Breather modes in spin chains: A study on the geometry and dynamics of certain special magnon modes

A thesis submitted

in partial fulfillment for the award of the degree of

Doctor of Philosophy

in

PHYSICS

by

Rahul O. R.

Department of Physics

Indian Institute of Space Science and Technology

Thiruvananthapuram, India

November 2019

Certificate

This is to certify that the thesis titled ***Breather modes in spin chains: A study on the geometry and dynamics of certain special magnon modes*** submitted by **Rahul O. R.**, to the Indian Institute of Space Science and Technology, Thiruvananthapuram, in partial fulfillment for the award of the degree of **Doctor of Philosophy** in **PHYSICS**, is a bona fide record of the original work carried out by him under my supervision. The contents of this report, in full or in parts, have not been submitted to any other Institute or University for the award of any degree or diploma.

Dr. S. Murugesh   Dr. Umesh R. Kadhane

Research Supervisor   Head of the Department

Department of Physics   Department of Physics

Place: Thiruvananthapuram

Date: November 2019

Declaration

I declare that this thesis titled *Breather modes in spin chains: A study on the geometry and dynamics of certain special magnon modes* submitted in partial fulfillment for the award of the degree of **Doctor of Philosophy** in **PHYSICS** is a record of original work carried out by me under the supervision of **Dr. S. Murugesh**, and has not formed the basis for the award of any degree, diploma, associateship, fellowship, or other titles in this or any other Institution or University of higher learning. In keeping with the ethical practice in reporting scientific information, due acknowledgments have been made wherever the findings of others have been cited.

Place: Thiruvananthapuram   Rahul O. R.

Date: November 2019   (SC14D002)

FOR MY MOTHER

Acknowledgements

Abstract

Geometry is inherent and well rooted in various disciplines of science. Integrable nonlinear system is one among them. They are exactly solvable with soliton solutions, and are naturally associated with differential curves and surfaces. One of the remarkable feature of integrable system is the *recurrence* property, wherein the system returns to its initial state through a rather complicated nonlinear evolution. This was observed for the first time as a paradox in the celebrated Fermi-Pasta-Ulam-Tsingou (FPUT) experiment. The paradox eventually led to the discovery of solitons and laid the foundation for the entire subject of integrability. The recurrence phenomena can be modelled by spatially periodic *breather* solution to the nonlinear Schrödinger equation (NLSE), more precisely, Akhmediev breather, wherein the system recovers the initial state in its time evolution. Being the governing model for a variety of physical systems, NLSE is well studied with a substantial amount of literature.

In this thesis we examine geometrical aspects of the NLSE in the context of breather solutions. The following nonlinear systems are studied owing to their close relationship with NLSE:

  ○ Classical 1-d Heisenberg Ferromagnet (HF),
  ○ Vortex filament in fluid under localized induction approximation (LIA).

In classical HF model we examine the breather excitation in detail. An explicit expression for the spin breather is presented. Spatially periodic case — a counter part of 'Akhmediev breather', is studied in particular. This special *magnon* mode leads to a *recurrence* phenomena in the HF model. In the background spin field the spin vectors take 'two' complete turns along the chain between its ends. During the breather excitation the spin chain continuously transforms to a configuration wherein the net turn becomes 'zero'. This peculiar geometrical feature is interpreted as a manifestation of the 'belt trick', which demonstrates the triviality of 4π rotation. Magnon mode is visualized in $\mathrm{SU}(2)$ group manifold along with a description of topological sectors and their energy lower bounds. In this breather mode the background spin configuration is a static field. Moreover, the initial and final configuration are exactly identical in the context of recurrence process.

Further, we present an explicit expression for a similar spin breather for which the background spin configuration is a dynamical field. This magnon mode is qualitatively different

in the sense that the recurrence process introduces an additional global rotation in the spin chain. That means the recurrence is not exact as in the previous case. This measurable change is treated as the 'trace' being left in the system during a breather excitation.

Mathematical framework of soliton theory associates each soliton solution with a surface in Euclidean 3-space. Geodesic on this surface is a space curve in $\mathbb{R}^3$ thereby providing a geometrical picture of the soliton solution. From a physics point of view, such a moving space curve approximately describes the dynamics of a vortex filament in fluid under LIA scheme. We obtain explicitly the breather excitation over a helical curve. Corresponding complex field of NLSE is also examined. We show that this is in fact a new *breather* solution to the NLSE. Specifically, the associated space curve is shown to have periodic *knot* formation in its time evolution. Previously known knotted solutions are of invariant shape which are associated with periodic solutions to the NLSE — more precisely, Kida class of solutions. We emphasize that a knot structure associated with a breather solution has so far not been witnessed. Spatially periodic case of this breather solution turn out to be a Galilean transformed version of the 'Akhmediev breather'. Their background space curves are a helix and a circle respectively. A circle and a helix are associated with plane wave solutions that are related through a Galilean transformation. We show that spatially periodic breathers of the Akhmediev type can also be obtained from a wave solution associated with a circle, through a Galilean transformation followed by a Darboux transformation. The general question of permutability of the two transforms, however remains open.

Contents

List of Figures

List of Tables

Abbreviations

FPUT   Fermi-Pasta-Ulam-Tsingou

NLSE   Non-Linear Schrödinger Equation

HF   Heisenberg Ferromagnet

1-d   one dimension

LIA   Localized Induction Approximation

MI   Modulation Instability

IST   Inverse Scattering Transform

AB   Akhmediev Breather

KMB   Kuznetsov-Ma Breather

PS   Peregrine Soliton

PDE   Partial Differential Equation

KdV   Korteweg-de Vries

LLE   Landau Lifshitz Equation

DT   Darboux Transformation

Nomenclature

ψ	solution to the nonlinear Schrödinger equation (NLSE)
$\boldsymbol{\Psi}$	solution to the Lax pair (linear system of equations) associated with the NLSE
$\hat{\mathbf{S}}$	solution to the 1-d Landau Lifshitz equation (LLE) or 1-d classical HF spin chain
$\mathbf{S}$	solution to the 1-d Landau Lifshitz equation (LLE) in matrix form
$\mathbf{R}$	solution to the localized induction approximation (LIA)
κ	curvature of the space curve
τ	torsion of the space curve
$\mathbb{R}^3$	Euclidean 3-space
κ_0	arbitrary real constant
λ_0	arbitrary complex parameter
ψ_{c}	plane wave solution to the NLSE associated with circle
ψ_{h}	plane wave solution to the NLSE associated with helix
ψ_{sh}	secant hyperbolic soliton of the NLSE
ψ_{cb}	breather solution to the NLSE over the plane wave ψ_{c}
ψ_{AB}	Akhmediev Breather
ψ_{GAB}	Galilean transformed Akhmediev Breather
$\Delta\varphi$	phase shift in the complex function ψ during a recurrence
$\Delta\theta$	additional global rotation in $\hat{\mathbf{S}}$ during a recurrence
$\mathrm{SU}(2)$	group of 2×2 special unitary matrices
$\mathrm{SO}(3)$	group of 3×3 special orthogonal matrices

Subscripts

t	$\frac{\partial}{\partial t}(\,)$; partial derivatives with respect to t
x	$\frac{\partial}{\partial x}(\,)$; partial derivatives with respect to x
λ	$\frac{\partial}{\partial \lambda}(\,)$; partial derivatives with respect to λ
R	real part of the complex variable
I	imaginary part of the complex variable

Chapter 1

Introduction

In physics we often encounter theoretical models that are comparatively simple, yet mathematically rich. It could be an equation or a set of equations that describe certain dynamics. They may not always represent an exact physical system to its minute details, but they carry the essential signature that define those systems. This often helps to gain significant insight into the system dynamics. One of the classic example is Lorenz attractor — a system of three differential equations, which possess the basic features of a chaotic system [1]. One can even think of a simpler model in one dimension, the 'logistic map' that shows chaotic behaviour [2]. The best part about these models is that they allow us to actually "see" the magic involved in the nonlinear evolution. For instance, one may witness the fractal geometry of a chaotic attractor; the self-similar structure at every scale [3, 4]. It is not an illustration of some previously known abstract idea, but the very intriguing nature of the system that cannot be revealed otherwise. Visualization of the dynamics have often played a decisive role in exploring the subject in detail.

The motion of a chaotic system will never repeat; there is no order. On the other hand, there are nonlinear systems that are completely ordered. In other words, infinitely many conservation laws present in the system restraining the system dynamics. These are integrable systems [5]. One can write analytical solutions for an integrable system, whereas one has to rely on numerical integration for a chaotic one. The integrability and chaos are two opposite regimes of nonlinear dynamics. One landmark in the history of integrable systems is FPUT experiment (FPU in earlier literature). Sixty-five years ago Fermi, Pasta, Ulam and Tsingou constructed a theoretical model by coupling a finite number of one dimensional anharmonic oscillators [6]. The first normal mode was excited initially with a finite amount of energy. Since the dynamical expression was nonlinear, they anticipated the sharing of energy with all the higher modes in equal manner. Sharing does occur as anticipated. However, after a sufficiently long time the initial mode is recovered with nearly

the same energy as in the beginning — a near recurrence. That was quite unexpected and paradoxical for a start [7].

Later studies showed that the mathematical model considered in FPUT experiment is in a way an integrable system. The motion of an integrable system can repeat. A more apt terminology is *recurrence*, in line with the landmark experiment. The energy sharing from first normal mode to higher modes, and the recovery of the first mode as in the beginning, is a common feature in nonlinear systems widely known as modulation instability (MI) [8]. Therefore the recurrence is not limited to the FPUT model alone. Technical details aside, one can consider the recurrence as the recovery of a smooth (single wave) initial condition through a rather complicated nonlinear evolution. This scenario can be exactly modeled by the *breather* solution of nonlinear Schrödinger equation (NLSE), more precisely a spatially periodic breather [9]. Initial and final stages are steady and smooth. The dynamics is actually taking place in between, much like shuffling playing cards in a peculiar way, that the cards end up in the same initial configuration. It is worth mentioning that the Fourier components of the breather mentioned here, analytically describe the growth–decay cycle of higher normal modes seen in the FPUT recurrence, where the recurrence occurs only once [10]. Breather is a special solution which has a pulsating nature along with localization properties [11]. They are soliton solutions with periodicity.

Every integrable system including NLSE, has a geometrical connection well rooted in the mathematical framework of soliton theory [12]. The connection can be explained less technically by invoking the relationship between a fluid vortex dynamics and the NLSE. One can think of a vortex filament around which fluid circulates. This vortex moves under its own induction. A simplified model can be considered omitting long range effects of the vorticity in ideal fluids. Such a model is now popularly known as localized induction approximation (LIA). In this scheme the curvature and torsion of the filament varies in such a way that they satisfy a coupled nonlinear equation. This finding was initially made by Da Rios in 1906, but remained obscure for more than fifty years [13]. However people have derived it in many different ways without being aware of the previous work. Later, it came to be known that the curvature and torsion, when put together to form a complex function in a certain manner, satisfies the NLSE. In other words, a soliton solution of the NLSE describes a moving space curve thereby providing a geometrical visualization of the complex solution [14]. Regarding the breather solution, such a space curve reflects the localization and periodicity geometrically [15].

There exist another mathematical model closely related to the NLSE, known as classical Heisenberg Ferromagnetic spin chain [16]. This is one dimensional system of classical

2

spins, 3-vectors, interacting with nearest neighbours. Spin-spin exchange interaction is arising as a consequence of the Pauli exclusion principle [17, 18]. Each vector can take arbitrary direction in three dimension. But the motion is constrained in such a way that nearby vectors try their best to align in the same direction. Excitations of a spin system are called *magnons* [18]. It can be treated as a wave in the spin chain. This classical HF spin chain is gauge equivalent to the NLSE [19]. In other words they are quite same in their underlying mathematics. Therefore the NLSE breather solutions must have a counterpart in classical HF model. What is special about spin chain is that they live in three dimensional space. Unlike complex solutions of NLSE one can actually "see" the dynamics.

It would be interesting to see the recurrence process in this HF spin chain. As pointed out earlier, the recurrence is like shuffling playing cards keeping the initial and final configuration identical. This could be visualized in spin chain during a breather excitation — a special *magnon* mode. The spin chain surely goes back to its initial orientation through a complicated nonlinear evolution. What happens in between? Are the initial and final configuration exactly identical? These questions are so far not explored in literature. This thesis tries to shed some light on this issue: the recurrence process in continuum spin chain, and their geometrical interpretations.

During our studies we observed certain interesting topological features in the associated space curve. Specifically, a periodic knot formation, so far not witnessed in breather excitations. We will detail these aspects also along with the magnon modes.

1.1 Rogue waves

There are certain special kind of waves that appear all of a sudden out of a calm and quite background; and disappear without leaving any remnants [20]. The concept is self evident from Fig. 1.1, which is an illustration of such a wave, widely known as *Rogue* wave or freak wave. Rogue waves can occur in deep ocean causing severe damage for ocean liners and oil platforms. This has been a mythical story for centuries till the scientific record of *Draupner wave* by digital measurements, during the New Year's day of 1995 at the Draupner platform in the North Sea [21, 22]. Rogue waves are not limited to ocean waves. Existance of rogue waves in optical fiber [23], plasma systems [24] and Bose - Einstein condensate under suitable conditions [25], are some of the areas of intense research in recent years. These waves are highly localized in space as well as in time, often modelled by exact solutions of

nonlinear Schrödinger equation (NLSE),

$$i\psi_t + \psi_{xx} + 2|\psi|^2\psi = 0, \tag{1.1}$$

which approximately describes wave dynamics in deep water [26]. NLSE is a useful model in many disciplines like optics, Bose - Einstein condensate, plasma physics, superfluid vortices, and ferromagnetic spin system to name a few [27, 28, 29, 16]. Being an integrable system, NLSE is exactly solvable with soliton solutions via Inverse Scattering Transform (IST) [30]. The detailed story of integrable system and the discovery of *soliton* goes a long way back in history, right from the celebrated Fermi-Pasta-Ulam-Tsingou experiment [6, 31] carried out in 1955.

| (a) | (b) | (c) | (d) | (e) |
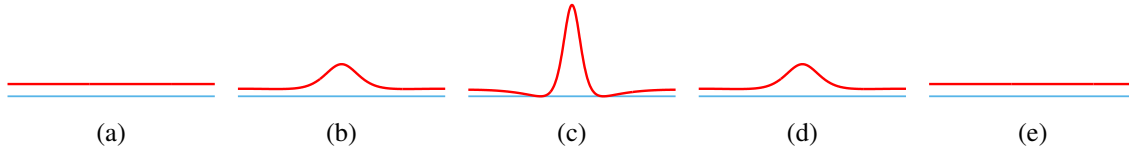
Figure 1.1: *Rogue wave* prototype — no hint, no trace.

In the NLSE framework, rogue wave can be seen as a special case of a more general solution called *breather* solution, where the energy localization has an oscillatory nature; either in space or in time. Spatially periodic breather is widely known as Akhmediev Breather (AB), time periodic one as Kuznetsov-Ma Breather (KMB), and the limiting case where the period of oscillation tends to infinity is termed as Peregrine Soliton (PS) [11].

1.2   Classical 1-d Heisenberg ferromagnet

One dimensional Heisenberg ferromagnet (HF) in the continuum limit is known to be equivalent to the NLSE [16, 19]. For simplicity, one may call it as classical HF model or simply HF model. In this model spins can be considered as unit vectors each having 3 rotational degrees of freedom, placed over a one-dimensional lattice. Spins at adjacent sites
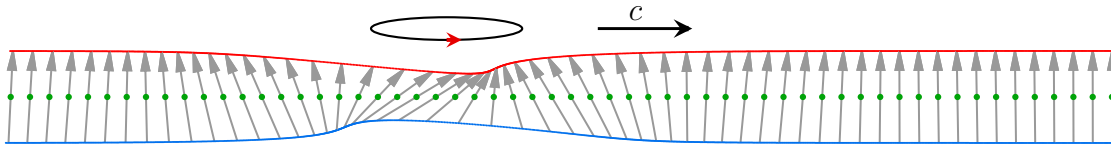
Figure 1.2: Soliton in the HF spin chain. Energy density, $E \propto \mathrm{sech}^2(x - ct)$.

4

interact via the exchange interaction arising out of the Pauli exclusion principle [17, 18]. This is an ideal model where there is no external magnetic field or damping force [32]. Interestingly, it is an integrable system endowed with soliton solutions [33]. The relationship between HF model and NLSE was initially identified by Lakhshmanan [34, 16] through geometrical arguments. More conclusively, Zakharov and Takhtajan showed that both the systems are gauge equivalent [19]. Therefore, associated with each solution to the NLSE, there exist a spin configuration. Thus all the features of NLSE can be expected in this spin system in an entirely different language.

To make this clear, consider the well known soliton solution to the NLSE — a localized travelling wave of 'secant-hyperbolic' type, ψ_{sh}. The corresponding solution in the HF spin chain is a localized disturbance moving with a constant speed [34, 35]. This is shown in Fig. 1.2, which can be seen as a soliton excitation over a static spin field.

1.3 Moving space curves

A vortex filament in an ideal fluid moves under its own induced velocity. Da Rios in 1906, formulated a dynamical expression for this motion by omitting the long range effects of the vorticity. Such a scheme is now known as localized induction approximation (LIA) [13]. Da Rios equation is an intrinsic equation describing a moving space curve, through a coupled partial differential equation of its curvature and torsion, given by

$$\kappa_t = -2\kappa_x \tau - \kappa \tau_x, \tag{1.2a}$$

$$\tau_t = \left(\frac{\kappa_{xx}}{\kappa} - \tau^2 \right)_x + \kappa \kappa_x. \tag{1.2b}$$

It has a rich history in literature as it was derived agian three times independently [36], without the authors being aware of the work done previously by Da Rios. One of its rediscovery was done by Lakshmanan *et al.* [34], wherein they wrote the dynamics of classical HF model in a coordinate independent way — as an intrisic equation similar to the Da Rios equation (but for a negative sign). The parallelism between Da Rios equation and the NLSE can be understood using the Hasimoto [37] function,

$$\psi = \frac{1}{2}\kappa \, e^{i\sigma}, \quad \sigma_x = \tau, \tag{1.3}$$

where κ and τ are respectively, the curvature and torsion of a curve. The complex function ψ is described by the NLSE (1.1), provided that κ and τ obeys the Da Rios equation (1.2).

(a) $\psi_l = 0$

(b) $\psi_{\mathrm{c}} = \kappa_0 e^{i2\kappa_0^2 t}$

(c) $\psi_{\mathrm{h}} = \kappa_0 e^{i\sqrt{2}\kappa_0 x}$

(d) $\psi_{\mathrm{sh}} = e^{i()} \operatorname{sech}(\ )$

(e) Akhmediev breather

(f) Kuznetsov-Ma breather
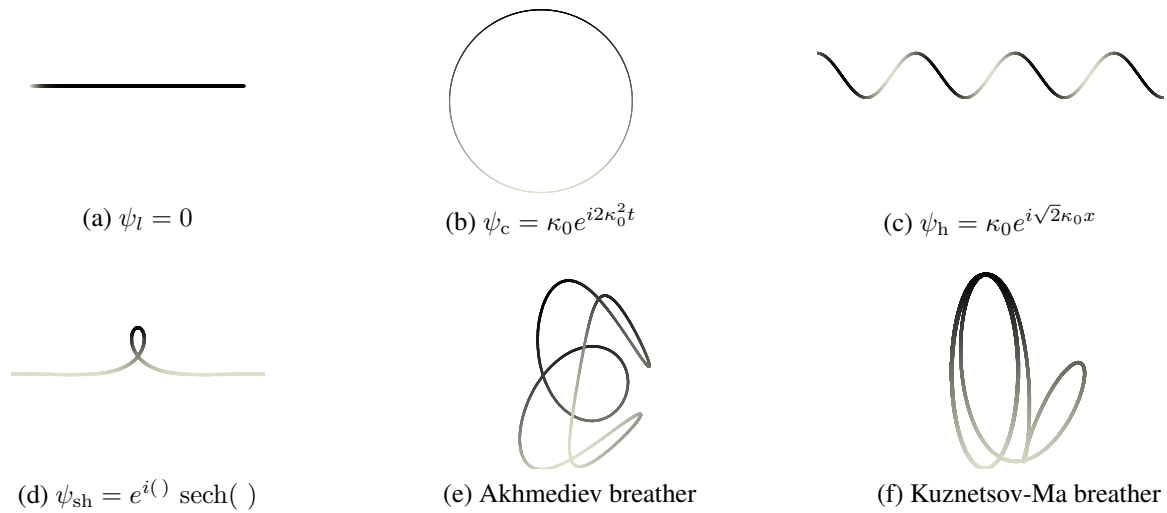
Figure 1.3: Space curves associated with ψ. Curves (a), (b), (c) and (d) are of invariant shape under time evolution. Straight line (a) doesn't move. Soliton excitation over the straight line leads to the traveling 'loop soliton' (Hasimoto loop) shown in (d). Breather excitation over the circle (b) leads to (e) and (f). Detailed plots for breathers (e) and (f) are given in Sec. 3.2.2.

In brief, there exist a moving space curve in $\mathbb{R}^3$ that can be systematically associated with each solution to the NLSE. Such a curve approximately describes motion of a vortex filament in an ideal fluid. Fig. 1.3 will elucidate the concept. Bathtub vortex [38] and smoke rings [39] are familiar examples of fluid vortices, which are respectively modeled by NLSE space curves shown in (a) and (b). Helical vortices (c) can be constructed experimentally [40]. Loop solitons (d) have been observed in the laboratory [41], and also in real situations like tornadoes [42]. A detailed description of the space curves will be provided in section 3.2.

Geometric nature of soliton solution is well rooted in the mathematical framework of integrable systems. In other words, the space curves are not limited to NLSE alone. A more rigorous formalism for the space curve, incorporating modified KdV and sine-Gordon equation was done by Lamb [43]. The concept of soliton surfaces was exemplified in a series of papers by Sym and co-workers [12, 44, 45, 46, 15], which is applicable to a broad class of integrable systems. In the particular case of NLSE, the curve described by the Da Rios equation is a geodesic on the soliton surface [44].

1.4 Solitons: A historical background

One of the major turning point in the study of nonlinear dynamics was the Fermi-Pasta-Ulam-Tsingou experiment, which is now considered to be the beginning of *experimental mathematics* [47]. Although the theoretical model under study was quite simple, its results were controversial in nature which continue to inspire many researchers all over the globe even after 65 years [48, 49, 50]. The FPUT problem has a decisive role in the understanding of integrable systems and soliton dynamics. For that reason, we will give an elaborate introduction to this experiment followed by a description of how does it lead to the discovery of solitons. However, minute mathematical details of this study is not necessary to understand the thesis work.

1.4.1 Fermi-Pasta-Ulam-Tsingou problem

The first ever numerical experiment Fermi-Pasta-Ulam-Tsingou problem was performed using one of the earliest computers, MANIAC I, at Los Alamos National Laboratory in 1955. Due to the demise of Fermi before the results were approved by him, it was not published that time but appeared as a classified report [6]. They studied the dynamics of a one dimensional chain of point masses linked together by linear force which is weakly perturbed by nonlinear terms. Let y_n be the displacement of the n-th mass from its equilibrium position. Two different systems were considered wherein the equation of motion for n-th mass can be written as,

$$\ddot{y}_n = (y_{n+1} - 2y_n + y_{n-1}) + \alpha \left[(y_{n+1} - y_n)^2 - (y_n - y_{n-1})^2 \right], \qquad (1.4\text{a})$$

$$\ddot{y}_n = (y_{n+1} - 2y_n + y_{n-1}) + \beta \left[(y_{n+1} - y_n)^3 - (y_n - y_{n-1})^3 \right]. \qquad (1.4\text{b})$$

For simplicity, they considered unit masses and the coefficient of linear term has been set to '1' without loss of generality. The first chain with quadratic non linearity is called α-model and the second chain with cubic non linearity is called β-model, where α and β are strengths of the nonlinear interaction between neighbours. Here end points are fixed, $y_0 = y_N = 0$. As a common approach they studied the system in terms of 'normal modes' $q_k(t)$, which are essentially the Fourier representation of $y_n(t)$, as given by

$$q_k(t) = \sqrt{\frac{2}{N}} \sum_{n=1}^{N} y_n(t) \sin \frac{\pi k n}{N}. \qquad (1.5)$$

7

Before going to the motivation behind this problem, it is necessary to make a distinction between integrable and non-integrable systems. For that purpose we will briefly discuss the unperturbed case, by setting $\alpha = 0$. Then the Hamiltonian for the α-model [7], turns out to be the Hamiltonian for a system of independent harmonic oscillators with frequency $\omega_k = 2\sin(\frac{\pi k}{2N})$ for the k-th normal mode. Let it be,

$$H(p_k, q_k) = \frac{1}{2}\sum_{k=1}^{N}(p_k^2 + \omega_k^2 q_k^2). \tag{1.6}$$

Here, $\dot{p}_k = -\omega_k^2 q_k$ and $\dot{q}_k = p_k$. For a given initial condition $q_k(0)$ and $p_k(0)$, it is possible to solve $q_k(t)$ and $p_k(t)$ at this stage. This special form of the Hamiltonian indicates a possible canonical transformation in which H is cyclic in the new coordinates [51, p. 378]. A new set of coordinates (Q_k, P_k) can be considered [5, p. 247] in the below form,

$$q_k = (2P_k/\omega_k)^{1/2}\sin Q_k, \quad p_k = (2P_k\,\omega_k)^{1/2}\cos Q_k, \tag{1.7}$$

so that the above Hamiltonian (1.6) get transformed to,

$$H_0(P_k, Q_k) = \sum_{k=1}^{N} P_k\,\omega_k. \tag{1.8}$$

Since H_0 is cyclic in Q_k, the conjugate momentum P_k is a constant. The solution for the system is, $P_k(t) = P_k(0)$ and $Q_k(t) = \omega_k t + Q_k(0)$, where $\omega_k = \partial H/\partial P_k$. For a given mode k, frequency ω_k is already a constant, so that $P_k\,\omega_k$ defines a new constant E_k, such that $H_0 = \sum E_k$. This E_k can be treated as the energy in the k-th mode, and the sum of which, is the total energy of the system. So, a harmonic system with N degree of freedom is solvable with solutions in the closed form and there exist N constants of motion. Since E_k's are separately constants, energy cannot be shared from one normal mode to another, and the energy equipartition is not possible in this harmonic limit [52]. We rarely get systems which are exactly solvable with explicit solutions. Here comes the notion of 'integrability'. *"An integrable Hamiltonian system is defined as one having as many single-valued, analytic constants of motion Φ_k as degrees of freedom, such that all pairwise Poisson brackets $\{\Phi_k, \Phi_l\} = 0$"* (Ford, 1992, p. 276) [7].

A more precise statement is given by Moser [53, p. 41] which is as follows: A Hamiltonian $H(p_k, q_k)$ is said to be integrable if there exist a canonical transformation from (p_k, q_k) into (P_k, Q_k) such that the Hamiltonian depends only on P_k. i.e., $H = H_0(P_k)$. Then the

temporal evolution of the system is given by,

$$P_k(t) = P_k(0), \quad Q_k(t) = Q_k(0) + \frac{\partial H_0}{\partial P_k}t, \tag{1.9}$$

where $k = 1, 2, \ldots, N$. The above canonical coordinates (P_k, Q_k) are referred to as 'normal coordinates', or sometimes action angle variables. $\frac{\partial P_k}{\partial t} = \{H_0, P_k\} = 0$, implies that all these P_k's are integrals of motion.

Since P_k's are constants of motion, the trajectory of an integrable system is spatially bounded. For $N = 1$, in a suitable phase space, the trajectory can be a circle. For $N = 2$ it can be on the surface of a torus. In general for a system having N degrees of freedom, system motion occurs on N-dimensional tori [5, 7]. Since Q_k's are cyclic variables, system dynamics can also be represented in Q_k plane, where Q_k at 0 and 2π are identified. (See section 8.3 in Ref. [5] and figures therein for a detailed discussion).

A natural question is this: what happens to the 'integrability' of the system under a small perturbation ?

Consider the perturbation of the form,

$$H = H_0(P_k) + \epsilon H_1(P_k, Q_k), \tag{1.10}$$

where $H_0(P_k)$ is integrable and ϵ is the strength of the perturbation. Clearly, $\epsilon = 0$, make the system integrable with N integrals of motion. Poincaré attempted to find how many of them survive when $\epsilon \neq 0$. He proved [54, p. 380] in 1889, that there exist no integrals of motion of the form $\Phi(P_k, Q_k, \epsilon)$ other than H.

Fermi was very much sure about this result, but was not aware of KAM theorem [55, p. 105] proposed around that period which proved a kind of near integrability for sufficiently small perturbation [56]. This was the reason behind setting the FPUT problem in that way — as a small perturbation to the linear problem [5, p. 259]. Since E_k's (Energy in the k-th mode) are the constants of motion in the linear problem, under perturbation they were led to believe that there exist no constants other than the total energy H. In short, in the presence of perturbation, $E_k = \dot{q}_k^2 + \omega_k^2 q_k^2$, would not remain constant under the time evolution, and the only possibility for this to happen is the sharing of energy between various modes. Sharing of energy should be in such a way that after a long time every mode will acquire same energy $\langle E_k \rangle$, which is independent of k, due to the 'equipartition theorem' in equilibrium statistical mechanics [52]. In fact, the motivation behind the FPUT experiment was not to confirm this energy equipartition, but to find the time it takes to

attain this equilibrium state [57, p. 977].

Fermi *et al.* studied the FPUT model (1.4) with an initial condition $y_n(0) = \sin\frac{n\pi}{N}$, $\dot{y}_n(0) = 0$, which is the same as exciting the chain in its 1st normal mode alone. They solved the equations of motion numerically for $y_n(t)$ (also for $\dot{y}_n(t)$) and expressed them in terms of normal modes q_k using (1.5). Energy in the k-th normal mode $E_k = \dot{q}_k^2 + \omega_k^2 q_k^2$, is computed in the due course, expecting that the initial energy given in 1st normal mode (E_1) will decrease gradually and the other higher modes will start to grow, thereby leading to energy equipartition after a suitable period of time. Contrary to their belief, the system didn't show any hint towards energy equipartition. Exchange of energy was observed only among first few normal modes. At the same time, this sharing was taking place in a regular fashion. This regularity is more profound with certain choice of parameters, so that the initial condition has been recovered (with a few percent closing error) and the system seems almost periodic. This (near) recurrence of initial state is observed in both α and β model as shown in Figs. 1 and 4 of their report [6]. See Fig. 8 in their report [6] to see the displacement $y_n(t)$, instead of 'normal modes'. It is worth quoting Zabusky at this point, who along with Kruskal treated the problem in this way to get an explanation for the recurrence — *"In fact, we have found that for this and similar problems, the description according to interacting interacting normal modes has usually been unrewarding as far as making decisive progress"*(Zabusky, 1967, p. 230) [58].

Although the 'recurrence' bring back the initial mode, a few percent of energy always get shared among other modes during a single FPUT period. This 'closing error' continues to increase in the next seven FPUT periods, beyond which the effect gets reversed. After fourteen such (near) recurrences, the 'return' to the initial condition was much closer than that of the first (near) recurrence. The existence of 'super-recurrence' (or super period) was studied by Tuck and Menzel [59], without which one could have argued that the system may show a tendency towards equipartition after a sufficiently long time. It is now recognized that the original problem of Fermi *et al.* was coded by Mary Tsingou Menzel who was credited for her work [6] but not listed as a co-author [31]. This is the reason why this crucial study was referred to as 'FPU problem' in previous literature.

Finally, FPUT results can be summarized as follows — certain small amount of non linearity imposed in their model didn't bring equipartition of energy. Higher 'normal modes' were practically absent as if the system have only a limited number of degrees of freedom. As a special case, this system even shows periodic behaviour, which is now known as recurrence property.

Some people considered the recurrence as a paradox, and later in 1965 Kruskal and

Zabusky explained this recurrence which shall be discussed in the next section. But other problems remained open at that time, namely the true reason behind the lack of equipartition under perturbation, and the strength of the perturbation (threshold) with which the system finally attain equipartition. These two apparent paradoxes have led to further studies. See for instance, Refs. [52, 60]. The FPUT experiment also stimulated the area of 'deterministic chaos' along with studies of 'integrable systems' which are now considered as the two pillars of nonlinear science [61, 62, 63].

1.4.2 Discovery of solitons

Kruskal and Zabusky attempted to study the recurrence problem using a continuum approximation of the discrete lattice. In fact, Fermi *et al.* had this in mind while formulating the problem. In their own words — *"for the purposes of numerical work this continuum is replaced by a finite number of points (at most 64 in our actual computation) so that the partial differential equation defining the motion of this string is replaced by a finite number of total differential equations"* (Fermi *et al.*, 1955, pp. 3–4) [6]. Which means, one has to go in the reverse direction to find out what partial differential equation (PDE) the discrete lattice corresponds to. Deducing that PDE and solving it under the given initial condition helps to achieve a clear picture of the system dynamics.

Displacement of the n-th particle $y_n(t)$, as mentioned in (1.4) can be replaced with $y(x, t)$ so that instead of counting n from 1 to N, one can vary x from 0 to L, the length of the chain. Replace $y_{n\pm1}(t)$ with corresponding Taylor expansion by keeping h as the lattice constant.

$$y_n(t) \equiv y(x, t); \qquad y_{n\pm1}(t) \equiv y(x, t) \pm hy_x + \frac{h^2}{2!}y_{xx} \pm \frac{h^3}{3!}y_{xxx} + \frac{h^4}{4!}y_{xxxx} \pm \cdots \quad (1.11)$$

On substituting this in (1.4), equation of motion for α model [58, p. 229] becomes

$$c^{-2}y_{tt} = (1 + \varepsilon y_x)y_{xx} + (h^2/12)y_{xxxx} + (\varepsilon h^2/6)y_{xxx}y_{xx} + O(h^4) + O(\varepsilon h^4), \quad (1.12)$$

where $\varepsilon = 2\alpha h$ and $c^2 = h^2 k/m$. Spring constant k and the mass of the particle m are set to '1' in (1.4) for simplicity. Here, $c^2 = \frac{hk}{(m/h)} =$ (elastic modulus / mass density), which is square of the sound speed in the lattice. At this point it is worth noting that for the harmonic limit $\alpha = 0$ (hence $\varepsilon = 0$),

$$y_{tt} = c^2 y_{xx} + c^2(h^2/12) \, y_{xxxx}. \qquad (1.13)$$

Lattice constant h arises as a measure of discreteness of the system . Omiting y_{xxxx} on the basis of negligibly small h^2, results in a non dispersive system. In other word, the discreteness (terms containing h^2 or higher powers) is required for the wave to spread out in the medium [58, 5]. Zabusky considered the lowest continuum limit of (1.12) in h, which is

$$y_{tt} = c^2(1 + \varepsilon y_x)y_{xx}, \tag{1.14}$$

and found an exact solution for it. But in this solution, y_x becomes multi-valued after a certain breakdown time, beyond which the evolution has no physical sense [64]. Kruskal and Zabusky later studied this in detail, taking the Fourier decomposition of $y(x, t)$ and found that the solution indeed describes the FPUT lattice dynamics suitably until the occurrence of breakdown [65]. Zabusky was already aware that the omission of higher derivatives has a role in this breakdown, which he had mentioned in the conclusion section of Ref. [64]. Finally, Zabusky and Kruskal decided to include the "discreteness or graininess of the medium" (term containing h^2) and focused on

$$c^{-2}y_{tt} = (1 + \varepsilon y_x)y_{xx} + (h^2/12)y_{xxxx}. \tag{1.15}$$

Introducing Riemann invariants and change of frame of reference [5, 58], they could derive a nonlinear partial differential equation of the form,

$$u_t + uu_x + \delta^2 u_{xxx} = 0, \tag{1.16}$$

where δ being the scaling factor. One can also arrive at (1.16) from (1.15) using an asymptotic transformation as shown by Toda [66, Sec. 5]. This PDE is the Korteweg-de Vries equation (KdV), well known since 1895, which was initially proposed to model the dynamics of a shallow water wave [67]. KdV equation also appears in the field of collision-free magneto hydrodynamics [68].

The term uu_x in (1.16) is the nonlinear term which is responsible for the breakdown of the wave profile. One can check this by considering the PDE, $u_t + uu_x = 0$, and its solution of the form $u(x, t) = F(x - ut)$, where $F(\xi)$ being some arbitrary function, say $\cos(\pi\xi)$. This is an implicit solution analogous to a traveling wave of the type $F(x - vt)$, where the velocity depends on the height u of the wave profile. Thus the regions of large u travel faster than other regions, and this overtaking effect eventually produces a flat front where u_x practically blows up [69, 5]. This kind of steepening of the wave is the outcome of non linearity. On the other hand, the term u_{xxx} is accountable for the dispersion in the

12

medium. The solution of $u_t + u_{xxx} = 0$, can be expressed in terms of Airy functions [69, p. 9], where an initial wave form splits into ripples (wave spreading) in its evolution [5, p. 364]. Therefore, the right amount of non linearity and dispersion is necessary for the wave to sustain in the long run.

Zabusky and Kruskal numerically solved the KdV equation in 1965, and resolved the puzzle of "recurrence" [70]. They studied the evolution of a long wave, $u(x, 0) = cos(\pi x)$, similar to the initial condition of FPUT problem, setting $\delta = 0.022$ in (1.16). They imposed a periodic boundary condition so that the waves go out through one of the boundaries, and re-appear from the other, instead of reflection in the fixed boundary problem. They observed that in the initial phase, the system behaves like $u_t + uu_x = 0$, where non linearity plays the major role, thereby steepening the wave profile towards the breakdown. But this (anticipated) breakdown ($u_x \rightarrow \infty$) will not occur as the term u_{xxx} starts to grow which produces ripples of small amplitude behind the already steepened wave profile (first peak). Amplitude of these ripples start to grow gradually, making them individual peaks having almost same shape and varying heights (8 solitary pulses in their study) [70, Fig. 1]. These solitary pulses travel with speeds proportional to their respective heights, eventually getting separated from each other. They either collide with those coming from the other side, or they overtake the shorter ones — both can be considered as solitary wave interaction. What is unusual here is that they interact by exchanging their respective positions, after which they reappear unaffected in size and shape [70]. This indicates that they are stable enough to sustain in the medium without losing their identity even after much longer period. These localized entities (solitary waves) interact among themselves in a way that resembles particle interaction. Therefore, the authors coined the word "soliton", for the first time. Motion of the pulses were quite random for a while. But in the later stage all the pulses came back to their respective positions, so that the original wave form is recovered almost completely — some what like a "mirror image" (in both space and time) of the splitting-up happened in the initial cosine wave [71]. Thus, the FPUT recurrence has been simulated successfully as a partial explanation to the paradox, which triggered further studies of 'soliton systems' or nonlinear integrable systems. A systematic method was developed for solving such systems analytically in closed form (KdV equation in particular), by Gardner *et al.* [72] in 1967 which is widely known as inverse scattering transform (IST).

1.5 NLSE breather: An exact solution for the recurrence

Form the beginning itself people were approaching the FPUT problem in two different ways, i.e., in terms of

1. Energy sharing between initial normal mode and other higher modes,

2. Recovery of initial wave profile after its breakdown into several wave packets.

Zabusky and Kruskal believed that the view point in terms of normal modes were not useful for the problem at hand. As far as the second view point is concerned, they have closed the problem in the context of elastic collision between solitons. Wave breaking process into envelope solitons is common phenomena seen in nonlinear and dispersive media. This can take place due to the periodic perturbations over a continuous background, which is well known in nonlinear science as modulation instability (MI) [73]. It is a basic phenomena in nonlinear systems which is extensively studied in the areas of optics, hydrodynamics, plasma physics and many more [8].

Interpretation of MI in terms of spectral components (Fourier modes) has close resemblance to the FPUT recurrence. In MI dynamics, energy sharing from central mode to the sidebands grows initially, then gradually comes to an end, reverses thereafter, and eventually reinforces the central mode once again as in the beginning. This is essentially a recurrence process. An exact analytic solution for this energy sharing was obtained much later by Akhmediev and Korneev, by considering the Fourier modes of spatially periodic breather solution to the NLSE [9]. This has been experimentally demonstrated using laser pulses in optical fibers [74]. A convenient mathematical expression for spectral evolution of Akhmediev breather (AB), and its comparison with numerical and experimental studies are shown in Refs [75, 76].

Thus, the recurrence observed in the FPUT experiment — the energy sharing between carrier wave and other spectral components, became more relevant later in the context of modulation instability (MI). This is in fact described by the Fourier expansion of the Akhmediev breather. This is the way FPUT recurrence is being perceived today [10].

1.6 Objectives of the thesis

Breather solution to the NLSE is an excitation over the plane wave $\psi_c = \kappa_0 e^{i2\kappa_0^2 t}$. In the context of Akhmediev breather, the plane wave will be recovered exactly as before (upto

a phase shift). This recurrence phenomena must have a counterpart in the classical HF model, owing to their gauge equivalence. The actual spin dynamics may provide a novel description for this recurrence. Motivated by this problem, our objective here is to obtain an explicit spin configuration associated with NLSE breather solution. Of particular interest to the recurrence problem, we will focus on the spatially periodic spin breather — a special magnon mode (Akhmediev type). Further studies will involve the topological features of this magnon mode by exploring the spinor representation, indicatrix, linking number etc. Energy lower bound for the magnon mode will be investigated.

A soliton solution can be systematically mapped to a geometric curve as shown in Fig. 1.3. Line, circle and helix are elementary in the study of geometrical curves as they are the simplest curves anyone can think of. Helix is more general among them because for a helix both the curvature and torsion are non-zero. Soliton (breather) excitation over a helical background may possess general features so far not witnessed in other existing space curves. To fill this gap, we will obtain a breather (excitation) solution over the plane wave $\psi_{\mathrm{h}} = \kappa_0 e^{i\sqrt{2}\kappa_0 x}$. Space curves associated with this breather solutions will be constructed explicitly. Galilean transformation of ψ_{c}, ψ_{h} and their respective breathers will be investigated. Spin configurations corresponding to this new breather will be studied with a focus on the spatially periodic case. Dynamics of this special magnon mode will be examined in the context of recurrence process.

1.7 Outline of the thesis

The thesis is thus organized as follows:

- In **Chapter 2** we present the mathematical background. This will involve a basic explanation of Lax pair and compatibility condition, a brief derivation of classical HF model right from Heisenberg Hamiltonian, derivation of Da Rios equation from the classical 1-d HF model, the Hasimoto map, gauge equivalence relationship, and the concept of soliton surfaces. Darboux transformation — the technique used in this thesis to construct soliton (breather) solution is briefly outlined.

- **Chapter 3** focuses on the space curve dynamics of the breather solutions. A detailed survey of various space curves associated with NLSE is provided. Further, we present explicit mathematical expression for a new breather solution, and its associated space curve. The associated space curve is shown to form a *knot* periodically. The time periods for *knot* and *unknot* are obtained numerically. We have shown that spatially

periodic case of this new breather is a Galilean transformation of the AB. In the context of LIA, the result is discussed in line with the recent laboratory studies of helical vortex excitations.

- **Chapter 4** is devoted to the breather excitation in classical HF model. An explicit mathematical expression for the spin breather is presented. Spatially periodic case (Akhmediev type) is considered wherein a particular rogue mode is studied in detail. Breather (rogue) excitation in the spin chain is found to demonstrate the well known *belt trick*. This peculiar topological feature is studied by exploring the spinor representation, i.e., a description of the spin dynamics in $\mathrm{SU}(2)$ group manifold. An energy lower bound is presented, thereby showing that the entire class of spin breather fall into two topological sectors.

- **Chapter 5** revolves around the FPUT recurrence in the HF model. Spin breathers associated with the *knotted* solution given in chapter 3 are obtained explicitly. We will focus on the spatially periodic case — a special magnon mode, to examine the recurrence process. It is shown that, during the recurrence process the spin chain has undergone an additional global rotation. This scenario is absent in the magnon mode given in Chapter 4. A comparison with these two is given.

- **Chapter 6** concludes the thesis by considering the key findings in a wider perspective. Some interesting research directions based on our results will be mentioned.

- **Appendix A** provides necessary mathematical derivation and and simplified steps related to Chapter 3.

- **Appendix B** provides necessary mathematical derivations and simplified steps. A brief description of AB, KMB, PS and their associated space curves are given.

Chapter 2

Theoretical background

2.1 Introduction

This chapter is entirely devoted to the mathematical background of the nonlinear systems to be studied in the thesis. Our study mainly involves three integrable systems namely –

 (1) nonlinear Schrödinger equation (NLSE),

 (2) Da Rios equation or LIA,

 (3) the classical HF model in one dimension.

This chapter will provide a comprehensive idea regarding the close relationship among these three. We use Darboux transformation (DT) technique to obtain new soliton (breather) solutions starting from trivial ones. This method is briefly outlined at the end of this chapter.

2.2 Lax pair and Compatibility condition

The idea of representing a nonlinear equation using two linear operators was due to Peter Lax [77], which now bears his name. This was proposed initially for KdV, and later for NLSE [30], indicating the applicability of IST in various nonlinear systems [5, 69]. A generalized method referred to as AKNS formulation (Ablowitz, Kaup, Newell, Segur) [78] is more convenient since the operators are in the form of matrices. We will introduce the concept of Lax pair only in the matrix form, and it is essential for the mathematical background to be discussed in the subsequent sections. Consider the system of linear matrix

equations,

$$F_x = U(x, t, \lambda)F, \tag{2.1a}$$

$$F_t = V(x, t, \lambda)F, \tag{2.1b}$$

where U and V are two matrix valued functions describing space and time evolution of F, and λ is an arbitrary spectral parameter in the language of IST. Equating mixed partial derivatives F_{xt} and F_{tx} computed from (2.1), the compatibility condition $F_{xt} = F_{tx}$ leads to the zero curvature condition

$$U_t - V_x + [U, V] = 0. \tag{2.2}$$

Let

$$\psi_t = \mathcal{K}(\psi, \psi_x, \psi_{xx}, ...), \tag{2.3}$$

be the integrable system in question, which is a nonlinear partial differential equation. If (2.3) can be shown as equivalent to (2.2), then the linear system (2.1) is said to be the Lax pair associated with the integrable system (2.3). In other words, one has to identify suitable U and V to constitute a Lax pair, such that the zero-curvature condition (2.2) give rise to the integrable system.

For a clarity on the nomenclature to be used, let us call U and V as connection coefficients (or simply connections) [79, p. 21], and the linear system (2.1) formed by them as Lax pair [80, p. 285]. We call F as the fundamental solution of the Lax pair [81, p. 5].

As an example, let U and V be (ideally functions of x, t and λ but for the purpose, they can be a function of ψ and its derivatives) in the below form,

$$U(\psi) = \begin{pmatrix} 0 & \psi \\ -\overline{\psi} & 0 \end{pmatrix} + \lambda \begin{pmatrix} -i & 0 \\ 0 & i \end{pmatrix}, \tag{2.4a}$$

$$V(\psi) = \begin{pmatrix} i|\psi|^2 & i\,\psi_x \\ i\,\overline{\psi}_x & -i|\psi|^2 \end{pmatrix} + \lambda \begin{pmatrix} 0 & 2\psi \\ -2\overline{\psi} & 0 \end{pmatrix} + \lambda^2 \begin{pmatrix} -2i & 0 \\ 0 & 2i \end{pmatrix}. \tag{2.4b}$$

Left hand side of the zero-curvature condition (2.2) then turn out to be a polynomial in λ, where the coefficient of λ^3, λ^2 and λ will vanish identically. The only term independent of λ survives, and results in the below matrix equation.

$$\begin{pmatrix} 0 & i\,\psi_t + \psi_{xx} + 2|\psi|^2\psi \\ -i\,\overline{\psi}_t + \overline{\psi}_{xx} + 2|\psi|^2\overline{\psi} & 0 \end{pmatrix} = 0 \tag{2.5}$$

18

Thus, the nonlinear Schrödinger equation (1.1) (and its complex conjugate), arises as the compatibility condition for a specific choice of U and V as given in (2.4). Therefore, the corresponding linear system (2.1) is said to form the Lax pair for the NLSE. For each solution $\psi(x,t)$ to the integrable system, there exist a fundamental solution to the Lax pair, so that one can think of a combination like – (ψ_0, F_0), (ψ_1, F_1), (ψ_2, F_2), and so on.

2.3   Classical 1-d Heisenberg Ferromagnet

Spin is an intrinsic property of a sub-atomic particle which is responsible for its magnetic dipole moment. Moreover, it does not have a classical analogue. In ferromagnetic materials, net magnetic dipole moment of an individual atom never gets cancelled due to the unpaired outer shell electron. This individual moment will try to align in the same direction as that of its neighbors. This will give rise to a spontaneous magnetic moment for an extremely small region called domain, even in the absence of an applied magnetic field [18]. Underlying mechanism behind this 'ordering' is the spin-spin exchange interaction that arises as a consequence of the Pauli exclusion principle [17, Sec. 76]. Dynamics of the system is governed by the Hamiltonian [82, 83],

$$\mathcal{H} = -J\sum_{i}^{N} \boldsymbol{S}_i \cdot \boldsymbol{S}_{i+1} \tag{2.6}$$

where $\boldsymbol{S}_i$ is the quantum mechanical spin operator for the i-th lattice and J is the exchange integral. It is clear from the Hamiltonian that the exchange interaction is confined to nearest neighbours. $\mathcal{H}$ given in (2.6) is widely known as Heisenberg Hamiltonian or Heisenberg model [83, 84]. One can examine the classical limit of (2.6), say classical Heisenberg model, by treating $\boldsymbol{S}_i$ as (unit) 3-vectors on an arbitrary dimensional lattice and the vectors that are nearest neighbours interact through their inner product. $J > 0$ leads to the spin ordering in ferromagnets and $J < 0$ corresponds to antiferromagnets [18]. Classical Heisenberg model is a statistical model used to study ferromagnetism. This is $n = 3$ case of the more general n-vector model [85] also known as $O(n)$ spin model describing n-dimensional interacting classical spins on a lattice [86]. $\mathcal{H}$ is invariant under global rotations in the spin space as the energy of interaction depends only on the relative orientation of the nearby spin vectors. Equation of motion for the spin at i-th site can be obtained from the Hamiltonian using,

$$\frac{d}{dt}\hat{\mathbf{S}}_i = \{\hat{\mathbf{S}}_i, \mathcal{H}\}. \tag{2.7}$$

19

If $\mathcal{A}$ and $\mathcal{B}$ are functions of spin, their Poisson bracket is given by [34],

$$\{\mathcal{A}, \mathcal{B}\} = \epsilon_{abc} \sum_{j=1}^{N} \frac{\partial \mathcal{A}}{\partial S_j^a} \frac{\partial \mathcal{B}}{\partial S_j^b} S_j^c \tag{2.8}$$

where ϵ_{abc} being the usual Levi-Civita tensor and the summation over the repeated indices is implied. Spin vector in terms of its components is given by, $\hat{\mathbf{S}}_i = \hat{\mathbf{e}}_a S_i^a + \hat{\mathbf{e}}_b S_i^b + \hat{\mathbf{e}}_c S_i^c$. Using (2.8), right hand side of (2.7) can be shown that, $\{\hat{\mathbf{S}}_i, \mathcal{H}\} = \epsilon_{abc} \hat{\mathbf{e}}_a \frac{\partial \mathcal{H}}{\partial S_i^b} S_i^c$. From (2.6), $\frac{\partial \mathcal{H}}{\partial S_i^b} = -J(S_{i+1}^b + S_{i-1}^b) = -J \sum_k^{(i)} S_k^b$, where $\sum_k^{(i)}$ implies the summation over nearest neighbour k of i. Thus Eq. (2.7) turn out to be

$$\frac{d}{dt} \hat{\mathbf{S}}_i = -J \epsilon_{abc} \hat{\mathbf{e}}_a \Big(\sum_k^{(i)} S_k^b \Big) S_i^c = J \hat{\mathbf{S}}_i \times \sum_k^{(i)} \hat{\mathbf{S}}_k \tag{2.9}$$

In the continuum limit, the distance between nearest neighbours approaches zero so that $\hat{\mathbf{S}}_i(t)$ can be replaced with a continuous function $\hat{\mathbf{S}}(\boldsymbol{r}, t)$. Expanding $\hat{\mathbf{S}}_{i+1}$ and $\hat{\mathbf{S}}_{i-1}$ around $\hat{\mathbf{S}}_i$ using Taylor series and applying the continuum limit $h \to 0$, yields $\sum_k^{(i)} \hat{\mathbf{S}}_k = 2\hat{\mathbf{S}}(\boldsymbol{r}) + h^2 \nabla^2 \hat{\mathbf{S}}(\boldsymbol{r})$. Finally, after suitable scaling in t,

$$\frac{d}{dt} \hat{\mathbf{S}}(\boldsymbol{r}, t) = \hat{\mathbf{S}}(\boldsymbol{r}, t) \times \nabla^2 \hat{\mathbf{S}}(\boldsymbol{r}, t) \tag{2.10}$$

This is called Landau Lifshitz Equation (LLE) [34, 87, 88]. We are interested in the (1+1) - dimensional case (x and t) of this classical Heisenberg ferromagnet (HF) owing to its integrability. Therefore, the required spin evolution equation, 1-d LLE, is given by,

$$\hat{\mathbf{S}}_t = \hat{\mathbf{S}} \times \hat{\mathbf{S}}_{xx}, \qquad \hat{\mathbf{S}}^2 = 1, \tag{2.11}$$

where $\hat{\mathbf{S}} = (S^1, S^2, S^3)$ is the unit spin field of interest. Note that in this thesis, we examine the HF model only in its classical version (or continuum limit) in (1+1) dimension. 1-d LLE describes the dynamics of classical 1-d HF model. Henceforth, whenever HF model is mentioned, it implies equation (2.11).

This is an ideal system with dimension (1+1) and there is no external field or damping. Generalized ferromagnetic spin system can have higher dimensions and additional interactions. In such a generalized spin system, a number of parameters are involved which makes the system highly complex and non-integrable [32]. The 1-d LLE has a close relationship with NLSE. Moreover, each solution of 1-d LLE (as well as NLSE) is associated with a

moving space curve in $\mathbb{R}^3$. Subsequently, these relationships will be discussed, but not in its chronological order of development in history.

After the discovery of 'solitons' in the numerical study [70] of KdV equation, a general method for obtaining solution in the closed form has been discovered by Gardner, Greene, Kruskal and Miura, which is now known as inverse scattering transform (IST) [72]. By employing IST, the integrability for NLSE [30] and HF model (or 1-d LLE) [33] has been established. Gauge equivalence between these two is introduced in 1979 [19]. This will be used in the thesis to derive the spin configuration that corresponds to a particular NLSE solution. Lax pair for the HF model (or 1-d LLE) is given by [19],

$$\begin{aligned}
\boldsymbol{\Phi}_x &= U_{HF}\boldsymbol{\Phi} = i\lambda\mathbf{S}\,\boldsymbol{\Phi}, \\
\boldsymbol{\Phi}_t &= V_{HF}\boldsymbol{\Phi} = \left(\lambda\mathbf{S}\mathbf{S}_x + 2i\lambda^2\mathbf{S}\right)\boldsymbol{\Phi},
\end{aligned} \tag{2.12}$$

where $\mathbf{S} = \sum S^i\sigma_i$, with $\sigma_i,\ i = 1,2,3$, being the Pauli matrices and S^i the components of the unit spin field $\hat{\mathbf{S}}$. Comparing (2.12) with (2.1) and making use of compatibility condition (2.2), 1-d LLE (2.11) can be written in the matrix form:

$$\mathbf{S}_t = \frac{1}{2i}[\mathbf{S}, \mathbf{S}_{xx}], \qquad \mathbf{S}^2 = \mathbf{I}. \tag{2.13}$$

If we write the Lax pair for the NLSE,

$$\begin{aligned}
\boldsymbol{\Psi}_x &= U\boldsymbol{\Psi}, \\
\boldsymbol{\Psi}_t &= V\boldsymbol{\Psi},
\end{aligned} \tag{2.14}$$

where U and V are connections defined in (2.4), $\boldsymbol{\Psi}$ is the fundamental solution of the Lax pair. It is to be noted that, $\boldsymbol{\Psi} \in \mathrm{SU}(2)$ Lie group whereas connections $U, V \in \mathfrak{su}(2)$ Lie algebra [80, p. 209]. Using gauge equivalence [19], spin configuration can be expressed as

$$\mathbf{S} = \lim_{\lambda\to 0} \boldsymbol{\Psi}^\dagger\sigma_3\boldsymbol{\Psi}. \tag{2.15}$$

The NLSE and 1-d LLE are thus said to be equivalent. In other words, a solution $\psi(x,t)$ to the NLSE determined using $\boldsymbol{\Psi}$ that satisfies the Lax pair (2.14) then corresponds to a spin configuration $\mathbf{S}(x,t) \in \mathfrak{su}(2)$ (in matrix form), through equation (2.15). In short, (2.15) presents a systematic way of finding a spin configuration corresponding to each solutions of NLSE obtained through inverse scattering transform technique.

2.4 Moving space curves – Da Rios equation

Study of space curves is an integral part of differential geometry. It is possible to characterize a curve in a coordinate independent way by specifying two continuous functions, namely curvature and torsion [89]. For a curve parametrized by arclength x, curvature $\kappa(x)$ and torsion $\tau(x)$ can be expressed using a canonical 'triad' of three mutually perpendicular unit vectors, defined everywhere on the curve (see Fig. 2.1). Let $\mathbf{R}(x,t)$ be the position vector of the curve. The unit vectors $\hat{\mathbf{e}}_1, \hat{\mathbf{e}}_2, \hat{\mathbf{e}}_3$ of a triad, also known as tangent, normal and binormal vectors respectively, are defined as follows:

$$\hat{\mathbf{e}}_1 = \mathbf{R}_x, \qquad \hat{\mathbf{e}}_2 = \frac{\hat{\mathbf{e}}_{1x}}{|\hat{\mathbf{e}}_{1x}|}, \qquad \hat{\mathbf{e}}_3 = \hat{\mathbf{e}}_1 \times \hat{\mathbf{e}}_2. \tag{2.16}$$

Curvature and torsion are defined as,

$$\kappa = \left(\hat{\mathbf{e}}_{1x} \cdot \hat{\mathbf{e}}_{1x}\right)^{\frac{1}{2}}, \quad \tau = \kappa^{-2}\hat{\mathbf{e}}_1 \cdot \left(\hat{\mathbf{e}}_{1x} \times \hat{\mathbf{e}}_{1xx}\right). \tag{2.17}$$

Geometrically, κ is a measure of local deviation of the curve from a straight line, while τ gives a measure of rate at which osculating plane (determined by $\hat{\mathbf{e}}_1$ and $\hat{\mathbf{e}}_2$) turns [90, p. 57].
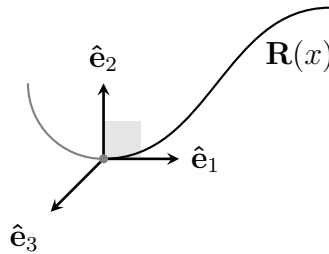
Figure 2.1: Triad

Motion of the triad along a static space curve is described by its derivatives with respect to x, expressed by the Serret-Frenet system of equation. This was initially obtained in 1847 by Frenet and later independently by Serret in 1851 [89, p. 19], which may be written as

$$\frac{\partial}{\partial x} \begin{pmatrix} \hat{\mathbf{e}}_1 \\ \hat{\mathbf{e}}_2 \\ \hat{\mathbf{e}}_3 \end{pmatrix} = \begin{pmatrix} 0 & \kappa & 0 \\ -\kappa & 0 & \tau \\ 0 & -\tau & 0 \end{pmatrix} \begin{pmatrix} \hat{\mathbf{e}}_1 \\ \hat{\mathbf{e}}_2 \\ \hat{\mathbf{e}}_3 \end{pmatrix}. \tag{2.18}$$

Moreover, one can think of a moving space curve, where the time evolution of the triad is

22

expressed in the rigid-body form [91, 92]

$$\frac{\partial}{\partial t} \begin{pmatrix} \hat{\mathbf{e}}_1 \\ \hat{\mathbf{e}}_2 \\ \hat{\mathbf{e}}_3 \end{pmatrix} = \begin{pmatrix} 0 & \omega_3 & -\omega_2 \\ -\omega_3 & 0 & \omega_1 \\ \omega_2 & -\omega_1 & 0 \end{pmatrix} \begin{pmatrix} \hat{\mathbf{e}}_1 \\ \hat{\mathbf{e}}_2 \\ \hat{\mathbf{e}}_3 \end{pmatrix}, \tag{2.19}$$

where ω_i's are arbitrary functions of x and t. Zero curvature condition (2.2) for the above system reads,

$$\kappa_t = \omega_{3x} + \tau\omega_2, \qquad \tau_t = \omega_{1x} - \kappa\omega_2, \qquad \omega_{2x} = \tau\omega_3 - \kappa\omega_1. \tag{2.20}$$

Lakshmanan *et al.* in a classic work [34], expressed the 1-d LLE (2.11) in coordinate independent form using the identification, $\hat{\mathbf{e}}_1 \equiv \hat{\mathbf{S}}$. More simply, they found a curve for which the tangents are spin vectors obeying 1-d LLE. As the Hamiltonian $\mathcal{H}$ (2.6) is invariant under a global rotation, the location and orientation of the curve are immaterial. Thus, taking $\hat{\mathbf{e}}_1 \equiv \hat{\mathbf{S}}$, the 1-d LLE (2.11) can be expressed as

$$\hat{\mathbf{e}}_{1t} = \hat{\mathbf{e}}_1 \times \hat{\mathbf{e}}_{1xx}, \qquad (\hat{\mathbf{e}}_1 \cdot \hat{\mathbf{e}}_1 = 1). \tag{2.21}$$

Having this additional expression, we are in a stage to write ω_i's in terms of κ and τ. This can be done by using compatibility condition $(\hat{\mathbf{e}}_i)_{tx} = (\hat{\mathbf{e}}_i)_{xt}$, $i = 1, 2, 3$. It follows that $\omega_1 = \kappa_{xx}/\kappa - \tau^2, \omega_2 = -\kappa_x$, and $\omega_3 = -\kappa\tau$. Substituting ω_1, ω_2 and ω_3 in (2.20) leads to a coupled nonlinear partial differential equation [34], given in (1.2). Finding a general solution for (1.2) is a challenging problem. However, solutions of the traveling wave type have been obtained [34], which have energy localization in a finite region — a solitary wave.

Intrinsic equations given in (1.2) were initially derived by Da Rios in an entirely different context, describing the dynamics of a non-stretching thin vortex filament due to the self induced velocity in an incompressible inviscid fluid. Assumptions employed in his study omitted the long range effects of the vorticity, and came to be referred to as Localized Induction Approximation (LIA) [13]. Much later, Arms and Hama rediscovered the LIA equation in vector form [93], which can be conveniently written as,

$$\mathbf{R}_t = \mathbf{R}_x \times \mathbf{R}_{xx}, \tag{2.22}$$

where $\mathbf{R}(x,t)$ is the position vector of the vortex filament. Put it differently, velocity of the filament, $\boldsymbol{v} = \mathbf{R}_t = \kappa\,\hat{\mathbf{e}}_3$, where κ is the curvature and $\hat{\mathbf{e}}_3$ is the binormal vector for

the curve. Induced velocity on a segment of the filament is proportional to its curvature at that point. Starting with (2.22), Betchov [94] derived a pair of intrinsic equations, wherein κ and τ are coupled together almost in a similar fashion as that of (1.2), without being aware of the work done by Da Rios. Hasimoto [37] introduced a complex function in terms of κ and τ as a solution to the NLSE, provided that κ and τ satisfies the Betchov's equation. Lamb [43, 95] extended this geometrical interpretation by setting a general formalism, which is also applicable to integrable systems like sine-Gordon equation and modified Korteweg-de Vries equation.

More specifically, the Hasimoto function

$$\psi(x,t) = \frac{1}{2}\kappa(x,t) \, \exp\left\{ i \int_0^x \tau(x',t) \, dx' \right\}, \tag{2.23}$$

satisfies the NLSE, $i\psi_t + \psi_{xx} + 2|\psi|^2\psi = 0$, provided that κ and τ are solution to the Da Rios equation (1.2). Alternatively, if ψ is expressed in the above form, the imaginary part of NLSE turn out to be (1.2)(b), and the real part after a differentiation with respect to x, becomes (1.2)(a). Moreover, if $\mathbf{R}(x,t)$ represents a non-stretching curve ($|\mathbf{R}_x| = 1$), differentiation of LIA (2.22) with respect to x, leads to $\mathbf{R}_{tx} = \mathbf{R}_x \times \mathbf{R}_{xxx}$. Compatibility condition on $\mathbf{R}$ gives $\mathbf{R}_{tx} = \mathbf{R}_{xt}$. An identification $\mathbf{R}_x \equiv \hat{\mathbf{S}}$, leads to 1-d LLE (2.11). Therefore LIA represents a moving space curve $\mathbf{R}(x,t)$, for which the tangent is a unit spin vector $\hat{\mathbf{S}}(x,t)$ field, obeying 1-d LLE (2.11).

To sum up, LIA (2.22) is the vector form of Da Rios equation (1.2). Lakshmanan *et al.* [34] showed that 1-d LLE (2.11) and the Da Rios equation are equivalent. Hasimoto [37] and Lamb [43] proposed a space curve dynamics associated with each solution to the NLSE. Following these developments, Lakshmanan extended their previous result of classical HF model towards the NLSE, and combined above nonlinear systems (2.11), (1.2) and (1.1) altogether [16]. Parallelly, it was shown by Zakharov and Takhtajan that classical HF model and NLSE are gauge equivalent [19].

2.5 Soliton surfaces

Through the Lax pair formulation a non-linear system is represented as the compatibility condition of a linear system. Recall Eq. (2.14) for instance, solving NLSE for ψ is then equivalent to finding the fundamental solution $\boldsymbol{\Psi}$. For a real spectral parameter λ, connections U and V taking values in matrix Lie algebra $\mathfrak{g}$, and $\boldsymbol{\Psi}$ is confined to the corresponding

Lie group. The matrix function $\mathbf{r}(x, t, \lambda)$ given by Sym-Tafel formula [12]

$$\mathbf{r}(x, t, \lambda) = \mathbf{\Psi}^{-1}(x, t, \lambda)\mathbf{\Psi}_{,\lambda}(x, t, \lambda), \qquad (2.24)$$

is then $\mathfrak{g}$ - valued. Here, suffix denotes derivative with respect to λ. Function $\mathbf{r}(x, t, \lambda)$ represents a λ - family of surfaces embedded into the Lie algebra $\mathfrak{g}$. The real parameter λ enumerates the members of the family, i.e, copies of the surfaces. The concept of soliton surfaces thus established the geometric nature of soliton solution which is applicable in a broad class of integrable systems endowed with a Lax pair [45, 96]. In the case of NLSE, Lie algebra of the linear system $\mathfrak{g}$ is $\mathfrak{su}(2)$ which is equivalent to $\mathbb{R}^3$, and the soliton surface is therefore embedded into a 3-dimensional Euclidean space [80]. Interestingly, the space curve associated with a soliton solution at any instant of time during its evolution is a geodesic on the soliton surface. Otherwise stated, soliton surface $\mathbf{r}(x, t)$ is swept out by the vortex filament under LIA and the tangent vector $\mathbf{r}_t(x, t)$ is the spin field that satisfies 1-d LLE [44].

Out of all λ - family of surfaces (2.24), one corresponding to $\lambda = 0$ describes the space curve motion [46, 15]. Therefore, the curve given by

$$\mathbf{R} = \lim_{\lambda \to 0} \mathbf{\Psi}^{-1}\mathbf{\Psi}_{\lambda}, \qquad (2.25)$$

is a solution to the LIA (2.22). Obviously $\mathbf{R} \in \mathfrak{su}(2)$ can be expressed in Cartesian coordinate system using an identification $\{i\sigma_1, i\sigma_2, i\sigma_3\} \equiv \{\hat{\mathbf{i}}, \hat{\mathbf{j}}, \hat{\mathbf{k}}\} \in \mathbb{R}^3$.

2.6 Darboux Transformation

This is a technique, in the form of a transformation relation, used to construct new soliton solutions from fairly simple ones. DT technique is extremely useful in extending the results from NLSE scheme towards 1-d LLE and LIA. This is because, the transformation is essentially acting on fundamental solution of the Lax pair.

2.6.1 Classical Darboux Transformation

The idea behind this transformation was first published in 1882 by the French mathematician Gaston Darboux [97], and the term "Darboux Transformation" was coined by Matveev [98] much later in 1979. Darboux studied the eigenvalue problem of Sturm-

Liouville equation,

$$-\phi_{xx} + u(x)\phi = \lambda\phi, \tag{2.26}$$

which is a linear partial differential equation of second order, well known in Quantum mechanics as 1-d time independent Schrödinger equation. $\phi(x, \lambda)$ is the solution corresponding to a potential function $u(x)$, and λ is a constant called spectral parameter. If $f(x) = \phi(x, \lambda_0)$ is a fixed solution at $\lambda = \lambda_0$, then (2.26) is covariant under the linear transformation $u \to u'$ and $\phi \to \phi'$ given by

$$\phi' = \phi_x - \frac{f_x}{f}\phi, \qquad u' = u - 2(\ln f)_{xx}. \tag{2.27}$$

In other words, if a combination (u, ϕ) satisfies (2.26), so does the new (u', ϕ'). Such transformation is called classical (original) Darboux transformation, and can be iterated as follows

$$(u, \phi) \longrightarrow (u', \phi') \longrightarrow (u'', \phi'') \longrightarrow \cdots \tag{2.28}$$

Note that the system (2.26) is a linear system. Associated with each solution ϕ, there exist a potential $u(x)$. The role of $u(x)$ will be clear if we consider one more linear system which is covariant under DT [99], as shown below,

$$\phi_t = -4\phi_{xxx} + 6u\phi_x + 3u_x\phi. \tag{2.29}$$

One can check the compatibility condition for these linear systems by computing $(\phi_{xx})_t$ from (2.26) and $(\phi_t)_{xx}$ from (2.29). Then for all λ, the necessary and sufficient condition for $(\phi_{xx})_t = (\phi_t)_{xx}$ being an identity, turns out to be

$$u_t - 6uu_x + u_{xxx} = 0, \tag{2.30}$$

which is the well known Korteweg-de Vries equation. Sign of the coefficient of uu_x is unimportant [72, 100], since $u \to -u$ leads to the other form (1.16) given earlier. The potential function $u(x)$ now turn out to be the solution of an integrable system. This integrable system is the compatibility condition for the system of linear equations (2.26) and (2.29). The covariance of the linear system (2.26) and (2.29) along with the compatibility condition, ensure that the new potential u' generated via DT will also be a solution to (2.30). Therefore, in the context of DT, solitons (potential u) comes into picture when the concerned integrable equation (say KdV) is represented as the compatibility condition for a system of two linear equations which are covariant under DT.

26

2.6.2 Matrix Darboux Transformation

Recall the system of linear equation (2.1), a matrix equation, known as Lax pair. Let $F(x, t, \lambda)$ be a matrix solution to (2.1), more particularly a fundamental solution of the Lax pair. Here, in order to generate new solutions, one needs to find a transformation in the form of a matrix operator. What is required here is a transformation from a known solution $F(x, t, \lambda)$ to an unknown solution $F'(x, t, \lambda)$. This must be accompanied by a transformation in connections U and V such that their structure remains unaffected. Consider the transformation,

$$F(x, t, \lambda) \rightarrow F'(x, t, \lambda) = G(x, t, \lambda)F(x, t, \lambda), \tag{2.31}$$

along with

$$U \rightarrow U' = G_x G^{-1} + GUG^{-1} \tag{2.32a}$$

$$V \rightarrow V' = G_t G^{-1} + GVG^{-1} \tag{2.32b}$$

where G is an invertible matrix. Upon multiplying F' from the right in (2.32) and using (2.31) in the right hand side, results in a new linear system of equations,

$$F'_x = U'(x, t, \lambda)F', \tag{2.33a}$$

$$F'_t = V'(x, t, \lambda)F', \tag{2.33b}$$

provided that F is a fundamental solution to (2.1). One can also verify from (2.32) that,

$$U'_t - V'_x + [U', V'] = U_t - V_x + [U, V]. \tag{2.34}$$

Which means the compatibility condition in (2.2) is invariant with respect to the above mentioned transformation. In physics such a transformation is called gauge transformation, and the representation of certain nonlinear system as the compatibility condition (2.2) remains valid for the whole class of gauge-equivalent connections [79]. But, in general the gauged system (2.33) may not have the same form as (2.1), i.e, the linear system may not be covariant with respect to the transformation (2.32).

To make this clear, recall (2.4), wherein one can see the soliton solution ψ (soliton field or potential) appearing in connections (U, V) in a definite pattern. This will allow us to call them as functions of ψ, say $U(\psi)$ and $V(\psi)$. The compatibility condition give rise to the corresponding nonlinear equation, $\psi_t = \mathcal{K}(\psi, \psi_x, \psi_{xx}, ...)$. Now suppose, the gauge equivalent connections in (2.33) is such that, $U' = U(\psi')$ and $V' = V(\psi')$. Then the

compatibility condition leads to $\psi'_t = \mathcal{K}(\psi', \psi'_x, \psi'_{xx}, ...)$. A transformation in this manner preserves the form of U and V, wherein one can replace the previous soliton solution ψ with an updated one. This type of transformation is called matrix Darboux transformation, for which a suitable choice of $G(\lambda)$ is necessary [101, 80, 81]. We outline the procedure below.

Let $\phi_{[1]}$ and $\phi_{[2]}$ be two known vector valued eigenfunctions of the Lax pair (2.1) corresponding to the parameters λ_1 and λ_2, where $\lambda_1 \neq \lambda_2$. On the introduction of matrices

$$M_0 = \text{diag}(\lambda_1, \lambda_2), \quad H = \begin{pmatrix} \phi_{[1]} & \phi_{[2]} \end{pmatrix}, \quad G_0 = -HM_0H^{-1}, \qquad (2.35)$$

the Darboux matrix $G(\lambda)$ can be found in the form

$$G(\lambda) = \lambda \mathbf{I} + G_0. \qquad (2.36)$$

As a remark: G_0 is independent of λ. $\det G(\lambda) = (\lambda - \lambda_1)(\lambda - \lambda_2)$. A suitable function $g(\lambda)$, in transformation relation $F' = g(\lambda)GF$, may ensure that $\det F' = 1$, to make it unitary if required.

Starting with a known solution ψ to the integrable system, a new solution ψ' can be obtained by,

$$\psi' = \psi - 2i(G_0)_{12}, \qquad (2.37)$$

where, $(G_0)_{12}$ is the second element of the first row in G_0. A natural choice of matrices M_0 and H can be achieved in the following way,

$$M_0 = \begin{pmatrix} \lambda_0 & 0 \\ 0 & \overline{\lambda_0} \end{pmatrix}, \quad H = \begin{pmatrix} \phi_{[1]} & \phi_{[2]} \end{pmatrix} = \begin{pmatrix} \phi_1 & -\overline{\phi_2} \\ \phi_2 & \overline{\phi_1} \end{pmatrix}, \qquad (2.38)$$

To preserve the polynomial structure of U and V, and to ensure the covariance of the Lax pair (2.1) under the transformation, $G(\lambda)$ should satisfy [80, p. 277],

$$G(\lambda_1)\phi_{[1]} = (\lambda_1 \mathbf{I} + G_0)\phi_{[1]} = 0, \qquad (2.39\text{a})$$

$$G(\lambda_2)\phi_{[2]} = (\lambda_2 \mathbf{I} + G_0)\phi_{[2]} = 0. \qquad (2.39\text{b})$$

By the choice of M_0 and H as given in (2.38), this condition is always satisfied. For a detailed proof of these assertions and an elaboration of the technique, see Refs. [80, 81].

Chapter 3

Breather solutions to the nonlinear Schrödinger equation and knotted space curves

3.1 Introduction

A space curve in $\mathbb{R}^3$ can be characterized in a coordinate independent way by specifying two single valued continuous functions $\kappa(x)$ and $\tau(x)$, say curvature and torsion respectively, where x being its arclength parameter. Such an equation is called *natural* or *intrinsic* equation for the curve. The fundamental theorem of space curves [89] says that there exists a unique curve (upto a global translation or rotation) for a given curvature and torsion. Curves that are associated with nonlinear Schrödinger equation (NLSE) via Hasimoto map [37], $\psi = \frac{1}{2}\kappa \exp\left[i\int_0^x \tau\, dx\right]$ are significant in the field of integrable systems, as they reveal soliton behaviour geometrically. Moreover, they are physically realizable in the context of fluid vortex dynamics in certain aspects.

In this chapter we present a new breather solution to the NLSE, where the associated space curve is *knotted*. What is narrated in the space curve is the true essence of the solution, which in fact cannot be revealed merely by looking at the soliton profile. Since NLSE is integrable, and is used to model a number of physical systems, this *knotted* breather solution is promising, and it demands an in-depth study to uncover its physical interpretation in various fields.

We will begin with an overview about various types of space curves associated with the NLSE. Using Darboux transformation technique, a new breather solution over the plane wave background $\psi_{\mathrm{h}} = \kappa_0 e^{i\sqrt{2}\kappa_0 x}$, is obtained. The space curves associated with this

breather is presented with detailed plots. Periodic *knot* formation in the space curve evolution is studied in detail. We note that spatially periodic case of the new breather solution is related to the well known Akhmediev breather through a Galilean transformation.

3.2   NLSE and space curves: an overview

Before going into the results, a brief discussion about various solutions to the NLSE and LIA is necessary. Each solution to the NLSE (1.1), $\psi(x,t)$ is related to a space curve via Hasimoto function [37, 16],

$$\psi = \frac{1}{2}\kappa\, e^{i\sigma}, \quad \sigma_x = \tau, \tag{3.1}$$

where κ and τ, respectively are the curvature and torsion of certain space curve parametrized by its arc length x. As detailed in Sec. 2.4, the curve defined by κ and τ could be a solution to the LIA equation

$$\mathbf{R}_t = \mathbf{R}_x \times \mathbf{R}_{xx}, \tag{3.2}$$

that describe, approximately the kinematics of a vortex filament in fluid under ideal conditions.

3.2.1   Solitons

The most trivial solution

$$\psi_l = 0, \tag{3.3}$$

corresponds to a straight line, since the curvature is zero (Fig. 1.3 (a)). Suffix l in (3.3) represents 'line'. The self-induced velocity on a segment of the vortex filament is proportional to its local curvature [13], which is zero in this case. Hence this vortex line does not move or change its shape in ideal situation. This is the most familiar example of a vortex, known as "bathtub vortex" that forms in a rotating container with a small drain hole at the bottom [38, Fig. 1]. The 1-soliton excitation over the zero background give rise to a secant-hyperbolic envelop soliton [30],

$$\psi_{\mathrm{sh}} = 2\lambda_{0I} \exp\left(i\mu_{0R}\right)\operatorname{sech}\mu_{0I}, \tag{3.4}$$

where $\mu_0 = \mu_{0R} + i\mu_{0I} = 2\lambda_0 x - 4\lambda_0^2 t$, and $\lambda_0 = \lambda_{0R} + i\lambda_{0I}$ is the complex scattering parameter that determines the amplitude and velocity of the soliton. Two more constants indicating the initial phase and position has been set to zero without loss of generality. This

is a travelling wave solution that preserves its size and shape as it moves. The corresponding space curve, the well known Hasimoto loop [37], can be thought of as the 1-soliton excitation of a straight line vortex. This is a localized helical twist (Fig. 1.3(d)), travelling along the straight line filament without any change in its size and shape. Small deformations of the real fluid vortex filament in the form of a helical twist that resembles solitary waves have been observed in laboratory [41]; similarities have been noticed in real situations like tornadoes [42, Fig. 1]. Similarly, the 2-soliton solution describes two isolated bumps as $t \to \pm\infty$, travelling with different speed (in general) which preserves their identity after the interaction (collision) [30]. Evidently, in the associated space curve one can see two Hasimoto loops moving along the vortex filament; faster one overcome the other, and regain their individual soliton structure after the interaction [46].

3.2.2 Breathers

A non-trivial seed solution

$$\psi_{\mathrm{c}} = \kappa_0 \, e^{2i\kappa_0^2 t}, \tag{3.5}$$

for some real constant κ_0, a plane wave of uniform magnitude and time dependent phase describes a curve of constant curvature and zero torsion — a circle. Note that the suffix c in ψ_{c} indicate 'circle' — its associated space curve (Fig. 1.3 (b)). An explicit expression for the space curve as a solution to the LIA (3.2) may be written as [15]

$$\mathbf{R}_{\mathrm{c}}(x,t) = \frac{1}{2\kappa_0} \left[4\kappa_0^2 t \, \hat{\mathbf{i}} + \sin(2\kappa_0 x) \, \hat{\mathbf{j}} - \cos(2\kappa_0 x) \, \hat{\mathbf{k}} \right], \tag{3.6}$$

a circle of radius $\frac{1}{2\kappa_0}$ travelling along $\hat{\mathbf{i}}$ direction with a constant speed $2\kappa_0$ perpendicular to the plane of the circle. The size and shape of the space curve is preserved as it evolves. This is a model for the notable "smoke-ring" motion [39].

A soliton excitation over the plane wave ψ_{c} (3.5) generates a family of breather solutions ψ_{cb}, which reduces to the iconic breather solutions — Kuznetsov-Ma breather (KMB) [102, 103], Akhmediev breather (AB) [9], and Peregrine soliton (PS) [104] under suitable limits [11]. Detailed calculations are provided in Appendix B. The associated space curves, i.e., the soliton excitation of the smoke-ring (3.6) has been explicitly studied by Cieśliński *et al.* [15]. In the time evolution, (many) localized loops gradually grows out of a circular backbone that resembles petals of a flower opening process. These petals turn around towards the other side of the circle, and eventually merge with the circular backbone.

(a)   (b)   (c)   (d)   (e)
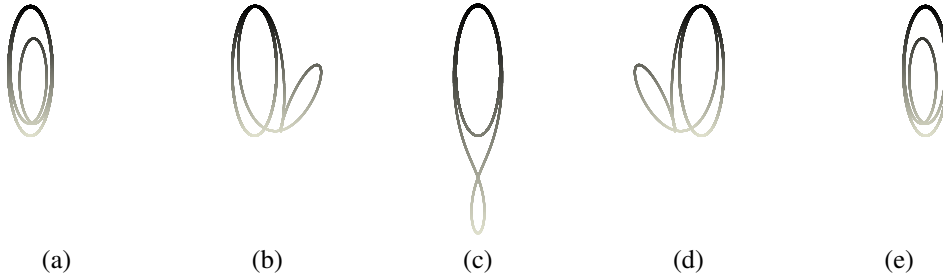
Figure 3.1: Space curves [15] associated with Kuznetsov-Ma breather (KMB). The circular backbone travels with a uniform speed. In the due course, a small *loop* comes out and goes in as shown in frames (a)–(e), which will repeat in time.

(a)   (b)   (c)   (d)   (e)
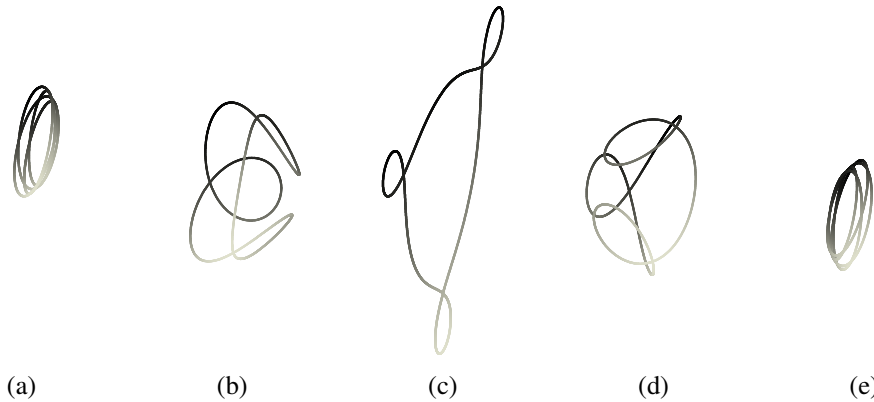
Figure 3.2: Space curves [15] associated with Akhmediev Breather (AB). The circular backbone travels with a uniform speed. In the due course, many small *loops* comes out and goes in as shown in frames (a)–(e), which resembles a "flower opening and closure". The curve shown here is a closed one owing to the suitable choice of parameters, wherein the number of loops (petals) can also be varied accordingly. However, unlike KMB (Fig. 3.1), the "flower opening and closure" occurs only at once.

(a)   (b)   (c)   (d)   (e)   (f)
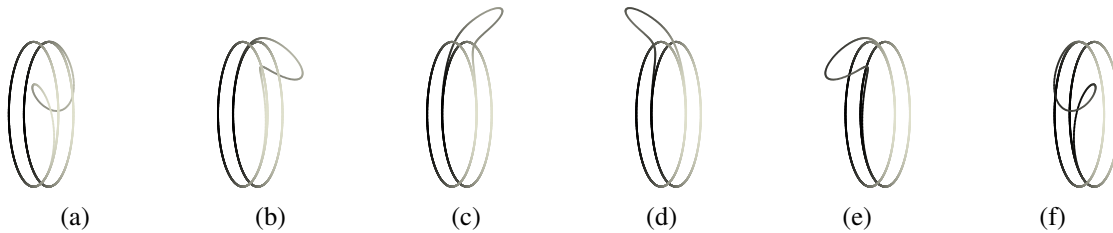
Figure 3.3: Space curves [15] — more general case with $\lambda_{0R} \neq 0$ (neither KMB nor AB). Both the ends of the curve are asymptotically circles, which coincide only with $\lambda_{0R} = 0$. A small *loop* comes out and goes in as shown in frames (a)–(f), which is a quasi periodic motion as a result of the overall rotation of the system. Self intersections do occur.

A repeating "flower opening and closure" with only a single "petal" corresponds to KMB, which is shown in Fig. 3.1. Space curves associated with Peregrine soliton (not shown here) is similar to Fig. 3.1 but the process never repeat in time. A single "flower opening and closure" with many (in fact infinite) "petals" corresponds to AB as shown in Fig. 3.2. The general case (neither KMB, nor AB) involves two parallel circles travelling together, connected by a loop that turn around both the circles in its time evolution. This is shown in Fig. 3.3. These space curves have many self-intersections throughout the time evolution which makes it impossible to observe them in real systems.

Space curve evolution generates a surface in $\mathbb{R}^3$ known as soliton surfaces (refer Sec. 2.5 for details). For instance, explicit soliton surfaces associated with the (spatially periodic) Akhmediev breather are illustrated in Ref. [80, p. 150]. Periodic solutions or breathers can also be thought of as 'bound states' of two or more ordinary solitons which are of same velocities. This can be achieved by the special choice of parameters (for the velocity) in an arbitrary N-soliton solution [30]. In space curve analogy, bound states can be seen as two loop solitons moving together with the same velocity [105], which can be designated as a travelling breather. In this process, one loop periodically revolves around the other, and generate a soliton surface as shown in Ref. [80, p. 126]. Stationary breathers as 'bound states', then corresponds to a zero velocity for both the loops (solitons). The soliton surfaces associated with stationary single soliton and travelling single soliton [80, pp. 124-125] are in sharp contrast to the above (bound state) breathers. It is worthwhile mentioning that in a geometric framework the transformation from one solution to another (auto Bäcklund transformation) can be interpreted as a passage from one soliton surface to the other [12, 45].

3.2.3 Travelling waves

There exist a special class of vortex filaments as solutions to the LIA which move steadily without deformation. The steady motion of the vortex filament as a rigid body motion has been studied extensively by Kida [106] where he obtained the solutions in terms of elliptic integrals. Vortex filaments of invariant shape are often called Kida class of solutions which are indeed the space curves associated with travelling wave solutions of NLSE [107]. A straight line, circle, helix, Hasimoto loop, curve over a doughnut surface, plane sinusoidal filament, elastica [108] all fall into the Kida class of solutions [106]. Travelling waves of NLSE in the form of periodic array of pulses can be expressed in terms of elliptic integrals [109] which tend to an ordinary single soliton when the separation be-

tween neighbouring pulses becomes infinite. Therefore, in the travelling wave spectrum (cnoidal waves), there exists two distinct limiting cases. One is a single soliton solution (or Hasimoto loop) and the other is a harmonic plane wave (or vortex ring). Bäcklund transformation of Kida class of vortex filaments [110] then reduces to soliton excitation of Hasimoto loop [46] and smoke ring [15] as two extreme limits. Curves over the doughnut surface are in general open curves, but for a suitable choice of parameters it can form torus knots [111, 112]. Unlike elliptic integral expressions as obtained by Kida, torus knot solutions can be expressed in explicit analytic form using cylindrical polar coordinates [113, Sec. 3].

3.3 Knotted breathers for the NLSE

We make use of Darboux transformation detailed in section 2.6 to obtain a new class of breather solutions to the NLSE. This breather is indeed special because of the knot structure present in its associated space curve; hence the name "knotted breather". As pointed out earlier (section 3.2.2) one can start from a non-trivial seed solution $\psi_c(x,t) = \kappa_0\, e^{2i\kappa_0^2 t}$, to arrive at the well known breather solutions that are KMB, AB or PS, using any of the standard techniques of obtaining soliton solutions. Instead, we start from a seed solution — a plane wave of uniform magnitude and space dependent phase term,

$$\psi_h = \kappa_0\, e^{i\sqrt{2}\,\kappa_0 x}, \tag{3.7}$$

for a real constant κ_0. Seed solution ψ_h when compared with (3.1), describes a space curve with curvature $2\kappa_0$ and torsion $\sqrt{2}\kappa_0$. Therefore the associated space curve is a helix, which is indicated by the suffix h in ψ_h.

3.3.1 Darboux transformation and fundamental solutions

A detailed steps for the DT technique is provided in Appendix A. In this section we present only the necessary solutions needed for the discussion.

Each solution to the NLSE (1.1) corresponds to a fundamental solution to the Lax pair (2.14). Seed solution ψ_h (3.7) corresponds to a fundamental solution $\mathbf{\Psi}_h(x, t, \lambda)$, to the below Lax pair

$$\mathbf{\Psi}_{h,x} = U_h \mathbf{\Psi}_h,$$
$$\mathbf{\Psi}_{h,t} = V_h \mathbf{\Psi}_h, \tag{3.8}$$

where $U_\mathrm{h} = U(\psi_\mathrm{h})$, and $V_\mathrm{h} = V(\psi_\mathrm{h})$. The connections $U(\psi)$ and $V(\psi)$ are given in (2.4). We explicitly write the fundamental solution $\mathbf{\Psi}_\mathrm{h}$ in the form,

$$\mathbf{\Psi}_\mathrm{h}(x,t,\lambda) = \frac{1}{\sqrt{d}} \begin{pmatrix} \varphi_1 & -\overline{\varphi}_2 \\ \varphi_2 & \overline{\varphi}_1 \end{pmatrix}, \tag{3.9}$$

where,

$$\varphi_1 = \left(a\,e^{i\Omega/2} + b\,e^{-i\Omega/2}\right)e^{i\frac{1}{\sqrt{2}}\kappa_0 x}, \quad \varphi_2 = -\left(b\,e^{i\Omega/2} + a\,e^{-i\Omega/2}\right)e^{-i\frac{1}{\sqrt{2}}\kappa_0 x},$$

$$\Omega = 2f\left(x - \sqrt{2}\mu t\right), \ f = \frac{1}{\sqrt{2}}\sqrt{\nu^2 + 2\kappa_0^2}, \ \mu = \kappa_0 - \sqrt{2}\,\lambda, \ \nu = \kappa_0 + \sqrt{2}\,\lambda, \tag{3.10}$$

$$a = i(\nu - \sqrt{2}f) - \sqrt{2}\kappa_0, \quad b = i(\nu + \sqrt{2}f) - \sqrt{2}\kappa_0, \quad d = 16f^2.$$

The Darboux matrix $G_1(\lambda)$ can be found in the form $G_1(\lambda) = \lambda\mathbf{I} + G_0$. We write it explicitly as,

$$G_1 = \begin{pmatrix} \lambda - \lambda_{0R} & 0 \\ 0 & \lambda - \lambda_{0R} \end{pmatrix} + i\,\frac{\lambda_{0I}}{\chi} \begin{pmatrix} -\xi & e^{i\sqrt{2}\kappa_0 x}(\zeta - i\,\eta) \\ e^{-i\sqrt{2}\kappa_0 x}(\zeta + i\,\eta) & \xi \end{pmatrix}, \tag{3.11}$$

wherein,

$\zeta = c_1\,\cos(\Omega_{0R}) + c_2\,\cosh(\Omega_{0I})$,
$\eta = c_3\,\sin(\Omega_{0R}) - c_4\,\sinh(\Omega_{0I})$,
$\xi = c_4\,\sin(\Omega_{0R}) + c_3\,\sinh(\Omega_{0I})$,
$\chi = c_2\,\cos(\Omega_{0R}) + c_1\,\cosh(\Omega_{0I})$,
$\Omega_0 = \Omega_{0R} + i\,\Omega_{0I} = 2f_0\left(x - \sqrt{2}\mu_0 t\right), \quad f_0 = f_{0R} + if_{0I} = \frac{1}{\sqrt{2}}\sqrt{\nu_0^2 + 2\kappa_0^2}$,
$\mu_0 = \mu_{0R} + i\mu_{0I} = \kappa_0 - \sqrt{2}\,\lambda_0, \qquad \nu_0 = \nu_{0R} + i\nu_{0I} = \kappa_0 + \sqrt{2}\,\lambda_0$,
$c_1 = 2\left(4\,\kappa_0^2 + 2\,|\nu_0|^2 + 4\sqrt{2}\,\kappa_0\,\nu_{0I} + 4\,|f_0|^2\right), \ c_2 = 2\left(4\,\kappa_0^2 + 2\,|\nu_0|^2 + 4\sqrt{2}\,\kappa_0\,\nu_{0I} - 4\,|f_0|^2\right)$,
$c_3 = 2\left(8\,\kappa_0\,f_{0I} + 4\sqrt{2}\left(\nu_{0R}\,f_{0R} + \nu_{0I}\,f_{0I}\right)\right), \ c_4 = -2\left(8\,\kappa_0\,f_{0R} + 4\sqrt{2}\left(\nu_{0I}\,f_{0R} - \nu_{0R}\,f_{0I}\right)\right)$,
and $\lambda_0 = \lambda_{0R} + i\lambda_{0I}$ is an arbitrary complex spectral parameter also known as scattering parameter in the framework of inverse scattering transforms. They also obey the conditions

$$\zeta^2 + \eta^2 + \xi^2 = \chi^2,$$
$$c_2^2 + c_3^2 + c_4^2 = c_1^2. \tag{3.12}$$

Darboux transformation gives a new $\mathbf{\Psi}_1$ by,

$$\mathbf{\Psi}_1(x,t,\lambda,\lambda_0) = \frac{1}{\sqrt{d_1}}\,G_1(x,t,\lambda,\lambda_0)\,\mathbf{\Psi}_\mathrm{h}(x,t,\lambda), \tag{3.13}$$

where $d_1 = |G_1| = (\lambda^2 + |\lambda_0|^2 - 2\lambda\lambda_{0R})$. Matrix solution $\boldsymbol{\Psi}_1$ satisfies the Lax pair

$$\begin{aligned}
\boldsymbol{\Psi}_{1,x} &= U_1\boldsymbol{\Psi}_1, \\
\boldsymbol{\Psi}_{1,t} &= V_1\boldsymbol{\Psi}_1,
\end{aligned} \tag{3.14}$$

where $U_1 = U(\psi_1)$, and $V_1 = V(\psi_1)$, with an updated ψ_1.

One may compare (3.8) and (3.14) to see how DT technique transforms $\boldsymbol{\Psi}_\text{h}$ to $\boldsymbol{\Psi}_1$ systematically. In the due course, seed solution ψ_h get updated to ψ_1 — a new breather solution to the NLSE. For calculation refer section A.2.3.

3.3.2 Explicit solution and breather profiles

Proceeding by the DT technique we arrive at the below solution, after some detailed algebra — a three parameter one-soliton solution (or one-breather) given by

$$\psi_1 = e^{i\sqrt{2}\kappa_0 x}\left(\kappa_0 - 2\,\lambda_{0I}\,\frac{(\zeta - i\,\eta)}{\chi}\right), \tag{3.15}$$

where the functions ζ, η and χ are defined below (3.11). Without any loss of generality, parameters indicating the initial position and phase of the soliton are taken to be zero.

In general, the breather solution ψ_1 (3.15) is periodic both in space and time, which is clear from the soliton profile shown in Fig. 3.4(a). This is a travelling wave with oscillating magnitude — hence the name "travelling breather". A similar profile can be seen for ψ_cb (B.22), which is the breather excitation over the plane wave ψ_c (3.5), by setting $\lambda_{0R} \neq 0$ (see for instance, Ref. [114, Figure 7]). It is worthwhile mentioning that the well known breathers AB, KMB and PS are fall into a class with $\lambda_{0R} = 0$ in ψ_cb (B.22).

Further, we show a spatially periodic profile in Fig. 3.4(b), obtained from ψ_1 (3.15) as a special case, by choosing $\lambda_{0R} = -\kappa_0/\sqrt{2}$ and $\kappa_0^2 > \lambda_{0I}^2$. Such a choice was intended to assemble soliton peaks at the $t = 0$ line. This can be explained as follows:
From the functions defined below (3.11),

$$\nu_0 = \nu_{0R} + i\,\nu_{0I} = (\kappa_0 + \sqrt{2}\,\lambda_{0R}) + i\sqrt{2}\,\lambda_{0I}. \tag{3.16}$$

When $\lambda_{0R} = -\frac{\kappa_0}{\sqrt{2}}$, one get $\nu_{0R} = 0$, and $\nu_{0I} = \sqrt{2}\,\lambda_{0I}$. Substituting this in f_0, it gives,

$$f_0 = f_{0R} + if_{0I} = \frac{1}{\sqrt{2}}\sqrt{\nu_0^2 + 2\,\kappa_0^2} = \sqrt{\kappa_0^2 - \lambda_{0I}^2}. \tag{3.17}$$

36

(a) Travelling breather

(b) Spatially periodic breather

(c) Temporally periodic breather

(d) Rogue breather
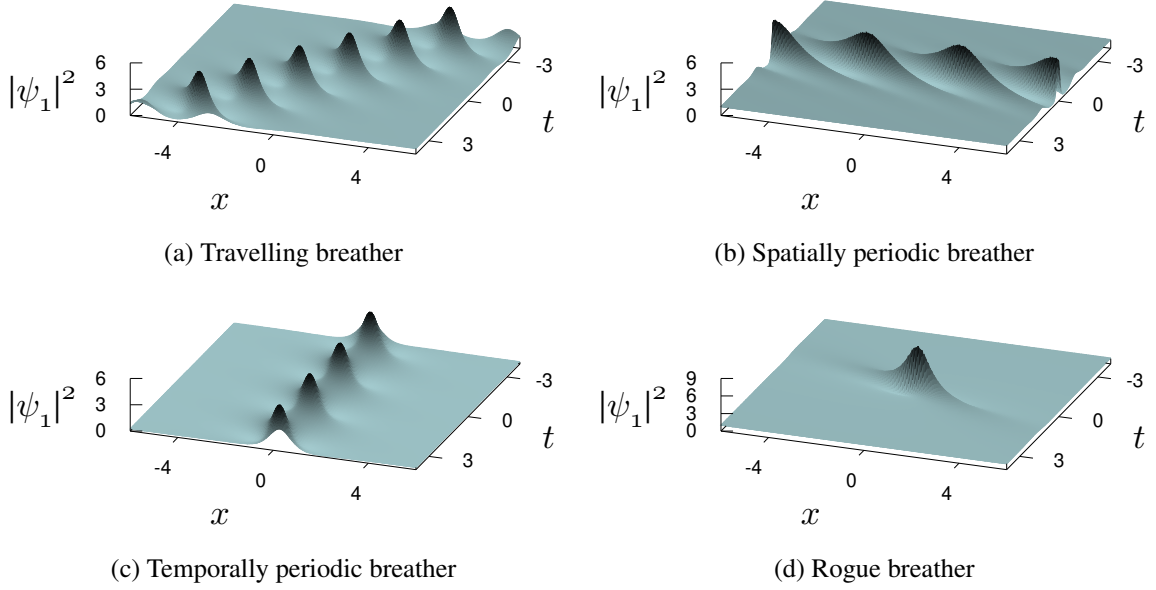
Figure 3.4: Soliton profile of ψ_1 (3.15) in the $x - t$ plane. (a) Breather periodic in both space and time, for $\kappa_0 = 0.8$, $\lambda_0 = -0.1 + 0.7\,i$ (b) Akhmediev type breather obtained by the condition $\lambda_{0R} = -\kappa_0/\sqrt{2}$ and $\kappa_0^2 > \lambda_{0I}^2$. Here $\kappa_0 = 1.0$, $\lambda_{0I} = 0.6$ (c) Kuznetsov-Ma type breather, arises as a special case for $f_{0I}\,\mu_{0R} + f_{0R}\,\mu_{0I} = 0$. This condition is met by setting, $\kappa_0 = 0.5$, $\lambda_0 = -0.07 + 0.8\,i$ (d) Rogue event as a limiting case of Akhmediev type breather shown in (b), choosing $\lambda_{0I} \sim \kappa_0$.

When $\kappa_0^2 > \lambda_{0I}^2$,

$$f_{0R} = \sqrt{\kappa_0^2 - \lambda_{0I}^2}, \text{ and } f_{0I} = 0 \tag{3.18}$$

Periodicity and localization arises in ψ_1 (3.15) via trigonometric and hyperbolic functions respectively. Hence, we write the general expression for Ω_{0R} and Ω_{0I} explicitly as,

$$\begin{aligned}
\Omega_{0R} &= 2\,f_{0R}\,x + 2\sqrt{2}\,t\,(f_{0I}\,\mu_{0I} - f_{0R}\,\mu_{0R}), \\
\Omega_{0I} &= 2\,f_{0I}\,x - 2\sqrt{2}\,t\,(f_{0I}\,\mu_{0R} + f_{0R}\,\mu_{0I}).
\end{aligned} \tag{3.19}$$

As per the choice made, $f_{0I} = 0$ from (3.18), thereby no x dependence in Ω_{0I} (3.19). Specifically, $\Omega_{0I} \equiv \Omega_{0I}(t)$, a function of time alone. In brief, the condition $\lambda_{0R} = -\frac{\kappa_0}{\sqrt{2}}$ and $\kappa_0^2 > \lambda_{0I}^2$ results in a localization at $t = 0$ line in the $x - t$ plane as shown in Fig. 3.4(b).

Keeping the same condition one can obtain a rogue event as a limiting case. From Ω_{0R} (3.19), the periodicity along x can be found to be π/f_{0R}, which tends to infinity for $\lambda_{0I} \sim \kappa_0$. This unveils the rogue nature of the breather solution as shown in Fig. 3.4(d).

In Fig. 3.4(c), the profile is temporally periodic. For this, one has to make Ω_{0I} a function

of x alone so that all the peaks gather together at the $x = 0$ line. From Ω_{0I} (3.19), this can be achieved by setting $f_{0I}\mu_{0R} + f_{0R}\mu_{0I} = 0$.

3.4 Galilean transformation

Even though the seed solutions ψ_c (3.5) and ψ_h (3.7) appear to be qualitatively different, they are related to each other through a Galilean transformation. It may be recalled that under the Galilean transformation

$$x \to x - vt, \quad t \to t, \tag{3.20}$$

the NLSE is invariant [11] through an additional phase change to the field function,

$$\psi \to \psi \exp\left[i(vx/2 - v^2 t/4 + v_0)\right], \tag{3.21}$$

where v and v_0 are arbitrary real constants. One can verify that, the plane wave solution ψ_c transforms to ψ_h under the Galilean transformation for $v = 2\sqrt{2}\kappa_0$ and $v_0 = 0$. According to the Hasimoto map (3.1), seed solution ψ_c has constant curvature but zero torsion which implies a circle. Seed solution ψ_h is mapped to a helix where both the curvature and torsion are non-zero constants. Thus the circle transforms to a helix. Specifically, the curve picks up a torsion under Galilean transformation. Note that the transformation (3.21) can only only be applied on the complex field ψ, but on the associated space curve, the corresponding transformation is not as straight forward.

We have described in the previous section, a spatially periodic breather for $\lambda_{0R} = -\frac{\kappa_0}{\sqrt{2}}$ and $\kappa_0^2 > \lambda_{0I}^2$. A simplified expression for this "Akhmediev type breather" is given by,

$$\psi_{\text{GAB}} = -\kappa_0\, e^{i\sqrt{2}\kappa_0(x-x_0)}\, \frac{\cosh(rt - 2i\phi) - \cos\phi\,\cos(q(x - vt))}{\cosh(rt) - \cos\phi\,\cos(q(x - vt))}, \tag{3.22}$$

where, $q = 2\kappa_0 \sin(\phi)$, $r = 2\kappa_0^2 \sin(2\phi)$, $v = 2\sqrt{2}\kappa_0$, $\phi = \cos^{-1}(\lambda_{0I}/\kappa_0)$ and $x_0 = \pi/q$. Detailed steps are provided in section A.3 of Appendix A. It is clear that the above breather is localized in t and periodic in x. For a comparison we write explicitly, the Akhmediev breather (for details, refer section B.4),

$$\psi_{\text{AB}} = -\kappa_0 e^{2i\kappa_0^2 t}\, \frac{\cosh(rt - 2i\phi) - \cos\phi\,\cos(qx)}{\cosh(rt) - \cos\phi\,\cos(qx)}, \tag{3.23}$$

38

where, $q = 2\kappa_0 \sin(\phi)$, $r = 2\kappa_0^2 \sin(2\phi)$ and $\phi = \cos^{-1}(\lambda_{0I}/\kappa_0)$. Comparing (3.22) with (3.23), one can infer that a Galilean transformation of ψ_{AB} leads to ψ_{GAB}.

Galilean transformed Akhmediev Breather — ψ_{GAB}, initially obtained by Salman [29], is therefore a special case of the breather solution we have presented here, upto a scaling and suitable choice of parameters. An analogue of the Peregrine soliton as a limiting case of Galilean transformed Akhmediev breather is studied by Salman in Ref. [115], by setting $\lambda_{0I} \sim \kappa_0$ in ψ_{GAB},

3.5 Knotted space curves as solutions to the LIA

Now we will discuss the geometric side of the soliton solution by presenting the space curves that are associated with seed solution ψ_h (3.7) and its Bäcklund transformation ψ_1 (3.15). Hasimoto function (3.1) for ψ_h describes a helix via intrinsic quantities κ and τ in a coordinate independent way. Explicit expression for the space curve as a solutions to the LIA (3.2) can be constructed as detailed in section 2.4 and 2.5.

3.5.1 Helix as a seed curve

The space curve $\mathbf{R}_h$ associated with the seed solution ψ_h (3.7) is given by the Sym-Tafel formula

$$\mathbf{R}_h = \lim_{\lambda \to 0} \mathbf{\Psi}_h^{-1} \mathbf{\Psi}_{h,\lambda}, \tag{3.24}$$

where $\mathbf{\Psi}_h$ (3.9) is the corresponding fundamental solution. The subscript λ denotes the differentiation with respect to λ. Following a straight forward calculation and simplification, we write the seed curve in $\mathbb{R}^3$ explicitly as,

$$\mathbf{R}_h = \frac{1}{3}\left[\left(\sqrt{3}(x + 2\sqrt{2}\kappa_0 t)\right)\hat{\mathbf{i}} + \left(\frac{1}{\kappa_0}\sin\theta\right)\hat{\mathbf{j}} - \left(\frac{1}{\kappa_0}\cos\theta\right)\hat{\mathbf{k}}\right], \tag{3.25}$$

where $\theta = \sqrt{6}\kappa_0(x - \sqrt{2}\kappa_0 t)$. The helix has a pitch $\sqrt{2}\pi/(3\kappa_0)$ and radius $1/(3\kappa_0)$ which are independent of time. This is a Kida class of vortex filament having a screw motion with translation along its axis with velocity $2\sqrt{\frac{2}{3}}\kappa_0$, and a rotation about its axis with period

$$T_0 = \pi/(\sqrt{3}\kappa_0^2). \tag{3.26}$$

Curvature and torsion can be directly computed from (3.25) yielding $\kappa = 2\kappa_0$ and $\tau = \sqrt{2}\kappa_0$, as expected.

39

3.5.2 Breather excitation over the helix

In the same manner, the space curve associated with the breather solution ψ_1 (3.15) can be obtained by

$$\mathbf{R}_1 = \lim_{\lambda \to 0} \mathbf{\Psi}_1^{-1} \mathbf{\Psi}_{1,\lambda}, \tag{3.27}$$

where $\mathbf{\Psi}_1$ is the fundamental solution given in (3.13). The explicit expression after a straightforward calculation can be shown to be

$$\mathbf{R}_1 = \mathbf{R}_{\mathrm{h}} + \frac{\lambda_{0I}}{|\lambda_0|^2 \chi} \left[-\frac{(\sqrt{2}\eta + \xi)}{\sqrt{3}} \hat{\mathbf{i}} + \left(-\zeta \sin\theta + \cos\theta \frac{(\eta - \sqrt{2}\xi)}{\sqrt{3}} \right) \hat{\mathbf{j}} \right.$$
$$\left. + \left(\zeta \cos\theta + \sin\theta \frac{(\eta - \sqrt{2}\xi)}{\sqrt{3}} \right) \hat{\mathbf{k}} \right], \quad (3.28)$$

where the functions ζ, η, ξ and χ were defined below (3.11), and θ is defined below (3.25).

The second term in (3.28) represents a rotating loop sliding down the helical backbone $\mathbf{R}_{\mathrm{h}}$ (Fig. 3.5). If the loop size is too small as compared to the pitch of the helix, motion of the loop locally resembles Hasimoto loop to a certain extent. Unlike the loop soliton motion on a filament with zero (or nearly zero) curvature, this travelling loop (for suitable parameter) intersects with the helical backbone in a periodic fashion. With a reasonable loop size which can be tuned through parameter value λ_{0I}, self intersections occur, leading to the formation of a *knot* structure, which is quite unexpected for an ordinary loop soliton dynamics.

3.5.3 Periodic knot formation

The behaviour of the space curve displays a periodic nature where one can identify a cycle with three successive intersections. Space curve dynamics is shown in Fig. 3.5 with five frames taken from an entire cycle. The space curve carries a *loop* between the first two intersections, whereas the curve has a *knot* for the remaining time. One cycle with period T_{total} is thus subdivided into a *loop* phase and a *knot* phase with periods T_{loop} and T_{knot}, respectively. Soliton profile at the same instant of time is also provided along with the curve for a better comparison. The *loop* phase is characterized by a single large soliton peak in contrast to the slowly varying small double peak of the *knot* phase. This can be understood from the Hasimoto map (3.1) which relates the curvature of the associated space curve with the magnitude of the soliton solution. When the curvature has a localized peak, the curve takes a quick turn results in a *loop*. Whereas a *knot* structure in an extended open curve is

40

reasonable with a slowly varying curvature with two small nearby peaks.

Generally the space curve presented here are periodic both spatially and temporally, as that of the breather profile shown in Fig. 3.4 (a). Along with the period attributed to the breather solution, background seed also has its own period, which is visible in the curve picture as the rotation period of the helical backbone T_0 (3.26), that is determined by κ_0 alone. T_0 is in general incommensurate with the above mentioned T_{total}, and as a consequence the space curve shown in Fig. 3.5 (a) and (e) are same but globally rotated. In

(a) $t = t_1$ (b) The *loop* phase   (c) $t = t_2 = t_1 + T_{loop}$

(d) The *knot* phase   (e) $t = t_2 + T_{knot} = t_1 + T_{total}$
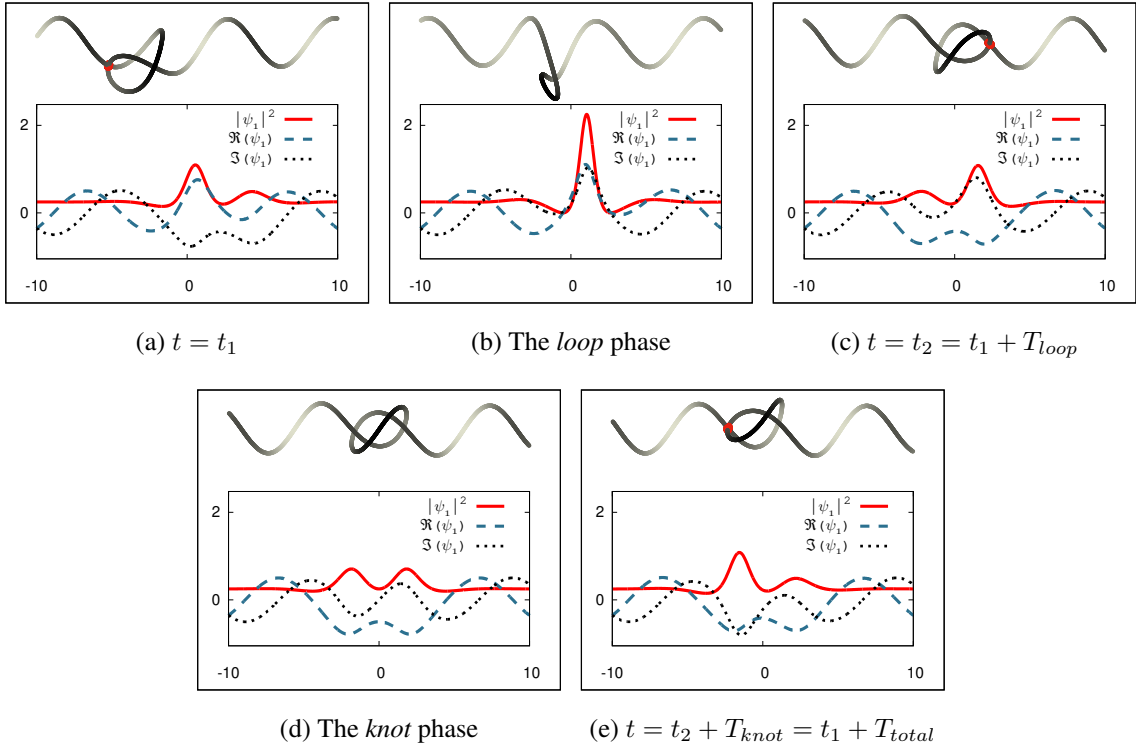
Figure 3.5: The space curves $\mathbf{R}_1$ associated with the breather solution ψ_1, and the corresponding energy ($|\psi|^2(x)$) profile, through an entire period of its evolution. The real and imaginary parts of ψ_1 are indicated by (blue) dashed and (black) dotted lines respectively. Successive self intersections marked by red dot on the curves. For this choice of parameters, $\kappa_0 = 0.5$ and $\lambda_0 = 0 + 0.5i$, the filament forms a *loop* between the first two intersections, (a) and (c), whereas it forms a *knot* for the remaining time, i.e., between (c) and (e). Thus, the period T_{total} is subdivided into two phases — the *knot* phase with period T_{knot}, and the loop phase with period T_{loop}. Energy localization is more profound in the *loop* phase (with a large single peak) than in the *knot* phase (with two smaller peaks). The curve in (a) is same as (e), but for a global rotation due to the period T_{total} being incommensurate with the rotation period T_0 of the helical backbone. For detailed animation, see the supplementary material: knot.avi.

fact, an analytical expression for time period of the curve evolution, T_{total} can be derived explicitly.

3.5.4 Analysis of time periods

It can be understood from Fig. 3.5 that T_{total} is same as the time difference between any two nearby peaks in the breather profile. Recalling the breather expression ψ_1 (3.15), one can find that the peak occurs at $\Omega_{0I} = 0$, as it is the argument of hyperbolic functions, whereas Ω_{0R} being responsible for the periodicity via trigonometric functions. They are explicitly given in (3.19). When using a more convenient coordinates, obtained by the transformation,

$$x' \to \frac{\sqrt{2}}{f_{0I}}(f_{0I}\,\mu_{0R} + f_{0R}\,\mu_{0I})\,t, \quad t' \to t, \tag{3.29}$$

it can be seen that,

$$\Omega_{0R}(x', t') = \frac{2\sqrt{2}\mu_{0I}|f_0|^2}{f_{0I}}\,t, \quad \Omega_{0I}(x', t') = 0. \tag{3.30}$$

It follows that the period

$$T_{total} = \frac{2\pi}{\Omega_{0R}} = \frac{\pi f_{0I}}{\sqrt{2}\mu_{0I}|f_0|^2}, \tag{3.31}$$

which depends on λ_{0R}, λ_{0I} and κ_0, through f_0 and μ_0 defined below (3.15).

However, it is cumbersome to obtain an expression for T_{knot} and T_{loop} analytically due to the complexity of the curve expression. Therefore we rely on a numerical approach by evolving the curve $\mathbf{R}_1$ (3.28). This is to investigate the dependence of time periods on the parameter λ_{0I}, keeping the other two fixed. For ease of analysis we set $\lambda_{0R} = 0$, thus providing a constant speed (however, non-zero) for the travelling loop. While κ_0 governs the helical backbone features, it is the relative value of κ_0 and λ_{0I} that determines the size and shape of the loop. We numerically evolve the curve (3.28) in time, keeping the parameters fixed, and successive intersections are recorded, the difference of which yields either T_{knot} or T_{loop}. Classifying a *knot* (or *unknot*) directly from its position vector computationally (without viewing) is quite difficult in geometry [116]. Viewing the curve at the starting position helps to assign the time difference, either as T_{knot} or T_{loop} accordingly (exceptional cases are taken care).

Observations are shown in the Fig. 3.6. Generally $T_{loop} > T_{knot}$, i.e, *knots* are always short lived as compared to the *loop* phase. For certain intermediate ranges of λ_{0I}, the curves does not make any self intersections. In Fig. 3.6, we mark this range of values as 'gray
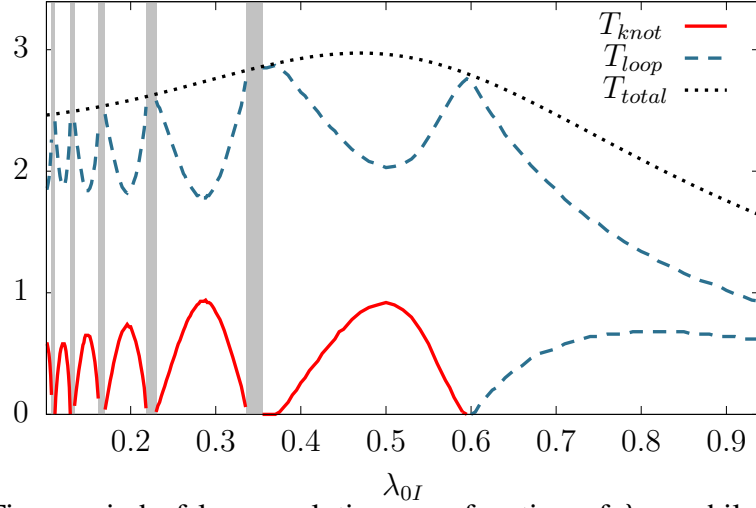
Figure 3.6: Time period of loop evolution as a function of λ_{0I}, while κ_0 and λ_{0R} are held constant. In the course of time (see Fig. 3.5), self intersections occur periodically, switching a *loop* phase into a *knot* phase, with respective time periods T_{loop} (dashed lines) and T_{knot} (solid lines). $T_{total} = T_{loop} + T_{knot}$. Generally $T_{loop} > T_{knot}$, i.e, *loop* phase is dominating over the *knot* phase. No knots are formed for values beyond $\lambda_{0I} = 0.6$ (at $\kappa_0 = 0.5, \lambda_{0R} = 0$), although intersections do occur. No intersections are noticed for certain intermediate ranges of λ_{0I}, indicated by gray bands. There are points where T_{knot} vanishes, corresponding to two simultaneous self intersections. See Fig. 3.7 for details.

(a) $\lambda_{0I} = 0.35$ (b) $\lambda_{0I} = 0.22$ (c) $T_{total} = T_{loop}, T_{knot} = 0$
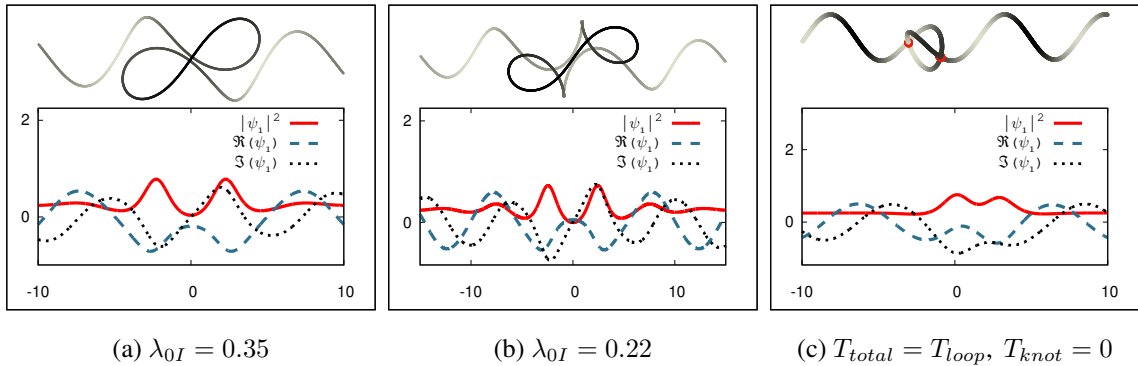
Figure 3.7: (a) A loop with two sub-winding, or 'petals', for $\lambda_{0I} = 0.35$ which falls under the first (prominent) gray band shown in Fig. 3.6 for which no self intersections are noticed. The size, shape and overall motion of the loop are fit in such a way that prevents any self intersection as the loop rotates about the helix. (b) As λ_{0I} is reduced the number of petals increases, here seen with three for $\lambda_{0I} = 0.22$, which falls under the second (prominent) gray band of Fig. 3.6. (c) Two simultaneous intersections (shown here for $\lambda_{0I} = 0.6$), with a vanishing T_{knot}. For detailed animation, see the supplementary materials: no_int.avi for (a), two_int.avi for (c).

bands'. Curves corresponding to this 'gray band' parameter values are non intersecting curves, as shown in Fig. 3.7 (a) for the first 'gray band', and (b) for the second 'gray band'. Note that the bands are numbered from right, and there are many more towards left. As λ_{0I} decreases, size of the loop increases, and involves sub-windings, or 'petals', which makes the motion slightly complicated. Number of 'petals' in each 'gray bands' increases as we moves towards the lower values of λ_{0I}.

Beyond certain value of λ_{0I} no *knots* are formed, although intersections do occur. Precisely, for $\lambda_{0I} > 0.6$, there are no *knots* as seen in Fig. 3.6. The curve for $\lambda_{0I} = 0.6$ is shown in Fig. 3.7 (c), which indicate two simultaneous self intersections. This is also an example for curves for which T_{knot} vanishes, on account of the two intersections occurring simultaneously. As λ_{0I} increases, the size of the loop decreases to a value smaller that the radius of the helix, so that it fails to make *knot* structure.

3.5.5 Soliton surfaces

As elaborated in section 2.5, the geometric nature of soliton solution can be seen in soliton surfaces. Soliton surface associated with the breather solution ψ_1 (3.15) is presented in Fig. 3.8. This is constructed by foliation of the *knotted* space curve previously discussed in Fig. 3.5.
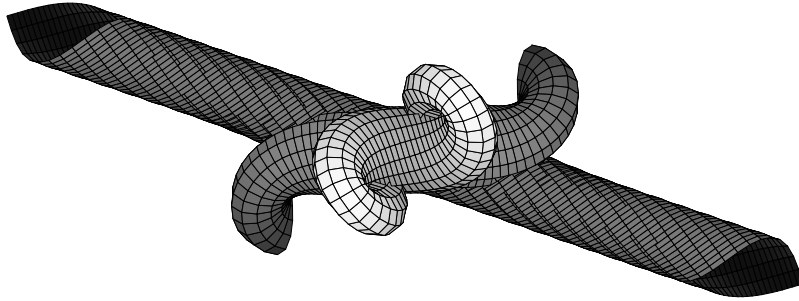
Figure 3.8: Soliton surface generated by the *knotted* space curve. The choice of parameters, $\kappa_0 = 0.5$ and $\lambda_0 = 0 + 0.5i$, is same as that of Fig. 3.5.

3.6 Discussion

It is tempting to interpret the space curves presented here as a vortex filament in fluids under LIA scheme. However we caution that the LIA is not an appropriate model to describe vortex motion when non-local interactions are predominant. LIA deals with the velocity

on the filament induced by its own vorticity disregarding long range effects. The more rigorous treatment requires invoking the Biot-Savart law to compute the velocity field at a given point induced by the vortex filament(s) in question [117, 118].

In the case of helical vortices, the velocity field induced in its vicinity [119], and the velocity induced on the filament itself [120] have been extensively studied in literature. An extended LIA for helical a vortex is suggested by incorporating the velocity induced by distant parts of the filament, which gives reasonable approximation for low pitch helices [121]. A detailed experimental study has already been performed by creating helical vortices under controlled conditions in a vortex chamber, wherein left-handed, right-handed, stationary, precessing, double helix and entangled helices have been studied [40].

| (a) | (b) | (c) | (d) | (e) |
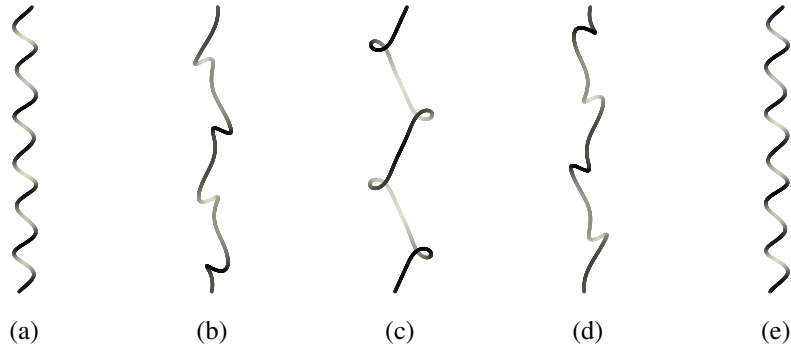
Figure 3.9: Time evolution of the space curve associated with Galilean transformed Akhmediev breather ψ_{GAB} (3.22). The breather excitation is spatially periodic but localized in time. Obtained from $\mathbf{R}_1$ (3.28) by the condition $\lambda_{0R} = -\kappa_0/\sqrt{2}$ and $\kappa_0^2 > \lambda_{0I}^2$. Specifically $\kappa_0 = 1.0$, $\lambda_{0I} = 0.6$, same as that of the breather profile shown in Fig. 3.4 (b). This space curve evolution has no self-intersection. For detailed animation, see the supplementary material: curve_gab.avi .

As discussed in Sec. 3.3, a special case of the breather solution ψ_1 (3.15) presented here is related to the Akhmediev breather through a Galilean transformation. This special case given in (3.22), was obtained earlier by Salman [29] by invoking such a transformation from the well known Akhmediev breather. The corresponding vortex filament is constructed using Hasimoto map to investigate propagation of breathers along superfluid vortex. Spatial periodicity present in the Akhmediev breather appears in the space curve as periodic *loops*. These *loops* grows slowly in time, out of a uniform background – a helical backbone in this case. After initializing the curve, a numerical integration can be carried out using more realistic models like Biot-Savart law and Gross-Pitaevskii equation, along with the LIA dynamics. Vortex bifurcation and re-connection process are incorporated in

the numerical study accordingly, which leads to the formation of isolated vortex rings out of each individual *loops*. The vortex ring thus formed moves away from the base curve owing to its induced velocity, thereby suggesting a mechanism for transfer of energy concentrated in the vortex, to far away regions of the superfluid. A more detailed discussion of space curves associated with this 'Akhmediev like' breather is given by Salman [115] where the space curves associated with Peregrine soliton as a limiting case is also given along with soliton profiles. We reproduce the space curves associated with ψ_{GAB} (3.22) and presented in Fig. 3.9, which shows spatially periodic breather excitations in the time evolution. We emphasize that *knotted* space curve presented in this work cannot be produced from Akhmediev breather for any choice of parameter values.

| (a) | (b) | (c) | (d) | (e) |
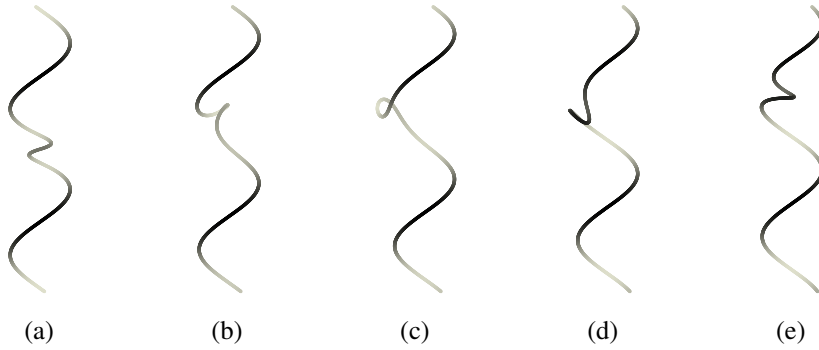
Figure 3.10: Time evolution of a travelling loop without self-intersection. Space curve $\mathbf{R}_1$ (3.28) for $\kappa_0 = 0.5$, $\lambda_0 = -0.6 + 1.2i$. For detailed animation, see the supplementary material: loop.avi .

Dynamics of a loop in a helical vortex is observed experimentally in real fluid in the context of vortex re-connection studies. Helical vortex is made under controlled conditions wherein an isolated loop responsible for the self intersection turns into an isolated vortex ring through a vortex re-connection process. Images taken from this study by Alekseenko *et al.* [122] are similar to the curve dynamics we have presented here to some extent (see for instance, Fig. 3.5 and Fig. 3.10 respectively for intersecting and non-intersecting travelling *loop*). However, in their studies, one of the turns of the helix begins to rise, and become a loop, which has no correlation with the space curve dynamics discussed here. They have shown that right after the vortex re-connection, Kelvin waves — wave modes arising from perturbation of vortex tubes, are formed [123]. In these studies, the self-intersections occur without the presence of any external vortices. Relying on the similarities, it is reasonable to suggest that the space curve given in this work would be helpful to study kelvin waves of various modes. One has to incorporate vortex re-connection events along with a nu-

merical integration of Biot-Savart law as described in Ref. [29]. Vortex rings formed via re-connection are rarely linked with the helical vortex [122], and is of size nearly double as that of isolated rings. This could be modelled by tuning the loop size accordingly in such a numerical study.

3.7   Conclusion

Being a logical connection well rooted in the mathematical framework of soliton theory, the geometrical space curves that are associated with non-linear Schödinger equation (NLSE) is of academic interest in addition to its physical relevance as an approximate description of a vortex filament in fluids. What is narrated in the space curve is the true essence of the solution, which in fact cannot be revealed merely by looking at the soliton profile. In this work we found a new class of breather solution to the NLSE, which is in a geometrical language, one-soliton excitation of helical space curve, and have shown that it has a *knot* structure, albeit short-lived. Helix is more general as compared to a line or a circle because both the curvature and torsion of a helix are non-zero. Soliton excitation in such a background may possess general features so far not witnessed in other existing space curves. There exist space curves in the form of stable *knots* of Kida class. However we emphasize that they are associated with periodic solutions to the NLSE which are qualitatively different from a breather solution.

The spatially periodic case of the knotted breather presented here is shown to have a relation with Akhmediev breather via Galilean transformation. Their background space curves are a helix and a circle respectively. A circle and a helix are associated with plane wave solutions that are related through a Galilean transformation. It is known that, a Galilean transformation of the Akhmediev breather leads to a spatially periodic breather. We show that, the same can be achieved from a seed solution associated with a circle, through a Galilean transformation followed by a Darboux transformation, for suitable parameter values. The general question of permutability of the two types of transforms, however remains open.

Bifurcation and vortex re-connection in fluids or superfluids are beyond the scope of LIA scheme. Nevertheless non-intersecting space curves presented here are in agreement with the experimental observation of helical vortex and its excitations, to a certain extent. Nowadays *knotted* vortices are not just a mathematical curiosity as the vortices in the form of trefoil *knot* in real fluids have been created in laboratory recently [124].

Since NLSE is integrable, and is being used to model a number of physical systems,

this *knotted* breather is promising, and it demands an in-depth study to uncover its physical interpretation in various fields.

Chapter 4

Rogue waves in Heisenberg ferromagnet

4.1 Introduction

Classical HF spin chain and nonlinear Schrödinger equation (NLSE) are gauge equivalent. They speak the same fact in different languages. For NLSE, the breather solutions are quite familiar. We examine the corresponding breather solutions in the HF spin chain. We are trying to answer the following question in its generality: what does a *breather* means to a spin chain?

The procedure is as follows: we investigate the NLSE first, starting from a plane wave $\psi_\mathrm{c} = \kappa_0 e^{2i\kappa_0^2 t}$ as seed solution. Breather solution is found using DT technique. Corresponding solution to the linear system (Lax pair) is also obtained. Using the gauge equivalence relation, the required spin filed (solution to the HF model) is explicitly constructed. Spatially periodic case is studied, wherein a rogue mode is identified for suitable parameters. Spin chain and its dynamics is visualized using detailed plots.

We observe a peculiar geometrical feature — the *belt trick* demonstrated by the spin chain in the process of breather excitation. The spin breather considered in our study, a special *magnon* mode, is essentially a counterpart of Akhmediev breather. Therefore the nonlinear process observed here is nothing but a *recurrence* phenomena. Since Lax pair solution is an $\mathrm{SU}(2)$ group element, breather excitation is also visualized in the group manifold. Interestingly, the breather mode helps to divide the solution space into two topological sectors with distinct energy bounds.

4.2 1-Soliton in classical HF spin chain

First, we briefly recall the interconnection between classical HF model and the NLSE. A detailed description is provided in sections 2.3 and 2.4. We consider the one-dimensional nonlinear Schrödinger equation (NLSE) of focusing type given by,

$$i\psi_t + \psi_{xx} + 2|\psi|^2\psi = 0. \tag{4.1}$$

This system is gauge equivalent to the 1-d classical HF model, for which the dynamics is described by one dimensional Landau Lifshitz Equation (LLE),

$$\hat{\mathbf{S}}_t = \hat{\mathbf{S}} \times \hat{\mathbf{S}}_{xx}, \qquad (\hat{\mathbf{S}}^2 = 1). \tag{4.2}$$

Lax representation for the NLSE gives an associated linear system (2.14) known as Lax pair. Therefore, every solution ψ to the NLSE corresponds to a matrix solution $\mathbf{\Psi}$ to its Lax pair. Gauge equivalence provides a systematic way of constructing a spin configuration by (2.15), $\mathbf{S} = \lim_{\lambda\to 0} \mathbf{\Psi}^\dagger \sigma_3 \mathbf{\Psi}$. This spin field satisfies 1-d LLE, where $\mathbf{S} = S_1\sigma_1 + S_2\sigma_2 + S_3\sigma_3 \equiv S_1\hat{\mathbf{i}} + S_2\hat{\mathbf{j}} + S_3\hat{\mathbf{k}}$. Energy density of the spin field can be expressed as [19],

$$E = \hat{\mathbf{S}}_x^2 = 4|\psi|^2. \tag{4.3}$$

The trivial solution $\psi_l = 0$ has its counterpart $\hat{\mathbf{S}}_l = 0\hat{\mathbf{i}} + 0\hat{\mathbf{j}} + 1\hat{\mathbf{k}}$, which is a static field. Suffix l indicates 'line', its associated space curve (Fig. 1.3 (a)). Energy density (4.3) is zero because the spins are strictly parallel throughout the spin chain. Starting from this zero *seed* solution, a 1-soliton can be obtained which is the well known travelling wave of 'secant-hyperbolic' form [30],

$$\psi_{\mathrm{sh}} = 2\lambda_{0I}\exp\left(i\mu_{0R}\right)\operatorname{sech}\mu_{0I}, \tag{4.4}$$

where $\mu_0 = \mu_{0R} + i\mu_{0I} = 2\lambda_0 x - 4\lambda_0^2 t$, and $\lambda_0 = \lambda_{0R} + i\lambda_{0I}$ is the complex scattering parameter that determines the amplitude and velocity of the soliton. Two more constants indicating the initial phase and position has been set to zero without loss of generality. For a qualitative description of the spin field, notice the z-component of the corresponding spin field [35, 33],

$$S_3 = 1 - \frac{2\lambda_{0I}^2}{|\lambda_0|^2}\operatorname{sech}^2(2\lambda_{0I}x - 8\lambda_{0I}\lambda_{0R}t), \tag{4.5}$$

tends to '1' except for a small region of the spin chain at any instant of time. This indicates

a localized disturbance (or excitation) in a 1-d isotropic spin field, which travels with a uniform speed. This is the 1-soliton excitation in classical HF model shown in Fig. 1.2. Energy density is in the form $\mathrm{sech}^2(x - ct)$, where c is the velocity. Total energy $\int E dx$, is finite even for an infinite spin chain.

4.3   Seed solution: a spatially periodic spin chain

Apart from travelling waves, the NLSE also allows *breather* solutions. A solution is said to be a breather if the field variable is localized, and in addition has a periodic nature, either in space or in time. There exist some well known breather solutions to the NLSE: the time periodic Kuznetsov-Ma breather(KMB) [102, 103], spatially periodic Akhmediev breather (AB) [9] and a special case of both — Peregrine soliton (PS) [104], for which periodicity in space and time are infinite. A breather solution is obtained using inverse scattering transform (or any other standard method for obtaining soliton solutions), if one start with a seed solution,

$$\psi_{\mathrm{c}} = \kappa_0 \, e^{2i\kappa_0^2 t}, \tag{4.6}$$

for an arbitrary real constant κ_0. Suffix c indicates the associated space curve, a 'circle' (Fig. 1.3 (b)). Seed solution ψ_{c} acts as a uniform background for the breather solution, in contrast to the zero background as in the case of 'secant-hyperbolic' soliton. In order to construct the spin configuration associated with ψ_{c}, the corresponding matrix solution to the Lax pair is required (for details refer section 2.3).

4.3.1   Seed solution and the Lax pair

Seed solution ψ_{c} corresponds to a matrix solution $\mathbf{\Psi}_{\mathrm{c}}$ to the below Lax pair

$$\begin{aligned} \mathbf{\Psi}_{\mathrm{c},x} &= U_{\mathrm{c}} \mathbf{\Psi}_{\mathrm{c}}, \\ \mathbf{\Psi}_{\mathrm{c},t} &= V_{\mathrm{c}} \mathbf{\Psi}_{\mathrm{c}}, \end{aligned} \tag{4.7}$$

where $U_{\mathrm{c}} = U(\psi_{\mathrm{c}})$, and $V_{\mathrm{c}} = V(\psi_{\mathrm{c}})$. The connections $U(\psi)$ and $V(\psi)$ are given in (2.4). We explicitly write the matrix solution $\mathbf{\Psi}_{\mathrm{c}}$ in the form,

$$\mathbf{\Psi}_{\mathrm{c}}(x, t, \lambda) = \frac{1}{\sqrt{d}} \begin{pmatrix} \varphi_1 & -\overline{\varphi_2} \\ \varphi_2 & \overline{\varphi_1} \end{pmatrix}, \tag{4.8}$$

51

wherein,

$$\varphi_1 = \left(e^{-i\omega/2} + i\,\frac{(\lambda - p)}{\kappa_0}\,e^{i\omega/2} \right) e^{i\kappa_0^2 t}, \; \varphi_2 = \left(i\,\frac{(\lambda - p)}{\kappa_0}\,e^{-i\omega/2} + e^{i\omega/2} \right) e^{-i\kappa_0^2 t},$$
$$\omega = 2\,p(x + 2\lambda t), \quad p = (\kappa_0^2 + \lambda^2)^{1/2}, \quad d = 4(\kappa_0^2 + \lambda^2 - \lambda p)/\kappa_0^2. \tag{4.9}$$

We have assumed the form of φ_1 and φ_2 in (4.8), similar to the form given by Yan-Chow Ma [103, Sec. II], then substituted in (4.7) to obtain its exact expression as given in (4.9).

4.3.2 Explicit expression for the seed spin

Spin configuration associated with ψ_c (4.6) can be obtained using the expression,

$$\mathbf{S}_c = \lim_{\lambda \to 0} \mathbf{\Psi}_c{}^\dagger \sigma_3 \mathbf{\Psi}_c \tag{4.10}$$

where $\mathbf{\Psi}_c$ is given in (4.8). Following a straight forward calculation the spin configuration can be written in the vector form as,

$$\hat{\mathbf{S}}_c = \cos(2\kappa_0 x)\hat{\mathbf{j}} + \sin(2\kappa_0 x)\hat{\mathbf{k}}. \tag{4.11}$$

Without loss of generality, two constants indicating global rotation and translation are set to zero. This "seed" spin is a static field (independent of t) with energy density $4\kappa_0^2$. Spin vectors are arranged in one dimension whereas each of them has the freedom to trace a curve over a (unit) sphere. The state space of the system is then $S^2 \times S^1$.

Spatial periodicity of the spin field makes it easier to look at a repeating segment of size L, with $\kappa_0 = n\pi/L$, where n is any integer. The continuous spin chain of size L as in (4.11), thus corresponds to a finite total energy,

$$E_0 = (2n\pi)^2/L. \tag{4.12}$$

Such a repeating segment for $n = 2$ is shown in Fig. 4.1 (a), where spins at the boundaries are identified. This enables us to think of a circular lattice of length L, upon which the spins are fixed. This circular lattice will be much helpful in our further analysis. In this description the spin field constitutes a closed ribbon as shown in Fig. 4.1 (b), so that the computation of number of turns become easier, apparent and accurate as compared to the open belt.

Quite recently, Darboux transformation of the classical HF model has been constructed

<center>(a)   (b)</center>
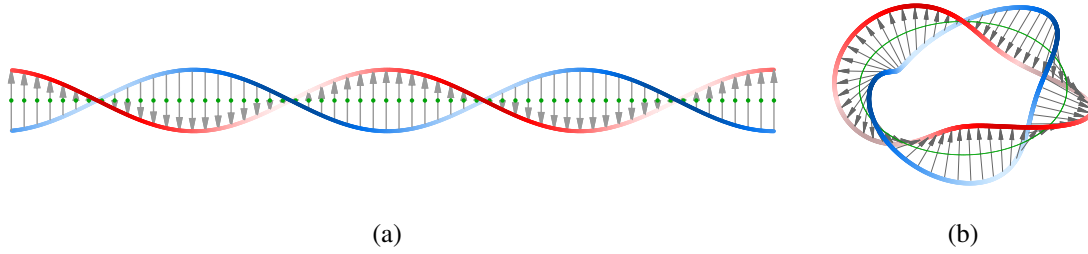
Figure 4.1: Spin configuration $\hat{\mathbf{S}}_{\mathrm{c}}$ (4.11) for $0 < x < L$, where $L = n\pi/\kappa_0$, with $n = 2$.
(a) The locus of the top (bottom) of the spin vector are marked in color red (blue) which
can be viewed as two boundaries of a belt. This open belt has n number of turns. (b) Due to
spatial periodicity, spins at $x = 0$ and $x = L$ are identified, and can be viewed as a closed
belt with n number of turns.

starting with a more general plane wave solution [125, 126], wherein the seed solution
(4.11) arises as a special case. Although breather (rogue) modes were obtained therein,
their investigation was carried out in terms of individual vector components (S_1, S_2, S_3)
and its variations in the time evolution. Moreover, their study is confined in the domain of
classical HF model. On the other hand, a comparative study between classical HF model
and the NLSE, in the context of breather (rogue) excitation has been done recently [127].
In this work, instead of DT technique, the space curve formalism has been employed to
obtain the curvature and torsion associated with NLSE breather solutions. Energy and
momentum of the spin chain are thus obtained and localization properties of the rogue
waves are discussed. In view of the above developments, our study goes beyond this by
exploring the geometrical features of the spin breather.

4.4   Breather modes in classical HF spin chain

Starting with seed solution ψ_{c} (4.6), we arrive at breather solution, say ψ_{cb}, using Darboux
transformation technique detailed in Sec. 2.6. Advantage of the DT technique is that it pro-
vides the corresponding matrix solution to the Lax pair, $\boldsymbol{\Psi}_{\mathrm{cb}}$, along with the breather. We
will first write down an explicit expression for $\boldsymbol{\Psi}_{\mathrm{cb}}$, and then move on to the corresponding
spin breather.

<center>53</center>

4.4.1 Darboux transformation

A detailed steps for the DT technique is provided in Appendix B. In this section we present only the necessary solutions needed for the discussion. The Darboux matrix $\mathbf{P}_1(\lambda)$ can be found in the form $\mathbf{P}_1(\lambda) = \lambda\mathbf{I} + G_0$. We write it explicitly as,

$$\mathbf{P}_1 = \begin{pmatrix} \lambda - \lambda_{0R} & 0 \\ 0 & \lambda - \lambda_{0R} \end{pmatrix} + i\,\frac{\lambda_{0I}}{\Delta} \begin{pmatrix} -\gamma & -e^{2i\kappa_0^2 t}(\alpha - i\,\beta) \\ -e^{-2i\kappa_0^2 t}(\alpha + i\,\beta) & \gamma \end{pmatrix}, \quad (4.13)$$

wherein,

$\alpha = b_1 \cos\omega_{0R} + b_2 \cosh\omega_{0I}$,

$\beta = b_3 \sin\omega_{0R} - b_4 \sinh\omega_{0I}$,

$\gamma = b_4 \sin\omega_{0R} + b_3 \sinh\omega_{0I}$,

$\Delta = b_2 \cos\omega_{0R} + b_1 \cosh\omega_{0I}$

$\omega_0 = \omega_{0R} + i\omega_{0I} = 2p_0(x + 2\lambda_0 t), \quad p_0 = p_{0R} + ip_{0I} = \sqrt{\kappa_0^2 + \lambda_0^2}$,

$b_1 = 2(\lambda_{0I}^2 + p_{0R}^2 - \lambda_{0R}p_{0R} - \lambda_{0I}p_{0I}), \quad b_2 = 2\kappa_0(p_{0I} - \lambda_{0I})$,

$b_3 = -2(\lambda_{0R}^2 + p_{0I}^2 - \lambda_{0R}p_{0R} - \lambda_{0I}p_{0I}), \quad b_4 = 2\kappa_0(p_{0R} - \lambda_{0R})$,

and $\lambda_0 = \lambda_{0R} + i\lambda_{0I}$ is the scattering parameter in the language of IST. Functions $\alpha, \beta, \gamma, \Delta$ and the constants b_i also satisfy conditions,

$$\alpha^2 + \beta^2 + \gamma^2 = \Delta^2,$$
$$b_2^2 + b_3^2 + b_4^2 = b_1^2. \tag{4.14}$$

Darboux transformation gives a new $\mathbf{\Psi}_{cb}$ from old $\mathbf{\Psi}_c$ (4.8) by,

$$\mathbf{\Psi}_{cb}(x, t, \lambda, \lambda_0) = \frac{1}{\sqrt{d_1}}\,\mathbf{P}_1(x, t, \lambda, \lambda_0)\,\mathbf{\Psi}_c(x, t, \lambda), \tag{4.15}$$

where $d_1 = |\mathbf{P}_1| = (\lambda^2 + |\lambda_0|^2 - 2\lambda\lambda_{0R})$. Matrix solution $\mathbf{\Psi}_{cb}$ satisfies the Lax pair

$$\mathbf{\Psi}_{cb,x} = U_{cb}\mathbf{\Psi}_{cb},$$
$$\mathbf{\Psi}_{cb,t} = V_{cb}\mathbf{\Psi}_{cb}, \tag{4.16}$$

where $U_{cb} = U(\psi_{cb})$, and $V_{cb} = V(\psi_{cb})$. One may compare (4.7) and (4.16) to see how DT technique transforms $\mathbf{\Psi}_c$ to $\mathbf{\Psi}_{cb}$ systematically. In the due course, seed solution ψ_c gets updated to ψ_{cb} — a breather solution to the NLSE over the background ψ_c.

4.4.2 Breather solution to the NLSE

As pointed out earlier, breather solution to the NLSE over the seed ψ_c (4.6) is well known in the literature. An explicit analytical expression for this breather solution in its entire generality is given in Ref. [114]. We reproduce the same below for immediate reference:

$$\psi_{cb} = e^{2i\kappa_0^2 t}\Big(\kappa_0 + 2\,\lambda_{0I}\,\frac{(\alpha - i\,\beta)}{\Delta}\Big),$$

(4.17)

where the functions α, β and Δ and the parameters are defined below (4.13). (Details of the derivation is provided in Appendix B)

One of the remarkable case is when $\lambda_{0R} = 0$, wherein a condition $\kappa_0 < \lambda_{0I}$ leads to KMB, and $\kappa_0 > \lambda_{0I}$ leads to AB. A limiting case of both yields PS. We have described these special cases in Appendix B. In what follows, we will examine the spin configuration associated with the NLSE breather ψ_{cb}.

4.4.3 Explicit expression for the spin breather

Spin configuration associated with ψ_{cb} (4.17) can be obtained using the expression,

$$\mathbf{S}_{cb} = \lim_{\lambda \to 0} \mathbf{\Psi}_{cb}{}^{\dagger}\sigma_3 \mathbf{\Psi}_{cb}$$

(4.18)

where $\mathbf{\Psi}_{cb}$ is given in (4.15). Calculation is quite tedious but straight forward. We write explicit expression for the spin field in vector form as,

$$\hat{\mathbf{S}}_{cb}(x,t) = \frac{\lambda_{0R}^2 - \lambda_{0I}^2}{|\lambda_0|^2}\,\hat{\mathbf{S}}_c + \left[\frac{2\,\lambda_{0I}^2}{|\lambda_0|^2\Delta^2}\gamma\beta - \frac{2\lambda_{0I}\lambda_{0R}}{|\lambda_0|^2\Delta}\alpha\right]\hat{\mathbf{i}}$$

$$+ \left[\frac{2\,\lambda_{0I}^2}{|\lambda_0|^2\Delta^2}\,\gamma\,\big(\gamma\,\cos(2\kappa_0 x) - \alpha\sin(2\kappa_0 x)\big) - \frac{2\,\lambda_{0I}\lambda_{0R}}{|\lambda_0|^2\Delta}\,\beta\,\sin(2\kappa_0 x)\right]\hat{\mathbf{j}}$$

$$+ \left[\frac{2\,\lambda_{0I}^2}{|\lambda_0|^2\Delta^2}\,\gamma\,\big(\alpha\,\cos(2\kappa_0 x) + \gamma\sin(2\kappa_0 x)\big) - \frac{2\,\lambda_{0I}\lambda_{0R}}{|\lambda_0|^2\Delta}\,\beta\,\cos(2\kappa_0 x)\right]\hat{\mathbf{k}},$$

(4.19)

where the functions α, β, γ and Δ and the parameters are defined below (4.13), and $\hat{\mathbf{S}}_c$ is given in (4.11) This is a three parameter family of solutions, where κ_0 is a real constant introduced in (4.6), and a complex eigenvalue $\lambda_0(= \lambda_{0R} + i\lambda_{0I})$ is the scattering parameter in the language of IST.

4.4.4 Limiting cases

• When $\lambda_{0I} = 0$, breather ψ_{cb} (4.17) reduces to the seed ψ_{c} (4.6), and spin breather $\hat{\mathbf{S}}_{\mathrm{cb}}$ (4.19) reduces to the seed spin $\hat{\mathbf{S}}_{\mathrm{c}}$ (4.11).

• When $\kappa_0 = 0$, breather ψ_{cb} (4.17) reduces to "secant-hyperbolic" solution ψ_{sh} (4.4), and the spin breather $\hat{\mathbf{S}}_{\mathrm{cb}}$ (4.19) reduces to the corresponding soliton excitation (of the secant hyperbolic type) in the classical HF spin chain [14].

One can verify this by setting $p_0 = -\lambda_0$. This will leads to $\omega_0 = -2\lambda_0(x + 2\lambda_0 t)$. The constants b_i then reduces to,

$$b_2 = b_4 = 0, \quad b_1 = -b_3 = 4|\lambda_0|^2. \tag{4.20}$$

Functions α, β, γ and Δ become,

$$\alpha = b_1 \cos\omega_{0R}, \quad \beta = b_3 \sin\omega_{0R}, \quad \gamma = b_3 \sinh\omega_{0I}, \quad \Delta = b_1 \cosh\omega_{0I}. \tag{4.21}$$

This will readily give,

$$\psi_{\mathrm{cb}}(\kappa_0 = 0) = 2\lambda_{0I}\frac{(\alpha - i\beta)}{\Delta} = 2\lambda_{0I}\frac{(\cos\omega_{0R} + i\sin\omega_{0R})}{\cosh\omega_{0I}} = 2\lambda_{0I}e^{i\omega_{0R}}\operatorname{sech}(\omega_{0I}). \tag{4.22}$$

Corresponding spin configuration can be found to be,

$$\hat{\mathbf{S}}_{\mathrm{cb}}(\kappa_0 = 0) = \left[\frac{2\lambda_{0I}}{|\lambda_0|^2}\operatorname{sech}\omega_{0I}\big(\lambda_{0I}\tanh\omega_{0I}\sin\omega_{0R} - \lambda_{0R}\cos\omega_{0R}\big)\right]\hat{\mathbf{i}}$$
$$+\left[1 - \frac{2\lambda_{0I}^2}{|\lambda_0|^2}\operatorname{sech}^2\omega_{0I}\right]\hat{\mathbf{j}} + \left[\frac{2\lambda_{0I}}{|\lambda_0|^2}\operatorname{sech}\omega_{0I}\big(\lambda_{0I}\tanh\omega_{0I}\cos\omega_{0R} + \lambda_{0R}\sin\omega_{0R}\big)\right]\hat{\mathbf{k}}. \tag{4.23}$$

4.4.5 Spatially periodic breather

The spin field $\hat{\mathbf{S}}_{\mathrm{cb}}$ (4.19) is difficult to analyse in its entire generality. However, it does have all the attributes of a breather, which make it relatively simple in certain limits. In fact, the real part of the spectral parameter, here labelled λ_{0R}, is responsible for the velocity of the breather. This will be set to zero in the following discussion without losing any of the qualitative features. For our further analysis, we shall consider a purely imaginary complex parameter,

$$\lambda_0 = 0 + i\,\lambda_{0I} = i\,a, \tag{4.24}$$

where a is positive. Then, the spin field in (4.19) reduces to a simpler form:

$$\hat{\mathbf{S}}_{\text{cb}} = -\hat{\mathbf{S}}_{\text{c}} + \frac{2\gamma}{\Delta^2}\left[\beta\hat{\mathbf{i}} + \left(\gamma\cos(2\kappa_0 x) - \alpha\sin(2\kappa_0 x)\right)\hat{\mathbf{j}} + \left(\alpha\cos(2\kappa_0 x) + \gamma\sin(2\kappa_0 x)\right)\hat{\mathbf{k}}\right]$$
(4.25)

Here, $\hat{\mathbf{S}}_{\text{c}}$ is the seed solution given in (4.11), and α, β, γ and Δ were defined below (4.13). Now we have two distinct cases, i) $\kappa_0 < a$ and ii) $\kappa_0 > a$. Besides these two cases there is one more interesting case — the *rogue* behaviour, when $a \sim \kappa_0$, that will be discussed in detail in the next section.

Beforehand, it is to be noted that the functions α, β, γ and Δ are depending on x and t through ω_0. Hence, we write its real and imaginary parts explicitly as,

$$\begin{aligned} \omega_{0R} &= 2p_{0R}\,x + 4t(p_{0R}\,\lambda_{0R} - p_{0I}\,\lambda_{0I}), \\ \omega_{0I} &= 2p_{0I}\,x + 4t(p_{0R}\,\lambda_{0I} + p_{0I}\,\lambda_{0R}). \end{aligned}$$
(4.26)

• **Case (i)** — $\kappa_0 < a$: From the expressions given below (4.13), $p_0 = \sqrt{\kappa_0^2 - a^2}$ is purely imaginary. Thus ω_{0R} is a pure function of time, while ω_{0I} is a function only of x. In short, $\omega_{0R} = \omega_{0R}(t)$ and $\omega_{0I} = \omega_{0I}(x)$. Periodicity in α, β, γ and Δ arises from ω_{0R}, whereas the localization comes from ω_{0I}. Thus the spin field is localized in space, and periodic in time, with a period

$$T = \frac{\pi}{2a\sqrt{a^2 - \kappa_0^2}}.$$
(4.27)

Since we are looking for a spin chain with periodic boundary condition to have finite total energy, this case is disallowed.

• **Case (ii)** — $\kappa_0 > a$: Here, we have $p_0 = \sqrt{\kappa_0^2 - a^2}$, which is purely real. The variables defined below (4.13) reduce to the following:

$$\begin{aligned} \alpha &= 2\kappa_0^2\cos\omega_{0R} - 2\kappa_0 a\cosh\omega_{0I}, \\ \beta &= -2\kappa_0\sqrt{\kappa_0^2 - a^2}\sinh\omega_{0I}, \\ \gamma &= 2\kappa_0\sqrt{\kappa_0^2 - a^2}\sin\omega_{0R}, \\ \Delta &= -2\kappa_0 a\cos\omega_{0R} + 2\kappa_0^2\cosh\omega_{0I}, \\ \omega_0 &= \omega_{0R} + i\omega_{0I} = 2\sqrt{\kappa_0^2 - a^2}(x + 2iat). \end{aligned}$$
(4.28)

In contrast to case (i), the breather is now periodic in space due to $\omega_{0R} = \omega_{0R}(x)$, and localized in time as $\omega_{0I} = \omega_{0I}(t)$. Spatially, the field is composed of two periodic functions

57

with periods generally incommensurate,

$$L_1 = \frac{\pi}{\kappa_0}, \quad \text{and} \quad L_2 = \frac{\pi}{\sqrt{\kappa_0^2 - a^2}} = \rho L_1, \quad (4.29)$$

where $\rho = 1/\sqrt{1 - a^2/\kappa_0^2}$. From (4.28), it can be verified that at $a = \kappa_0$, the spin field get reduced to the background seed field that we started with. Situation is same at $a = 0$ as discussed in Sec. 4.4.4. So we are left with strict case $0 < a < \kappa_0$. In order to satisfy our condition for periodicity, $\hat{\mathbf{S}}_{cb}(x + L, t) = \hat{\mathbf{S}}_{cb}(x, t)$, the spatial periods given in (4.29) should be in such a way that,

$$L = nL_1 = mL_2 \quad (4.30)$$

where m and n are positive integers. Thus, from (4.29), $\rho = L_2/L_1 = n/m$, or equivalently $a = \frac{\pi}{L}\sqrt{n^2 - m^2}$. Note that $n > m$ since $\rho \in (1, \infty)$.

In the language of NLSE, case (i) corresponds to time periodic Kuznetsov-Ma Breather (KMB) whereas case (ii) is associated with the spatially periodic Akhmediev Breather (AB) (refer Appendix B for details). The *rogue* breather mode arises as an intermediate limiting case, when both the periods tend to infinity. The rogue wave is highly localized in space and time. The field variable suddenly gets enhanced locally in space, and is sustained only for a short duration. From (4.27) and (4.29), it can be seen that a rogue corresponds to the case when $|\kappa_0^2 - a^2| \sim 0$, or equally $\rho \to \infty$. However, in our finite system of size L with periodic boundary conditions, the nearest possible one is when $\rho = n/m$ is largest, i.e., when $m = 1$ for any given n. Consequently, we shall identify this as the *rogue spin mode* in the finite ferromagnetic spin chain. As a further justification for the rogue behaviour, we show in Fig. 4.2, a sudden colossal rise in the energy density profile, localized in both space and time, commonly ascribed to rogue waves.
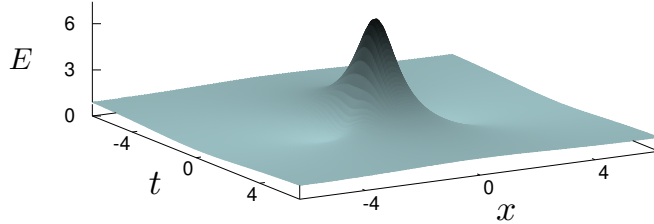
Figure 4.2: The energy density $E(x, t) = (\hat{\mathbf{S}}_x)^2$ in the $x - t$ plane for $m = 1$, $n = 2$ and $\kappa_0 = 0.5$ ($L = 2\pi/\kappa_0$ and $a = \sqrt{3}\pi/L$) — rogue spin mode, for $\hat{\mathbf{S}}_{cb}$ (4.25). A short-lived intensification of energy local in both space and time accredited to rogue waves.

4.5 The rogue mode and the 'belt trick'

In the previous section we have discussed a class of spatially periodic spin breathers for $\kappa_0 > a$, with periods L_1 and L_2 as given in (4.29). Further we identified a rogue event particularly for the finite spin chain with periodic boundary condition. In a finite spin chain of size $L(= nL_1 = mL_2)$, rogue occurs with largest possible $\rho(= n/m, n > m)$. As discussed earlier, the breather vanishes for $a = 0$ and $a = \kappa_0$, or in terms of ρ, there is no breather for $\rho = 1$ and $\rho = \infty$. For this reason $m = n$ and $m = 0$ are overruled. Therefore we take $m = 1$ as the rogue situation in finite spin chain, for any $n = 2, 3, ..$ etc. We set $n = 2$ in this study, as this is the one with lowest total energy in this class (Eq. (4.12)). We also set $\kappa_0 = 0.5$ in this study without loss of generality. For instance see Fig. 4.2, with background energy density $4\kappa_0^2 = 1$, from (4.3). The length of the chain is $L = n\pi/\kappa_0 = 4\pi$. We have chosen $-L/2 < x < L/2$, in order to place the rogue excitation at the origin of the $x - t$ plane.

The above mentioned rogue wave is valid only in finite spin chain. Essentially we are dealing with a spatially periodic breather (Akhmediev type) in HF model, but looking at a repeating segment of length $L = n\pi/\kappa_0$. In this segment the dynamics appears as a rogue event with a single energy peak as shown in Fig. 4.2. However, for a true rogue event one can think of an infinite spin chain with $|\kappa_0^2 - a^2| \sim 0$.

We have shown the seed spin with $n = 2$ in Fig. 4.1 which will act as the background field, over which the rogue excitation occurs. There, for the sake of illustration we have used red (blue) lines to indicate the locus of the top (bottom) of the spin vector. The two lines can be viewed as the two boundaries of (an open) belt surface. Due to the spatial periodicity spins at $x = 0$ and $x = L$ are identical, allowing us to make the belt a closed one with n number of turns. In what follows, we will study the dynamics of spin chain in terms of the topological feature — net turns, present in this belt.

4.5.1 Open belt and the number of turns

We show the complete time evolution of rogue spin mode $\hat{\mathbf{S}}_{\mathrm{cb}}$ (4.25) in Fig. 4.3. As expected, the dynamics begins from a smooth periodic background as $t \to -\infty$ and eventually recover the same initial condition as $t \to +\infty$. One can think of an open belt made up of series of spin vectors from one end to the other. The initial and final state of the belt has two complete turns between its ends, since $n = 2$. In the rogue excitation, there is an intermediate phase where the net turns present in the belt becomes zero. This is
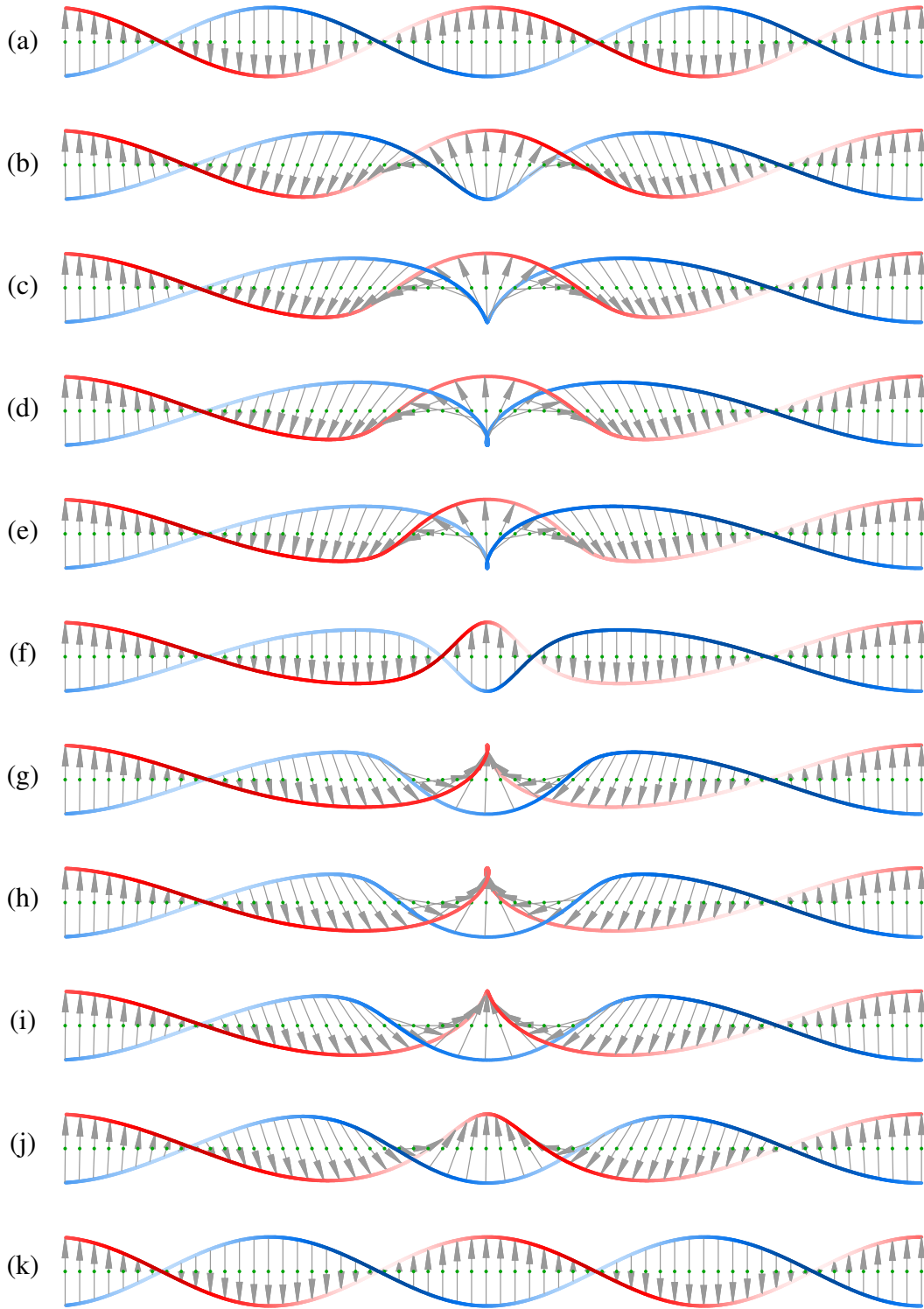
Figure 4.3: Rogue wave in classical HF spin chain. Time evolution of the spin configuration $\hat{\mathbf{S}}_{cb}$ (4.25) for $n = 2$ and $m = 1$. (a) and (k) corresponds to the background spin field at $t \to \pm\infty$, where the net number of turn is two. (f) corresponds to an instant $t = 0$, where the energy peak has its maximum, with net turns in the spin chain is surprisingly zero. For detailed animation, see the supplementary material: belt_trick1.avi .

quite dramatic because each spin vectors evolve continuously in time, rotated only by an infinitesimal amount from its neighbour. However the overall behaviour of the spin chain shows a singular shift form 'two total turns' to 'no net turn'. Another interesting fact is that in Fig. 4.3 (a) and (k), all the spin vectors are lying in a plane, more precisely $y - z$ plane (refer $\hat{\mathbf{S}}_{\mathrm{c}}$ (4.11)). If one moves along the chain from one end to the other, i.e., along the x axis, the spin field rotates two times in this plane amounting to a total 'twist' of '2'. However, in the intermediate stage through its evolution, Fig. 4.3 (f), the total twist about the axis is 'zero'.

We further observe that Fig. 4.3 (f) corresponds to an instant $t = 0$, where the energy density peak has its maximum, as shown in Fig. 4.2. Therefore we draw a conclusion that the transformation from 'two total turns' to 'no net turn' is accompanied by the rogue excitation.

Considering the choice of parameter values, spatially periodic spin breather studied here is essentially an analogue of the well known Akhmediev breather. A remarkable feature of this breather solution is that, it grows from a uniform background and eventually returns to the same through a rather complicated nonlinear evolution. Akhmediev breather seen in their Fourier spectrum is an exact solution to the celebrated FPUT recurrence phenomena [10]. In our classical HF model, what is narrated in Fig. 4.3 is a recurrence process. Following the breather excitation, the spin chain recovers the initial state exactly as in the beginning. Any trace of the breather excitation thus occurred in the spin chain is not visible in the long run. We will revisit this issue in detail later in Chapter 5.

4.5.2   Closed belt and the linking number

In order to have a quantitative description one need to compute the number of turns present in the belt. A closed belt description is more suitable for this analysis. In Fig. 4.4, we show the time evolution of the closed belt for the rogue spin mode $\hat{\mathbf{S}}_{\mathrm{cb}}$ (4.25) through six sequential instances. The initial and final state nearly reaches the background field as seen in Fig. 4.4 (a) and (f) with '2' complete turns. Interesting case is when t approaches zero — the rogue event, accompanied with the energy peak as seen in Fig. 4.2. This 'rogue event' corresponds to Fig. 4.4 (c) and (d) where the total number of turns in the belt is surprisingly zero. One may think of a transition stage between these two as shown in Fig. 4.4 (b) and (e), wherein the belt passes through itself.

Alternatively, this can also be described in terms of linking number, L_k, of the red and blue loops seen in Fig. 4.4. Linking number of two loops may be broadly thought of as
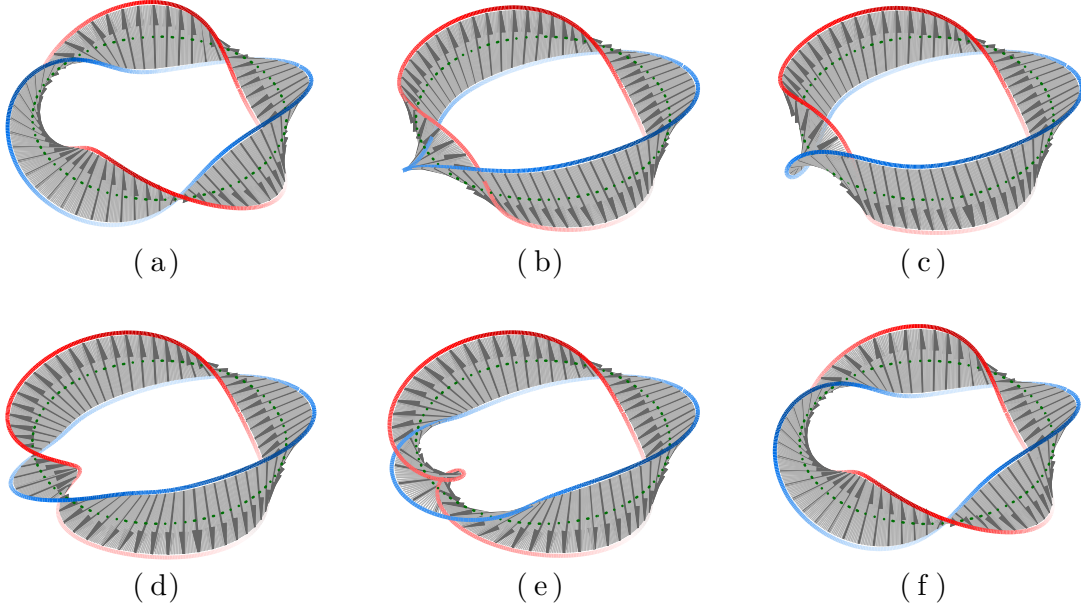
Figure 4.4: Spin configuration at different instances from the time evolution of $\hat{\mathbf{S}}_{cb}$ (4.25) for $n = 2$ and $m = 1$. Owing to the spatial periodicity, spins at the boundary are identified, making the lattice a circle, resulting in a closed belt made up of spin vectors. The loci of the top (bottom) ends of the spin vectors are marked by the red (blue) lines. The belt has '2' net rotations (or 4π radians) in figures (a) and (f). Whereas the net rotation in (c) and (d), is zero. In other words, the blue and red loops are *linked* in (a) and (f) with a linking number '2', while in the intermediate phase, (c) and (d), they are *un-linked*. In the transition process, the belt passes through itself as shown in (b) and (e). For detailed animation, see the supplementary material: belt_trick2.avi .

the number of times the loops have to cut through each other to be completely separated. Before and after the rogue event these loops are linked with, $L_k = 2$, whereas in the intermediate phase they are un-linked, i.e., the loops can be separated without breaking them. Gauss' linking number [128] of two closed curves $\mathbf{R}_1(s)$ and $\mathbf{R}_2(s')$ is given by

$$L_k = \frac{1}{4\pi} \oint_{\mathbf{R}_1} \oint_{\mathbf{R}_2} \mathbf{T}_1(s) \times \mathbf{T}_2(s') \cdot \frac{\mathbf{R}_1(s) - \mathbf{R}_2(s')}{|\mathbf{R}_1(s) - \mathbf{R}_2(s')|^3} \, ds \, ds', \tag{4.31}$$
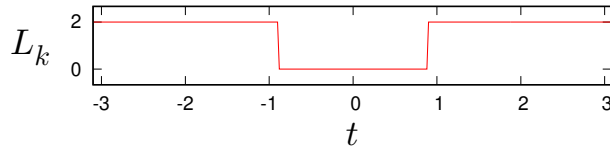
Figure 4.5: A plot of the linking number L_k between the red and blue loops shown in Fig. 4.4, as a function of time. The behaviour of the total twist is identical, since $L_k = T_w$.

62

where $T_1(s)$ and $T_2(s')$ are the respective tangent vectors. Linking number L_k of two loops is necessarily an integer, invariant under continuous deformation that do not tear the loops. Hence it is a topological quantity [129]. One can think of two curves R and R' that closely track each other, and form the boundaries of a closed ribbon such that,

$$R'(s) = R(s) + \epsilon\, U(s), \tag{4.32}$$

where ϵ is the width of the ribbon, and $U(s)$ is a local vector lying along the surface of the ribbon perpendicular to the tangent vector at s, i.e., $T(s) \cdot U(s) = 0$. But as $\epsilon \to 0$ both the integrals in L_k (4.31) go along the same curve R, giving rise to a limiting integral W_r, as written below [130].

$$W_r = \frac{1}{4\pi} \oint_R \oint_R T(s) \times T(s') \cdot \frac{R(s) - R(s')}{|R(s) - R(s')|^3}\, ds\, ds'. \tag{4.33}$$

The writhe W_r depends only on the orientation of the axis curve. It is not an invariant under continuous deformation of the curve [129]. Along the ribbon, vector U rotates about T. Summing all the local variations of $U(s)$ gives a measure of the twist, explicitly written as [130],

$$T_w = \frac{1}{4\pi} \oint_R T(s) \cdot \left(U(s) \times \frac{dU(s)}{ds} \right) ds. \tag{4.34}$$

Twist T_w is not an invariant under deformation. The quantity dT_w/ds measures the rotation rate of secondary curve about the axis curve [130]. The non-topological properties twist T_w, and writhe W_r, satisfy the Calugareanu theorem [131], also popular as White-Fuller theorem [132, 133],

$$L_k = T_w + W_r . \tag{4.35}$$

The axis of the belt (ribbon) considered here (Fig. 4.4) lies on a circle, resulting in $W_r = 0$ [129], and therefore $L_k = T_w$. In this case the twist T_w measures the amount by which the boundaries are twisted about the center axis (middle line). If the ribbon passes through itself (which is actually happening in our case), L_k changes by ± 2, see for instance [134, Sec. 4]. We compute the linking number numerically, using Gauss' linking integral (4.31), and presented in Fig. 4.5 as a function of time.

A sudden jump in L_k (or T_w) from $2 \to 0$ and $0 \to 2$ occurs when the red and blue loops make a crossover. In other words, a portion of the belt passes through itself which is not forbidden here, as the belt is imaginary, but spin are not. The spins live in their

63

internal space, and their dynamics is quite smooth and continuous. Each spin vector differs in its orientation from its neighbours only slightly, but their collective dynamics exhibit a transition between two distinct phases, which is not obvious. We set other integer values for m and n, and observed the same qualitative behaviour. In general, the change in number of turn is given by, $n \to (n - 2m) \to n$.

4.5.3   Contractible loop in $\mathrm{SO}(3)$ group manifold

At each lattice site, one may construct a triad of vectors (Fig. 2.1), with the spin vector itself being one of them. The triad at the adjacent site may be obtained from the first through the action of an $\mathrm{SO}(3)$ group element — more precisely, a rotation matrix. Since the spins at the boundary are identified, the entire chain is thus described by a set of $\mathrm{SO}(3)$ elements, that forms a closed loop in the parameter space of $\mathrm{SO}(3)$ group. Before we proceed further with our analysis, we describe here the $\mathrm{SO}(3)$ group manifold and its properties.

Rotation matrix $R \in \mathrm{SO}(3)$, is a 3×3 real matrix, such that $R^{-1} = R^T$ and $\det R = 1$. It has three independent parameters in its nine entries. In order to express the matrix R, one choice is Euler angles [51, p. 150], but they are not quite useful for practical purposes. A more convenient approach is the axis-angle representation in which a rotation is specified by certain angle θ, about an axis $\hat{\mathbf{n}}$. Let J_1, J_2 and J_3 be the traceless Hermitian matrices, the generators of rotation, given by,

$$J_1 = \begin{pmatrix} 0 & 0 & 0 \\ 0 & 0 & -i \\ 0 & i & 0 \end{pmatrix}, \quad J_2 = \begin{pmatrix} 0 & 0 & i \\ 0 & 0 & 0 \\ -i & 0 & 0 \end{pmatrix}, \text{ and } \quad J_3 = \begin{pmatrix} 0 & -i & 0 \\ i & 0 & 0 \\ 0 & 0 & 0 \end{pmatrix}. \tag{4.36}$$

An arbitrary rotation about $\hat{\mathbf{n}}$ through an angle θ, can be expressed in the form [135, p. 32],

$$R(\hat{\mathbf{n}}, \theta) = e^{-i\theta(\hat{\mathbf{n}} \cdot \mathbf{J})}, \tag{4.37}$$

where $\hat{\mathbf{n}} = \{n_1, n_2, n_3\}$ and $\mathbf{J} = \{J_1, J_2, J_3\}$. Note that, $|\hat{\mathbf{n}}| = 1$, hence only 2 parameters are needed to specify $\hat{\mathbf{n}}$. For convenience, let $\mathcal{J} = -i(\hat{\mathbf{n}} \cdot \mathbf{J})$. From (4.36), it follows that,

$$\mathcal{J} = -i(\hat{\mathbf{n}} \cdot \mathbf{J}) = \begin{pmatrix} 0 & -n_3 & n_2 \\ n_3 & 0 & -n_1 \\ -n_2 & n_1 & 0 \end{pmatrix}, \quad \mathcal{J}^3 = -\mathcal{J}. \tag{4.38}$$

The matrix exponential $\exp\{\theta\mathcal{J}\}$ can be obtained by the series expansion [136, 137] as

follows:

$$
\begin{aligned}
e^{\theta \mathcal{J}} &= \mathbf{I} + \theta \mathcal{J} + \frac{1}{2!}\theta^2 \mathcal{J}^2 + \frac{1}{3!}\theta^3 \mathcal{J}^3 + \frac{1}{4!}\theta^4 \mathcal{J}^4 + \cdots \\
&= \mathbf{I} + \theta \mathcal{J} + \frac{1}{2!}\theta^2 \mathcal{J}^2 - \frac{1}{3!}\theta^3 \mathcal{J} - \frac{1}{4!}\theta^4 \mathcal{J}^2 + \cdots \\
&= \mathbf{I} + \mathcal{J}\left(\theta - \frac{1}{3!}\theta^3 + \cdots\right) + \mathcal{J}^2\left(\frac{1}{2!}\theta^2 - \frac{1}{4!}\theta^4 + \cdots\right) \\
&= \mathbf{I} + \mathcal{J}\left(\sin\theta\right) + \mathcal{J}^2\left(1 - \cos\theta\right).
\end{aligned}
\tag{4.39}
$$

Finally, one can arrive at the well known expression for rotation matrix,

$$
R(\hat{\mathbf{n}}, \theta) = e^{-i\theta(\hat{\mathbf{n}} \cdot \mathbf{J})} = \mathbf{I} + \sin\theta\,(-i\hat{\mathbf{n}} \cdot \mathbf{J}) + (1 - \cos\theta)\,(-i\hat{\mathbf{n}} \cdot \mathbf{J})^2.
\tag{4.40}
$$

Each element of $\mathrm{SO}(3)$ group can be written in the form $e^{-i\theta(\hat{\mathbf{n}} \cdot \mathbf{J})}$, where θ is real. Linear vector space $\hat{\mathbf{n}} \cdot \mathbf{J}$ is an *algebra* spanned by a basis J_1, J_2 and J_3 endowed with a commutation relation,

$$
[J_i, J_j] = i\epsilon_{ijk} J_k,
\tag{4.41}
$$

where ϵ_{ijk} is the Levi-Civita tensor [135]. Since this algebra generates the Lie group $\mathrm{SO}(3)$, the vector space spanned by $\{J_1, J_2, J_3\}$ is called the $\mathfrak{so}(3)$ Lie algebra. The relation (4.37) can be seen as an exponential map which has vital role in the study of Lie algebra and Lie groups. By definition [138, 137], the above Lie group and its Lie algebra are related by:

$$
\exp : \mathfrak{so}(3) \longrightarrow \mathrm{SO}(3).
\tag{4.42}
$$

The number of real parameters needed to specify a group element is its dimension, which is 3 for $\mathrm{SO}(3)$ Lie group. Corresponding Lie algebra $\mathfrak{so}(3)$ has a basis $\{J_1, J_2, J_3\}$ with the same number of elements.

As mentioned above, $R(\hat{\mathbf{n}}, \theta)$ defines a rotation about the vector $\hat{\mathbf{n}}$ through an angle θ. When θ goes beyond π, one can see from (4.40) that,

$$
R(\hat{\mathbf{n}}, \pi + \theta) = R(-\hat{\mathbf{n}}, \pi - \theta).
\tag{4.43}
$$

Thus, beyond π one can conveniently express the rotation through an angle $\pi - \theta$ about an axis $-\hat{\mathbf{n}}$. This effectively fixes the range of θ as, $0 < \theta < \pi$. Another remarkable conclusion follows from (4.40) by setting $\theta = \pi$:

$$
R(\hat{\mathbf{n}}, \pi) = R(-\hat{\mathbf{n}}, \pi).
\tag{4.44}
$$

Equations (4.43) and (4.44) can be more meaningful if we consider an open sphere of radius π, as shown in Fig. 4.6. Every point in this sphere is represented by a position vector $\vec{\mathcal{P}} = \theta\hat{\mathbf{n}}$, i.e., at a radial distance θ, in the direction $\hat{\mathbf{n}}$. Every point thus describe a rotation through $\vec{\mathcal{P}} = \theta\hat{\mathbf{n}} \equiv R(\hat{\mathbf{n}}, \theta)$. See Fig. 4.6(a) for a pictorial representation. When $\theta = \pi$, the rotation is represented equally by two points due to the relation (4.44). These two points — antipodal points (or pairs), resides at the boundary of the sphere but diametrically opposite to each other. Since the purpose is to represent the rotation, antipodal points are hence identified. This is shown in Fig. 4.6(b). An open sphere of radius π, with antipodal points identified in this manner, is referred as the parameter space of $SO(3)$ group. This sphere is closed and bounded. In what follows, we will explain two kinds of closed loops in this parameter space where one is contractible but the other is not [139, p. 96].

$R(\hat{\mathbf{n}}, \theta)$

$R(\hat{\mathbf{n}}, \pi) = R(-\hat{\mathbf{n}}, \pi)$

(a)   (b)
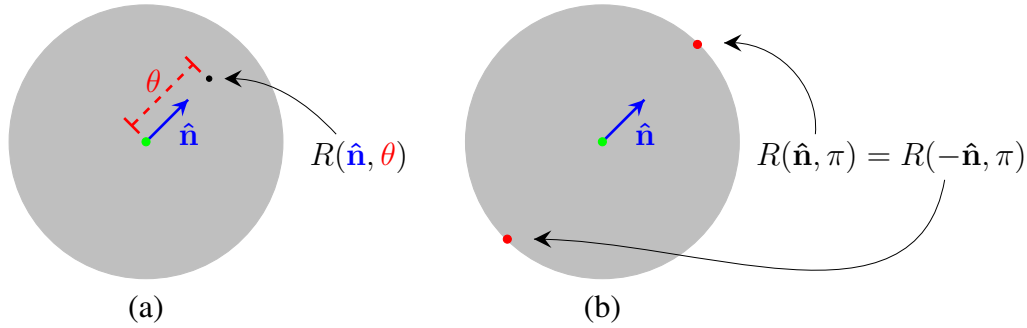
Figure 4.6: Parameter space of $SO(3)$. (a) An open sphere of radius π. Any arbitrary rotation $R(\hat{\mathbf{n}}, \theta)$ can be indicated by a point $\vec{\mathcal{P}}(= \theta\hat{\mathbf{n}})$ in this sphere at a radial distance θ, in the direction $\hat{\mathbf{n}}$. Rotation beyond π can be represented using $R(\hat{\mathbf{n}}, \pi+\theta) = R(-\hat{\mathbf{n}}, \pi-\theta)$. (b) Antipodal points (for e.g. red dots) are identified since they represent the same rotation.

For the sake of simplicity, consider a full rotation of an object or a triad in a plane. Obviously, the the rotation is about a fixed vector $\hat{\mathbf{n}}$ which is the normal to the plane, and the angle of rotation varies from 0 to 2π. One can visualize this rotation by marking the points $\vec{\mathcal{P}} = \theta\hat{\mathbf{n}}$, in the parameter space corresponding to each orientation the triad takes in the due course. This is shown in Fig. 4.7. Initial orientation indicated by $\theta = 0$, corresponds to the center of the sphere, which is the identity element in the parameter space. As θ varies to $\pi/2$, the point representing the rotation $\vec{\mathcal{P}}$ moves in the direction $\hat{\mathbf{n}}$, thereby making a line as shown in (b). When $\theta = \pi$, the point $\vec{\mathcal{P}}$ touches the boundary (at the top), which is equally represented by a point on the opposite pole (at the bottom). These are antipodal points marked in color red in the figure. Beyond π the curve continues from the antipodal point at the bottom towards the center satisfying (4.43). After a complete rotation; $\theta = 2\pi$, which gives $R(\hat{\mathbf{n}}, 2\pi) = R(\hat{\mathbf{n}}, 0) = \mathbf{I}$.

Thus $\vec{\mathcal{P}}$ comes back to the center of the sphere, thereby making a closed loop in the parameter space. It is to be noted that, the curve seen in Fig. 4.7(e) doesn't have any discontinuity at the antipodal points. Visually it may seem as broken when it touches the red dots (antipodal points), but in the mathematical sense the curve is smooth and closed. Although the description start with a rotation in a plane, the conclusion to be drawn from this closed loop is more general.

A closed loop in the parameter space of $\mathrm{SO}(3)$ describes a rotation in Euclidean 3-space keeping the initial and final orientation fixed. Any continuous deformation of this closed loop are therefore valid. However, there exist a constraint that the corresponding antipodal points (pairs) in the parameter space are always at the opposite poles. This constraint is illustrated in Fig. 4.8. So, one cannot merge two antipodal points together. On the other hand, antipodal points cannot be detached from the boundary as it will make the loop discontinuous. Whatever be the deformation, the closed loop formed by one complete rotation cannot be shrunk to a point [139, p. 96]. In short, one full rotation by 2π is topologically non-trivial [140].

In the parameter space two complete rotations can be seen as two diametrical lines as shown in Fig. 4.9(a). Antipodal points of the same kind are marked in same color. Note that, each diametrical line connects two antipodal points which are of different kind. This is in clear contrast to that of one rotation scenario. Therefore, the constraint illustrated in Fig. 4.8 for one rotation, is not applicable here. Closed curve thus can be shrunk to a point as shown in Fig. 4.9(b)–(e). In conclusion, a closed loop in the parameter space corresponding to two complete rotation is contractible [139, p. 96]. I.e., a rotation through 4π is topologically trivial [140].

In the above discussion we set the initial orientation as identity $\mathbf{I}$, which is why all the curves passes through the center of the sphere. Such a description was only to make the concept clear, and it is not a necessity. Rotation of an object (rotating frame) is analysed with respect to a fixed frame of reference (non-rotating frame). After the rotation, if the object comes back to the same orientation, it must draw a closed curve in the parameter space of $\mathrm{SO}(3)$. Identity (center of the sphere) has no special role in this curve. If the closed curve passes through antipodal points odd number of times, they cannot be shrunk to a point [139, p. 97]. On the other hand, if it passes through antipodal points even number of times, they can be shrunk to a point. A Lie group $\mathcal{G}$ is *simply connected* if every loop can be continuously shrunk to a point in $\mathcal{G}$ [138, p. 15]. Therefore, $\mathrm{SO}(3)$ is not simply connected. In fact $\mathrm{SO}(3)$ is *doubly connected* because it allows two distinct classes of closed curves [139, p. 96].

(a) $\theta = 0$ (b) $\theta = \pi/2$ (c) $\theta = \pi$ (d) $\theta = 3\pi/2$ (e) $\theta = 2\pi$
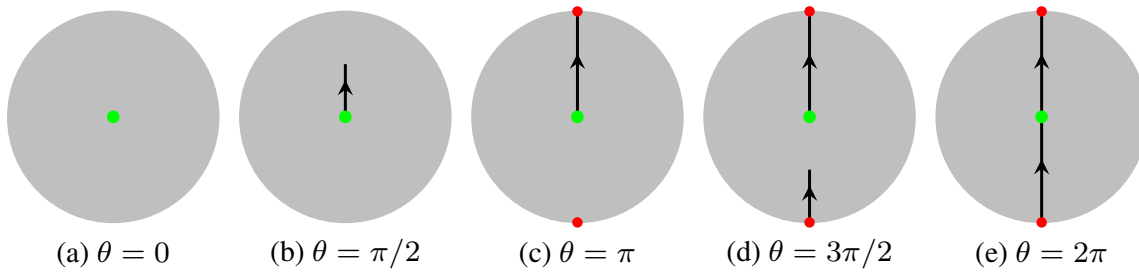
Figure 4.7: One complete rotation seen in the $SO(3)$ group manifold. Rotation about an axis $\hat{\mathbf{n}}$ through an angle θ is marked by a point $\vec{\mathcal{P}} = \theta\hat{\mathbf{n}}$ in an open sphere of radius π, with antipodal points identified. A complete rotation in a plane ($\theta : 0 \to 2\pi$) forms a closed loop in the parameter space.

(a)   (b)
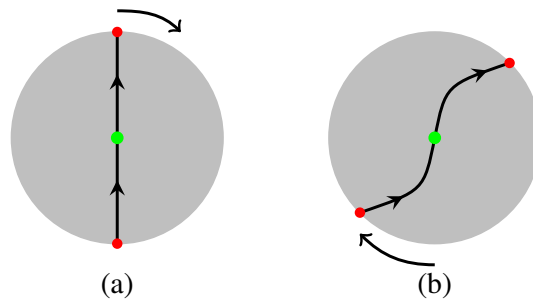
Figure 4.8: Non contractible loop in the parameter space of $SO(3)$. (a) Closed loop in the form of a diametrical line corresponds to one complete rotation. Antipodal points (red dots) are always pinned together so that they situate at the opposite poles. (b) Any deformation in this closed loop can no way shrink it to a point. One rotation is non-trivial.

(a)   (b)   (c)   (d)   (e)
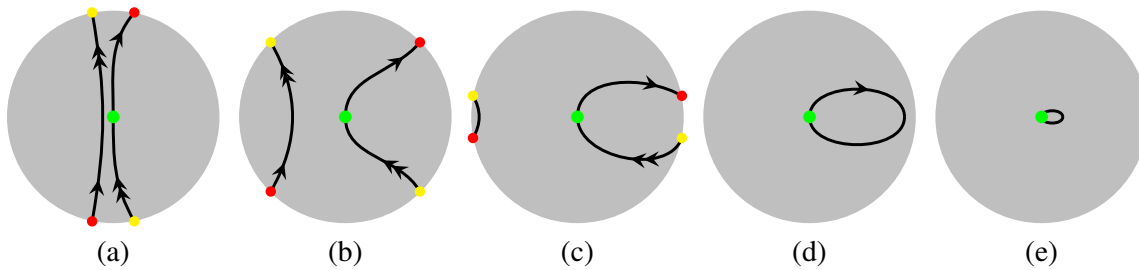
Figure 4.9: Contractible loop in the parameter space of $SO(3)$. (a) Two complete rotations form a closed loop in the parameter space, which can be seen as two diametrical lines connecting antipodal points. Antipodal points of the same kind are marked in same color — red and yellow. (b) - (e) Deformation in this closed loop can eventually shrink it to a point. Two rotation is trivial.

68

Due to the doubly connected nature of $\mathrm{SO}(3)$ group, a 'single turn' cannot be removed (added) from (to) a belt, keeping the orientation of its ends fixed. At the same time, it is possible to remove two complete turns from a belt through a continuous deformation (keeping its end orientation fixed). This is often referred to as 'belt trick', 'Dirac's string trick', 'plate trick', etc [141, 140]. This is a simple demonstration using a belt or a ribbon to explain that 'two rotation' is in fact 'no rotation'.

Now coming back to the spin chain, we note that the spins at the boundary are identified. Thus the entire chain is described by a set of $\mathrm{SO}(3)$ elements, that forms a closed loop in the parameter space of $\mathrm{SO}(3)$. At the occurrence of rogue breather we observed a continuous transition from 'two total turns' to 'no net turn'. This can be viewed as the shrinking of two diametrical lines in the parameter space (corresponds to 4π rotation) to a point (in fact not a point, but a closed loop perfectly inside the sphere). Therefore we conclude that, the rogue breather in classical Heisenberg ferromagnetic spin chain is a manifestation of the belt trick, arising naturally in its dynamics. We are not aware of any other physical system, or event that exhibit the belt trick through their natural dynamics.

4.6 Indicatrix curve and constant area

Since $\hat{\mathbf{S}}$ is a unit vector it can be expressed in the form $\hat{\mathbf{S}} = (\sin\theta\cos\phi, \sin\theta\sin\phi, \cos\theta)$ where θ and ϕ are spherical polar co-ordinates. Each spin vector thus can be represented by a point on the surface of a unit sphere. The entire spin chain at any particular instant of time, traces a curve on the unit sphere which is called indicatrix. Due to spatial periodicity of the spin field this indicatrix must be a closed curve. We show in Fig. 4.10, a sequence of indicatrix curves taken from the time evolution of the rogue breather.

We below obtain the area of the surface enclosed by the closed indicatrix, denoted by $\mathbf{F}_I$. This is clearly equal to the flux through this enclosed area due to a magnetic monopole of unit strength situated at the origin. I.e., a magnetic field that is radially outward, and has unit magnitude at the surface. This is given by

$$\mathbf{F}_I = \int da = \int_{\text{area enlosed by indicatrix}} \mathbf{B} \cdot \vec{da} = \oint_{\text{closed indicatrix}} \mathbf{A} \cdot \vec{dl}. \qquad (4.45)$$

Here, we have invoked Stokes' theorem for the closed loop traced by $\hat{\mathbf{S}}$ on the surface of the unit sphere, and $\mathbf{A}$ is the vector potential, such that $\nabla \times \mathbf{A} = \mathbf{B}$. The magnetic field of a monopole of unit strength, $\mathbf{B} = \hat{\mathbf{r}}/r^2$ can be derived from a vector potential [142, p. 140]

69

$$\mathbf{A} = \frac{(\pm 1 - \cos\theta)}{r\sin\theta}\hat{\phi}, \tag{4.46}$$

with the '$\pm$' applicable in upper and lower hemispheres, respectively, both nevertheless leading to the same $\mathbf{B}$. More precisely, there are two vector potentials $\mathbf{A}^{\mathrm{I}}$ and $\mathbf{A}^{\mathrm{II}}$ where the former with '$+1$' is singular only at $\theta = \pi$ and the later with '-1' is singular at $\theta = 0$. A line element in spherical polar co-ordinate is given by $\vec{dl} = dr\,\hat{\mathbf{r}} + r\,d\theta\,\hat{\boldsymbol{\theta}} + r\sin\theta\,d\phi\,\hat{\boldsymbol{\phi}}$. Substituting $\mathbf{A}^{\mathrm{I}}$ in (4.45), we get the integrand as $(1 - \cos\theta)d\phi$. Angles θ and ϕ are parametrized by x. Hence we express the area enclosed by the indicatrix curve as

$$\mathbf{F}_I = \oint \frac{\partial\phi}{\partial x}(1 - \cos\theta)dx. \tag{4.47}$$

This integral is in fact also the total momentum of the spin chain, and is the generator for spatial translations [35]. Since a uniform lateral shift of the spin mode does not change its total energy, the total momentum commutes with the Hamiltonian

$$\mathbf{H} = J \int \left(\frac{\partial\hat{\mathbf{S}}}{\partial x}\right)^2 dx, \tag{4.48}$$

and hence remains a constant. With $m = 1$ and $n = 2$ for the rogue spin mode, using (4.25) a direct calculation of the integral in (4.47) yields $\mathbf{F}_I = 4\pi$. In Fig. 4.10 we illustrate the time evolution of the indicatrix curve for the rogue breather mode. The curve intersects itself once. With the intersection preserved, the area enclosed by the indicatrix on the surface of the unit sphere remains constant.

(a)   (b)   (c)   (d)   (e)   (f)
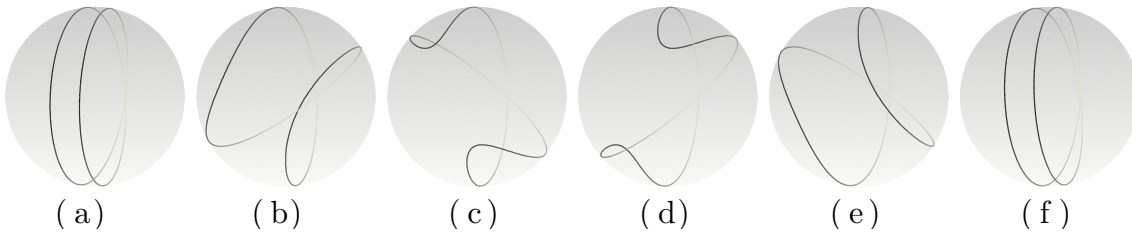
Figure 4.10: Snapshots of the closed loop on the unit sphere traced by the spin vector – the indicatrix, for the breather spin mode ($m = 1$, $n = 2$). The indicatrix intersects itself once, which is preserved throughout the time evolution. The curve is symmetric about the great circle passing through the intersection. Keeping in mind the direction of the loop, total area covered by the loop on the surface of the sphere remains a constant (4π). For detailed animation, see the supplementary material: indicatrix.avi .

4.7 Spinor association

We have already shown that the HF spin chain demonstrates the 'belt trick' during the breather excitation. Basic fact behind the belt trick is the contractibility of loops in the parameter space of $\mathrm{SO}(3)$, as illustrated in Fig. 4.9. However, an explicit connection between the group manifold and the spin dynamics was not presented there. In this section, we will examine the breather excitation in the spin chain by visualizing it in the $\mathrm{SU}(2)$ group manifold. The Lie group $\mathrm{SU}(2)$ comes into the picture for two reasons:

1. There exist a group homomorphism between $\mathrm{SU}(2)$ and $\mathrm{SO}(3)$. Therefore, the belt trick can also be seen in $\mathrm{SU}(2)$.

2. The Lax pair (2.14) for the NLSE has a fundamental solution $\mathbf{\Psi}$, which is an element of $\mathrm{SU}(2)$. Gauge equivalence implies that, for each spin configuration $\hat{\mathbf{S}}$, there exist a solution ψ to the NLSE. This ψ and the fundamental solution $\mathbf{\Psi}$ are always correlated. Therefore the belt trick seen in the spin breather must be present in $\mathbf{\Psi}$.

4.7.1 $\mathrm{SU}(2)$ group and angle doubling

Group $\mathrm{SU}(2)$ is the set of 2×2 complex matrices U, such that $U^\dagger = U^{-1}$ and $\det U = 1$. It can be conveniently written as,

$$U = \begin{pmatrix} r & -\overline{s} \\ s & \overline{r} \end{pmatrix}, \quad |r|^2 + |s|^2 = 1, \tag{4.49}$$

where r and s are arbitrary complex numbers [137]. With the additional constraint on the determinant, r and s can be specified by three real numbers. Thus the dimension of $\mathrm{SU}(2)$ group is three. Being a matrix Lie group, $\mathrm{SU}(2)$ can be represented by the exponential map [143]:

$$\exp : \mathfrak{su}(2) \longrightarrow \mathrm{SU}(2), \tag{4.50}$$

where $\mathfrak{su}(2)$ is the Lie algebra spanned by Pauli matrices,

$$\sigma_1 = \begin{pmatrix} 0 & 1 \\ 1 & 0 \end{pmatrix}, \quad \sigma_2 = \begin{pmatrix} 0 & -i \\ i & 0 \end{pmatrix}, \text{ and } \sigma_3 = \begin{pmatrix} 1 & 0 \\ 0 & -1 \end{pmatrix}. \tag{4.51}$$

Any element $U \in \mathrm{SU}(2)$ can be written as

$$U = e^{-i(\theta/2)(\hat{\mathbf{n}} \cdot \vec{\sigma})}, \tag{4.52}$$

71

where $\hat{\mathbf{n}} = \{n_1, n_2, n_3\}$, $\boldsymbol{\sigma} = \{\sigma_1, \sigma_2, \sigma_3\}$ and θ is a real number. To represent U, three parameters are needed — one for θ, and two for $\hat{\mathbf{n}}$, since $|\hat{\mathbf{n}}| = 1$. One can compute the matrix exponential to arrive at a more convenient expression [137, 143]. Let $\mathcal{K} = -i(\hat{\mathbf{n}} \cdot \boldsymbol{\vec{\sigma}})$. It follows that,

$$\mathcal{K} = -i(\hat{\mathbf{n}} \cdot \boldsymbol{\vec{\sigma}}) = \begin{pmatrix} -in_3 & -n_2 - in_1 \\ n_2 - in_1 & in_3 \end{pmatrix}, \quad \mathcal{K}^2 = -\mathbf{I}. \tag{4.53}$$

Series expansion gives,

$$\begin{aligned} e^{(\theta/2)\mathcal{K}} &= \mathbf{I} + (\theta/2)\mathcal{K} + \frac{1}{2!}(\theta/2)^2\mathcal{K}^2 + \frac{1}{3!}(\theta/2)^3\mathcal{K}^3 + \frac{1}{4!}(\theta/2)^4\mathcal{K}^4 + \cdots \\ &= \mathbf{I} + (\theta/2)\mathcal{K} - \frac{1}{2!}(\theta/2)^2\mathbf{I} - \frac{1}{3!}(\theta/2)^3\mathcal{K} + \frac{1}{4!}(\theta/2)^4\mathbf{I} - \cdots \\ &= \mathbf{I}\left(1 - \frac{1}{2!}(\theta/2)^2 + \frac{1}{4!}(\theta/2)^4 - \cdots\right) + \mathcal{K}\left((\theta/2) - \frac{1}{3!}(\theta/2)^3 + \cdots\right) \\ &= \mathbf{I}\cos(\theta/2) + \mathcal{K}\sin(\theta/2). \end{aligned} \tag{4.54}$$

Finally, the general expression for $\mathrm{SU}(2)$ matrix [136, p. 100] is written as,

$$U(\hat{\mathbf{n}}, \theta) = e^{-i(\theta/2)(\hat{\mathbf{n}} \cdot \boldsymbol{\vec{\sigma}})} = \mathbf{I}\cos(\theta/2) - i(\hat{\mathbf{n}} \cdot \boldsymbol{\vec{\sigma}})\sin(\theta/2). \tag{4.55}$$

Comparing (4.55) with (4.40), one can see that $U(\hat{\mathbf{n}}, \theta)$ is generated by the following set of 2×2 matrices,

$$K_1 = \frac{\sigma_1}{2}, \quad K_2 = \frac{\sigma_2}{2}, \text{ and } \quad K_3 = \frac{\sigma_3}{2}, \tag{4.56}$$

for which, the commutation relations can be found to be,

$$[K_i, K_j] = i\epsilon_{ijk}K_k. \tag{4.57}$$

Comparing this with (4.41), one can see that the commutation relations for generators of $\mathrm{SU}(2)$ is identical to that of $\mathrm{SO}(3)$. Further, it is to be noted that both the generators (4.36) and (4.56) are traceless Hermitian matrices. In brief, $\mathfrak{su}(2)$ and $\mathfrak{so}(3)$ are isomorphic Lie algebras [138, p. 116].

At this point, one contrast between $\mathrm{SU}(2)$ and $\mathrm{SO}(3)$ can be made. As the rotation angle varies through 4π, it can be seen from (4.55) that,

$$U(\hat{\mathbf{n}}, \theta + 2\pi) = -U(\hat{\mathbf{n}}, \theta), \text{ and } \quad U(\hat{\mathbf{n}}, \theta + 4\pi) = U(\hat{\mathbf{n}}, \theta). \tag{4.58}$$

Thus, the rotation period for $SU(2)$ is 4π, unlike 2π for $SO(3)$. A 2π rotation never brings back the element towards the initial state, instead it changes sign [144].

There exists a homomorphism between $SU(2)$ and $SO(3)$, which is a two-to-one mapping,

$$\Phi: \quad SU(2) \xrightarrow{2:1} SO(3), \quad \Phi(U) = R, \tag{4.59}$$

where $U \in SU(2)$ and $R \in SO(3)$. We omit the details of the mapping here. This homomorphism is often called 'Double cover', since two distinct elements of $SU(2)$ is being mapped to an element of $SO(3)$. In other words, $\Phi(U) = \Phi(-U) = R$. This is why R is unchanged by a rotation $\theta = 2\pi$. A complete rotation forms a closed curve in $SO(3)$ but not in $SU(2)$ because the curve starts from U and ends in $-U$. Two complete rotation can form a closed curve in $SU(2)$. Moreover, $SU(2)$ is simply connected with fundamental group $\{1\}$, which implies that every closed curves are contractible. On the other hand, for $SO(3)$, the fundamental group is $\{1, -1\}$, which is the reason why it is doubly connected with two distinct types of closed curves [138].

For a given element of $SU(2)$, the parameters θ and $\hat{\mathbf{n}}$ can be found by comparing (4.49) and (4.55). We write the required relations explicitly,

$$\begin{aligned}
\cos(\theta/2) &= \text{Re}(r), \\
n_1 \sin(\theta/2) &= -\text{Im}(s), \\
n_2 \sin(\theta/2) &= \text{Re}(s), \\
n_3 \sin(\theta/2) &= -\text{Im}(r).
\end{aligned} \tag{4.60}$$

Although θ varies from 0 to 4π in a period, it is possible to represent the matrix $U(\hat{\mathbf{n}}, \theta)$ within a range $0 < \theta < \pi$. Using (4.55), one can find the appropriate representation of U which falls in ranges $0 \to \pi$, $\pi \to 2\pi$, $2\pi \to 3\pi$ and $3\pi \to 4\pi$ as follows:

$$\begin{aligned}
0 \to \pi; & \quad U(\hat{\mathbf{n}}, \theta), \\
\pi \to 2\pi; & \quad U(\hat{\mathbf{n}}, \pi + \theta) &= -U(-\hat{\mathbf{n}}, \pi - \theta), \\
2\pi \to 3\pi; & \quad U(\hat{\mathbf{n}}, 2\pi + \theta) &= -U(\hat{\mathbf{n}}, \theta), \\
3\pi \to 4\pi; & \quad U(\hat{\mathbf{n}}, 3\pi + \theta) &= U(-\hat{\mathbf{n}}, \pi - \theta).
\end{aligned} \tag{4.61}$$

4.7.2 Belt trick seen in $SU(2)$ group manifold

A matrix element of $SO(3)$ rotates a vector in $\mathbb{R}^3$. Likewise, an element of $SU(2)$ rotates a *spinor* — vector in a 2-d complex vector space [145, 144]. We will show that the rotation

of the spinor is closely related with the dynamics of the spin chain. Without explicitly expressing the spinor, we will give the $\mathrm{SU}(2)$ elements responsible for the spinor evolution.

Every spin configuration is related to a solution to the NLSE via gauge equivalence. The Lax pair (2.14) for the NLSE has a fundamental solution $\mathbf{\Psi}$, which is an element of $\mathrm{SU}(2)$. This enables us to think of a set $\{\psi, \mathbf{\Psi}, \hat{\mathbf{S}}\}$. For a complete picture, see the Table 4.1, which summarizes various solutions presented in this work. Thus we argue that, there exist a close relationship between the dynamics of classical HF spin chain and the rotation matrix in $\mathrm{SU}(2)$. The belt trick seen in the spin breather must be present in $\mathrm{SU}(2)$, since $\mathbf{S} = \lim_{\lambda \to 0} \mathbf{\Psi}^\dagger \sigma_3 \mathbf{\Psi}$. In this section, we will examine these $\mathrm{SU}(2)$ elements by finding their axis-angle parametrization. Evolution of the closed curve in the group manifold will also be discussed in detail.

Table 4.1: The relationship between NLSE, HF spin chain and their solutions.

NLSE	Lax pair	HF spin chain
$i\psi_t + \psi_{xx} + 2\|\psi\|^2\psi = 0$	$\mathbf{\Psi}_x = U\mathbf{\Psi},\ \mathbf{\Psi}_t = V\mathbf{\Psi}$	$\hat{\mathbf{S}}_t = \hat{\mathbf{S}} \times \hat{\mathbf{S}}_{xx}, \qquad \hat{\mathbf{S}}^2 = 1$
$\psi \in \mathbb{C}$	$\mathbf{\Psi} \in \mathrm{SU}(2)$	$\mathbf{S} = \lim_{\lambda \to 0} \mathbf{\Psi}^\dagger \sigma_3 \mathbf{\Psi} \in \mathfrak{su}(2)$
ψ_c (seed) Eq. (4.6)	$\mathbf{\Psi}_c$ Eq. (4.8)	$\mathbf{S}_c$ Eq. (4.11)
ψ_{cb} (breather) Eq. (4.17)	$\mathbf{\Psi}_{cb}$ Eq. (4.15)	$\mathbf{S}_{cb}$ Eq. (4.19)
$\begin{array}{l} \lambda_0 = ia \\ \kappa_0 > a \end{array}$		
ψ_{AB} (AB) Eq. (3.23)	$\lim_{\lambda \to 0} \mathbf{\Psi}_{cb}$ Eq. (4.64)	$\mathbf{S}_{cb}$ (simplified) (4.25) (4.28)

4.7.2.1   Seed spin and $\mathbf{\Psi}_c$

Since everything is compiled together in Table 4.1, without further explanation we move on to the fundamental solution associated with the seed spin. The seed spin is explicitly obtained in section 4.3.2 using the expression, $\mathbf{S}_c = \lim_{\lambda \to 0} \mathbf{\Psi}_c{}^\dagger \sigma_3 \mathbf{\Psi}_c$. Out of all λ-family of solutions, the one with $\lambda \to 0$ is entering in the spin configuration. Therefore, we argue that the features seen in the spin chain are present in $\mathbf{\Psi}_c$ in the limit $\lambda \to 0$. It can be written

as (details are provided in Appendix B),

$$\lim_{\lambda \to 0} \mathbf{\Psi}_c(x, t, \lambda) = \begin{pmatrix} \cos(\kappa_0 x - \frac{\pi}{4}) \, e^{i(\kappa_0^2 t - \frac{\pi}{4})} & i \sin(\kappa_0 x - \frac{\pi}{4}) \, e^{i(\kappa_0^2 t - \frac{\pi}{4})} \\ i \sin(\kappa_0 x - \frac{\pi}{4}) \, e^{-i(\kappa_0^2 t - \frac{\pi}{4})} & \cos(\kappa_0 x - \frac{\pi}{4}) \, e^{-i(\kappa_0^2 t - \frac{\pi}{4})} \end{pmatrix}$$

$$= \begin{pmatrix} e^{i(\kappa_0^2 t - \frac{\pi}{4})} & 0 \\ 0 & e^{-i(\kappa_0^2 t - \frac{\pi}{4})} \end{pmatrix} \begin{pmatrix} \cos(\kappa_0 x - \frac{\pi}{4}) & i \sin(\kappa_0 x - \frac{\pi}{4}) \\ i \sin(\kappa_0 x - \frac{\pi}{4}) & \cos(\kappa_0 x - \frac{\pi}{4}) \end{pmatrix} \quad (4.62)$$

$$= e^{i\sigma_3(\kappa_0^2 t - \frac{\pi}{4})} \cdot e^{i\sigma_1(\kappa_0 x - \frac{\pi}{4})}$$

$$= e^{i\sigma_3(\kappa_0^2 t - \frac{\pi}{4})} \cdot e^{i\sigma_1(\Theta/2)},$$

with $\Theta/2 + \frac{\pi}{4} = \kappa_o x = \frac{n\pi x}{L}$. We have used the matrix exponential relation (4.55) for writing the matrix in the final form. In this form, it appears to be a combination of rotations about σ_3 and σ_1 axis which are respectively the $\hat{\mathbf{z}}$ and $\hat{\mathbf{x}}$ directions in $\mathbb{R}^3$. Using the gauge equivalence, the spin field in the matrix form (4.10) can be calculated as,

$$\mathbf{S}_c(x, t) = e^{-i\sigma_1 \Theta/2} e^{-i\sigma_3(\kappa_0^2 t - \frac{\pi}{4})} \sigma_3 \, e^{i\sigma_3(\kappa_0^2 t - \frac{\pi}{4})} e^{i\sigma_1 \Theta/2}$$

$$= e^{-i\sigma_1 \Theta/2} \sigma_3 \, e^{i\sigma_1 \Theta/2} \quad (4.63)$$

$$= \cos(2\kappa_0 x)\sigma_2 + \sin(2\kappa_0 x)\sigma_3 = \mathbf{S}_c(x, 0),$$

the seed solution, as given in (4.11).

Further, it can be seen from (4.62) that at any instant of time, say $t = \pi/4\kappa_0^2$ for simplicity, the rotation is about $\hat{\mathbf{x}}$ (or σ_1) through an angle Θ. For $n = 1$, angle Θ varies from 0 to 2π since $0 < x < L$. Recall the angle doubling scenario explained in the previous subsection. A rotation of 2π form a diametrical line along $\hat{\mathbf{x}}$ in the $\mathrm{SO}(3)$ group manifold — in fact a closed loop, signifying a complete rotation in $\mathbb{R}^3$. However, the $\mathrm{SU}(2)$ matrix, $\mathbf{\Psi}_c$ (4.62) simply changes sign and never form a closed loop in its manifold. Angle doubling can be seen from the argument of trigonometric functions appearing in (4.62) and (4.63). For $n = 2$, therefore $0 \le \Theta < 4\pi$, corresponds to two overlapping diametrical lines, indicating two complete rotations (for $\mathbf{S}_c$). Hence, with 4π rotation, $\mathbf{\Psi}_c$ (4.62) comes back to the initial form, thereby making a closed loop in $\mathrm{SU}(2)$.

Notice the time dependence in (4.62), we infer that there is a rotation about $\hat{\mathbf{z}}$ (or σ_3) in the time evolution, with period $2\pi/\kappa_0^2 (= 2L^2/\pi)$. During this time period the diametric line completes one full global rotation.

4.7.2.2 Spin breather and Ψ_{cb}

From the seed solution, we are now moving towards the breather mode. Although we have obtained a general expression for breather, the current study of belt trick is based on a spatially periodic case with the choice of $\lambda_{0R} = 0$ and $\kappa_0 > \lambda_{0I}$. The corresponding spin breather (a reduced expression) is given in (4.25), along with variables defined in (4.28). This is essentially a counterpart of the Akhmediev breather in HF spin chain. Spin breather is explicitly obtained in section 4.4.3 by the relation, $\mathbf{S}_{cb} = \lim_{\lambda \to 0} \Psi_{cb}{}^{\dagger} \sigma_3 \Psi_{cb}$. In order to examine the belt trick, the matrix Ψ_{cb} has to be expressed for $\lambda = 0$, $\lambda_{0R} = 0$, and $\kappa_0 > \lambda_{0I}$. We rewrite Ψ_{cb} (4.15) below in the required limit:

$$\lim_{\lambda \to 0} \Psi_{cb} = \lim_{\lambda \to 0} \frac{1}{\sqrt{d_1}} \mathbf{P}_1 \Psi_c , \tag{4.64}$$

where $\mathbf{P}_1$ is the Darboux matrix given in (4.13), and $d_1 = |\mathbf{P}_1|$. Matrix Ψ_c is already given in the required limit in (4.62). For the Darboux matrix $\mathbf{P}_1$, we have computed the limit $\lambda_{0R} = 0$ and $\lambda = 0$, in section B.31 of Appendix B. Thus we write,

$$\lim_{\lambda \to 0} \frac{1}{\sqrt{d_1}} \mathbf{P}_1(x, t, \lambda, \lambda_0) = \frac{1}{\Delta} \begin{pmatrix} -i\gamma & -e^{2i\kappa_0^2 t}(\beta + i\alpha) \\ e^{-2i\kappa_0^2 t}(\beta - i\alpha) & i\gamma \end{pmatrix}, \tag{4.65}$$

with α, β, γ and Δ as in (4.28). Since $\alpha^2 + \beta^2 + \gamma^2 = \Delta^2$, we may define variables A and B in the following form,

$$\sin A \, \cos B = \frac{\beta}{\Delta}, \quad \sin A \, \sin B = \frac{\alpha}{\Delta}, \quad \cos A = \frac{\gamma}{\Delta}, \tag{4.66}$$

so that (4.65) may be rewritten as,

$$\lim_{\lambda \to 0} \frac{1}{\sqrt{d_1}} \mathbf{P}_1 = \begin{pmatrix} -i\cos A & -\sin A \, e^{i(B + 2\kappa_0^2 t)} \\ \sin A \, e^{-i(B + 2\kappa_0^2 t)} & i\cos A \end{pmatrix}. \tag{4.67}$$

Since it is an $\mathrm{SU}(2)$ element, one can visualize this as a rotation (4.55). Corresponding axis $\hat{\mathbf{n}} = \{n_1, n_2, n_3\}$ and angle θ can be obtained from (4.60). Hence, right hand side of (4.67) is a rotation about the axis $\hat{\mathbf{n}}(x, t) = \{\sin A \, \sin(B + 2\kappa_0^2 t), \sin A \, \cos(B + 2\kappa_0^2 t), \cos A\}$, but peculiarly through a constant angle π. However, the direction $\hat{\mathbf{n}}(x, t)$ is obscured by the complicated form of the variables in (4.28).

In what follows, we will visualize the belt trick in group manifold. Evolution of the spin chain is previously shown in Fig. 4.3. We will show next, how does the corresponding

76

SU(2) elements (4.64) evolve in time. We first obtained the axis angle parametrization $(\hat{\mathbf{n}}, \theta)$ using (4.60). The parameter space, is an open sphere of radius π with antipodal points identified. Therefore the range of θ lies in between 0 and π as per the relations given in (4.61). In the case of SU(2) we will follow a formalism where U and $-U$ are indicated by the same point inside the sphere. This will essentially become a $2 \rightarrow 1$ mapping from SU(2) to SO(3). Thus a single diametrical line seen in this parameter space does not mean a closed curve in SU(2), because the curve merely connects the identity element I with $-I$. Note that both of them mapped to the same element in SO(3) which is the identity in that group — hence the curve represent a complete rotation (for the spin vector).

We give a detailed plot of the group element in Fig. 4.11 as a series of events taken from the time evolution. For large $|t|$ values, rogue breather dynamics approaches the seed spin configuration. It is obvious that the seed spin with $n = 2$, makes two overlapping diametrical lines in the group manifold. This is a closed loop, both in SU(2) and SO(3). As the system evolves towards the rogue event, these two diametrical lines seen in Fig. 4.11(a) starts to separate and deform continuously. Antipodal pairs are marked in the same color. It is clear from the plots that any motion of a particular antipodal point (say, red) over the surface, must be accompanied with a motion of the corresponding point (red) on the other side. In the due course (Fig. 4.11(a)–(f)), the size of one line keep decreasing, vanishing eventually, permitting the other to connect into a closed loop. This closed loop seen in Fig. 4.11(f)–(j), resides entirely within the sphere without touching the surface. In principle, this closed loop can be shrunk to a point through continuous deformation — thus it is topologically equivalent to a point. However, a single point in the manifold corresponds to zero energy for the 1-d isotropic spin field. Since our classical HF spin chain is a conservative system, such 'shrinking' will not occur in this dynamics. If dissipation effects are also incorporated, one can expect a 'shrinking' from the closed loop eventually reducing to a point. Further stages of the rogue breather evolution in Fig. 4.11(h)–(o), shows its symmetric nature in time, as is expected. At the end, it results in two overlapping diametrical lines where it started from.

On a technical note we want to remark that, all the curves seen in the Fig. 4.11 start with the identity — the center of the sphere. In general this is not guaranteed in (4.64). As discussed above, the matrices given in (4.67) and (4.62) have complicated evolution, even in time. To make the analysis more convenient we deliberately fixed the first element at the center of the sphere. However this is no way alters the conclusions discussed in this work. For example, consider an arbitrary curve parametrized by its arc length $\boldsymbol{r}(s)$, where $\boldsymbol{r}(0) \neq \vec{0}$. One can define $\boldsymbol{r}'(s) = \boldsymbol{r}(s) - \boldsymbol{r}(0)$, such that $\boldsymbol{r}'(s)$ is identical to $\boldsymbol{r}(s)$, but

(a) (b) (c) (d) (e) (f) (g) (h)

(i) (j) (k) (l) (m) (n) (o)
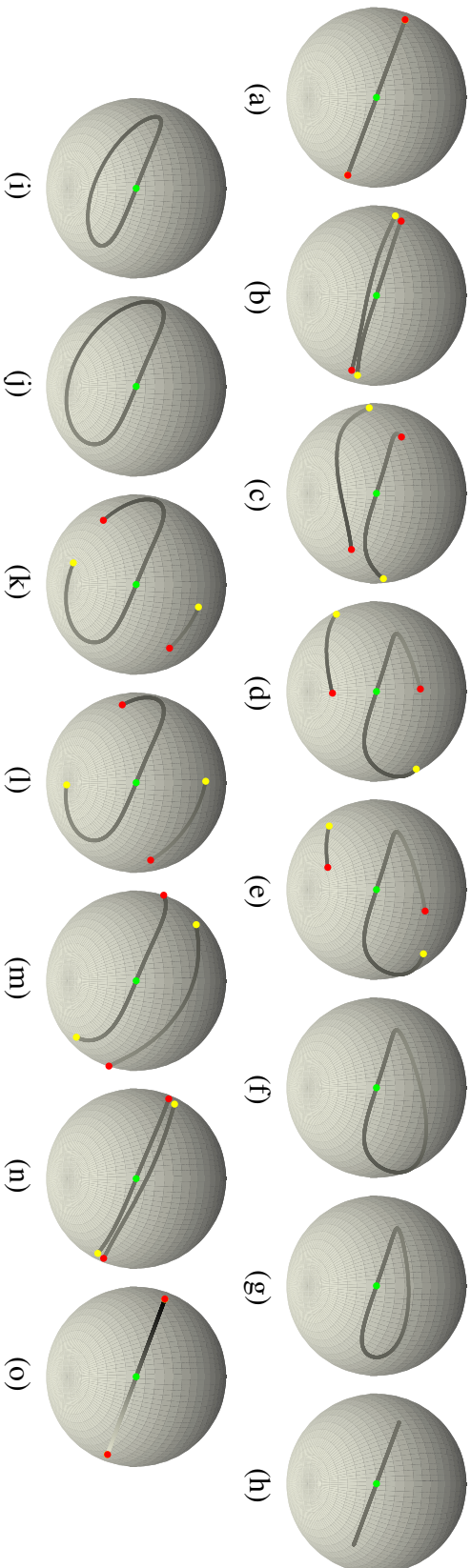
Figure 4.11: The breather mode as seen in the group manifold — an open sphere of radius π, with antipodal points identified. For $m = 1$ and $n = 2$ (two turn), the seed solution, (4.11), corresponds to two overlapping diametrical lines. The antipodal pairs are indicated by dots of the same color. In the process of the breather mode evolution the two lines join to form a closed loop within the sphere (f), which can be then shrunk to a point continuously if dissipation is incorporated. The same cannot be achieved for a case with $n = 1$ (one turn) — a single line connecting two antipodal points. For detailed animation, see the supplementary material: topology.avi .

78

starts from the origin. Likewise, the matrix $U \in \mathrm{SU}(2)$ at a particular instant of time t, be parametrized by x. As x varies from 0 to L, matrix $U(x)$ draws a closed curve in the parameter space. In general $U(x = 0) \neq \mathbf{I}$, hence the curve does not start from the center. In this work. this issue is bypassed by defining $U'(x) = U(0)^{-1}U(x)$. What is seen in the Fig. 4.11 is thus $U'(x)$.

The parameter space shown in Fig. 4.11 does not distinguish an element U from $-U$ (refer (4.61) for details). Hence it is essentially a group homomorphism (4.59). One can explicitly do this by constructing an $\mathrm{SO}(3)$ matrix right from the $\mathrm{SU}(2)$ element [80, p. 373]. Then the axis angle parametrization for this $\mathrm{SO}(3)$ matrix can be easily obtained from (4.40). We observed that the evolution of the closed curve in this procedure is identical to that of Fig. 4.11, as is expected.

Breathers are not possible with $n = 1$. However, we would like to point out one topological aspect it has in contrast with $n = 2$. In principle, two diametrical lines can be shrunk to a point. In the case of a single diametrical line ($n = 1$), the end points are always identified. As one of them moves along the surface, so does the other, keeping them always at opposite ends. Hence they will never be able to join together to form a closed loop that resides perfectly within the sphere. Therefore, a diametrical line in the group manifold cannot be shrunk to a point. In other words 2π rotations are topologically non-trivial, while 4π rotations are trivial. This is indeed the gist of the belt trick. Topologically, a breather mode with $n = 2$ or any other with an 'even' twist are thus equivalent. This is distinct from those breather modes, with n as odd number. Thus depending on the nature of their total twist, T_w — 'odd' or 'even', entire collection of breather modes can be grouped into two distinct classes. Our study is based on an integrable system, where the energy is conserved. But in a modified system [32] that includes dissipation and other such factors, a spin configuration with higher twist T_w, can be transformed to a configuration with twist $T_w - 2$, and eventually to a configuration with lowest possible twist in its class — either '0' or '1', through breather like excitations.

4.8   Energy bounds and topological sectors

We have shown that spin field with spatial periodicity fall into two distinct classes, as a consequence of the fact that $\mathrm{SO}(3)$ group manifold is doubly connected. In addition, it can be shown that their energy is bounded from below. It is possible to define a mapping from 1-d spin chain into a space curve parametrized by its arc length. Here, each spin vector, which is of unit magnitude is identified with the unit tangent of the curve. More precisely,

if $\mathbf{R}(x)$ is the position vector of space curve, and x being its arc length, then

$$\frac{d\mathbf{R}(x)}{dx} \equiv \hat{\mathbf{S}}(x). \tag{4.68}$$

The unit moduli of $\hat{\mathbf{S}}(x)$ implies that $\mathbf{R}(x)$ is non-stretching. A spin chain can have a total spin,

$$\mathbf{S}_{tot} = \oint \hat{\mathbf{S}}\, dx, \tag{4.69}$$

which is a constant of the time evolution. This is also a consequence of the global rotation symmetry of the Heisenberg Hamiltonian. Spatially periodic spin configurations that are discussed in this chapter, in fact correspond to $\mathbf{S}_{tot} = 0$. This additional condition, $\mathbf{S}_{tot} = 0$, thus corresponds to a closed curve in 3 dimension ($\oint d\mathbf{R} = 0$). In the case of the indicatrix — the curve traced by $\hat{\mathbf{S}}$ on the unit sphere, spatial periodicity of the spin field alone can provide a closed curve. In addition, a zero total spin gives a closed indicatrix that cannot be confined to any single hemisphere [146], no matter which way one looks at it (see for instance Fig. 4.10).

The curve $\mathbf{R}(x)$ with tangent vector identification $\hat{\mathbf{e}}_1 = \hat{\mathbf{S}}$ has curvature $\kappa = |\hat{\mathbf{e}}_{1x}| = |\frac{\partial \hat{\mathbf{S}}}{\partial x}|$. The total curvature of any closed curve must be greater that 2π. This is a fact well know in differential geometry as Fenchel's theorem [147, 148], which may be written as,

$$\oint \kappa dx \geq 2\pi. \tag{4.70}$$

Using Cauchy-Schwarz inequality [146], we have

$$L \oint \kappa^2 dx \geq \left(\oint \kappa dx \right)^2, \tag{4.71}$$

Since $\kappa = |\frac{\partial \hat{\mathbf{S}}}{\partial x}|$, the energy density turn out to be κ^2 from (4.3). Substituting (4.70) in (4.71), one can arrive at the energy lower bound for the spin configuration [149]

$$E_{Total} \geq 4\pi^2/L. \tag{4.72}$$

However, the energy does not have an upper bound, since the spin chain can take any integer value for n.

The rogue breather dynamics we have studied in this chapter is an exact solution for HF model given in (4.2), which is an integrale system free of any dissipation. In this dynamics, we show that the spin configuration with total twist T_w can be contiuously transformed to

one with twist $T_w - 2$ which is a short lived intermediate phase. Later, the spin configuration goes back to its initial configuration where it has started with. If dissipation effects, such as Gilbert damping [150] are to be included, system will not revert to its initial configuration. Breather excitation can thus transform any spin configuration with twist T_w continuously to one with a total twist of $T_w - 2$, and eventually to a twist of either '0' or '1'. Thus we obtain a more general lower bound for the total energy of the spin chain with periodic boundary condition, determined by its twist:

$$ E_{Total} \geq \begin{cases} 0 & \text{for 'even' twist,} \\ 4\pi^2/L & \text{for 'odd' twist.} \end{cases} \tag{4.73} $$

Hence, a spin configuration with given $\hat{\mathbf{S}}_{tot}$, fall into two distinct topological classes, due to the fact that the fundamental group of $SO(3)$ is $\mathbb{Z}_2$. Further, HF model admits soliton solution in the form of *breather* modes, as a mediator shifting the total twist of the chain by '2'.

4.9   Conclusion

We have studied the breather excitation in classical HF spin chain. An exact analytical expression for the spin breather is presented. Of particular interest for our studies, we focused on a spatially periodic case which is essentially an analogue of Akhmediev breather in the HF model.

It is shown that the spin chain demonstrates the 'belt-trick' during the breather excitation. The belt trick, also known as 'Dirac string trick' is often used to illustrate the triviality of 4π rotation. A finite spin chain with two complete turns between its ends may be continuously transformed to a chain wherein net rotation is surprisingly zero. This peculiar topological feature, even though theoretically well understood, has so far not been witnessed in a physical model to the best of our knowledge. In view of the recurrence phenomena seen in various integrable systems, we find that after the belt trick demonstration the initial configuration of the spin chain is exactly recovered.

Evolution of the spin chain has also been visualized in the group manifold. Close relation between the spin field and the $SU(2)$ element, arising naturally in the framework of soliton theory, is explored in detail.

We have also pointed out that the total energy of the spin chain has a lower bound, depending inversely on the size of the chain. If dissipation effects were to be regarded,

the configuration space is broadly reduced to two topological sectors with distinct energy lower bounds, determined by their total twist — 'odd' or 'even'.

Chapter 5

Recurrence process in the Heisenberg ferromagnetic spin chain

5.1 Introduction

HF spin chain demonstrates the 'belt trick' during a breather excitation. This peculiar geometrical feature has been discussed in Chapter 4 wherein the background spin configuration is a static field. In this chapter one more spin breather solution is constructed which shows the 'belt trick' behaviour. This is distinct from the former in the sense that its background field is time dependent. The new spin breather presented here can be thought of as the tangent vector of the knotted space curve discussed in Chapter 3. Both the breather modes studied in this thesis (Chapter 4 and 5) are found to exhibit the 'belt trick behaviour', as if this peculiar feature is a general characteristics of the NLSE breather solution.

We start with a plane wave solution $\psi_{\mathrm{h}} = \kappa_0 e^{i\sqrt{2}\,\kappa_0 x}$, to obtain a breather as explained in Chapter 3. Spin configuration associated with this breather solution is constructed explicitly using gauge equivalence. Spatially periodic spin breather is studied in detail as a special case. An additional global rotation is observed in the background spin chain due to the breather excitation. Although the spin chain goes back to its initial configuration, this additional rotations clearly distinguish the initial and final state of the system.

In the case of Akhmediev breather, it is known that the initial and final phase of the complex field has a shift. The significance of the additional global rotation in the spin chain (analogous to the 'phase shift') in the context of FPUT recurrence is discussed. However, this scenario is absent in the spin breather studied in Chapter 4. A qualitative distinction of the two spin breathers in this regard is pointed out.

5.2 Seed solution: a rotating spin chain

For each solution ψ to the NLSE, there is one auxiliary matrix function $\mathbf{\Psi}$ as a solution to the corresponding Lax pair. Spin configuration associated with ψ is obtainable via gauge equivalence, $\mathbf{S} = \lim_{\lambda \to 0} \mathbf{\Psi}^\dagger \sigma_3 \mathbf{\Psi}$, which then can be expressed in vector form $\hat{\mathbf{S}} \equiv (S_1, S_2, S_3)$ as explained in Sec. 2.3. This is the procedure followed in Chapter 4, wherein the background spin field (4.11) is a static field (time independent) which is associated to the seed solution $\psi_\mathrm{c} = \kappa_0\, e^{2i\kappa_0^2 t}$.

Here in this chapter, we begins with a seed solution,

$$\psi_\mathrm{h} = \kappa_0 e^{i\sqrt{2}\,\kappa_0 x} \tag{5.1}$$

where κ_0 is a real constant. Suffix h denotes the associated space curve — helix (Fig. 1.3 (c)). One can construct the spin field associated with ψ_h, using the expression,

$$\mathbf{S}_\mathrm{h} = \lim_{\lambda \to 0} \mathbf{\Psi}_\mathrm{h}^\dagger \sigma_3 \mathbf{\Psi}_\mathrm{h} \tag{5.2}$$

where $\mathbf{\Psi}_\mathrm{h}$ is given in (3.9). Following a straightforward calculation, the explicit expression for the seed spin may be written as,

$$\hat{\mathbf{S}}_\mathrm{h} = \sqrt{\frac{2}{3}} \left(\frac{1}{\sqrt{2}}\,\hat{\mathbf{i}} + \cos\theta\,\hat{\mathbf{j}} + \sin\theta\,\hat{\mathbf{k}} \right), \tag{5.3}$$

where $\theta = \sqrt{6}\kappa_0(x - \sqrt{2}\kappa_0 t)$. This spin configuration has a uniform rotation about the x-axis with time period $T_0 = \pi/(\sqrt{3}\kappa_0^2)$, and a spatial period $L_1 = \sqrt{2}\pi/(\sqrt{3}\kappa_0)$ such that $\hat{\mathbf{S}}_\mathrm{h}(x, t) = \hat{\mathbf{S}}_\mathrm{h}(x + nL_1, t)$, for an integer n. The spin field $\hat{\mathbf{S}}_\mathrm{h}$ is shown in Fig. 5.1 taking the lattice sites along x- axis, where the rotation of the chain as a whole about the axis is implied. Hence this spin field is a dynamical field unlike the previously discussed static field seen in Fig. 4.1 . Energy density (4.3) can be found to be, $E_0 = |\hat{\mathbf{S}}_{\mathrm{h},x}|^2 = 4|\psi_h|^2 = 4\kappa_0^2$.

5.3 Spin breather modes over the rotating spin chain

We are investigating the breather excitation over the background spin field $\hat{\mathbf{S}}_\mathrm{h}$ (5.3). Breather solution over the plane wave ψ_h using DT technique has already been discussed in Chapter 3. The breather solution ψ_1 (3.15), is explicitly obtained for which the associated space

curve in knotted. Here we extend the result towards HF spin chain using the relation,

$$\mathbf{S}_1 = \lim_{\lambda \to 0} \mathbf{\Psi}_1^\dagger \sigma_3 \mathbf{\Psi}_1 \qquad (5.4)$$

where $\mathbf{\Psi}_1$ (3.13) is the solution to the Lax pair corresponding to the breather ψ_1 (3.15).

Calculation of the spin configuration $\hat{\mathbf{S}}_1$ is straightforward. Explicit expression for the spin breather is obtained as,

$$\hat{\mathbf{S}}_1(x,t) = \frac{\lambda_{0R}^2 - \lambda_{0I}^2}{|\lambda_0|^2}\hat{\mathbf{S}}_h + \left[-\frac{2\lambda_{0I}^2\xi}{|\lambda_0|^2\chi^2}\left(-\frac{(\sqrt{2}\eta + \xi)}{\sqrt{3}} \right) + \frac{2\lambda_{0I}\lambda_{0R}}{|\lambda_0|^2\chi}\left(-\frac{\sqrt{2}}{\sqrt{3}}\zeta \right) \right]\hat{\mathbf{i}}$$

$$+ \left[-\frac{2\lambda_{0I}^2\xi}{|\lambda_0|^2\chi^2}\left(\cos\theta\frac{(\eta - \sqrt{2}\xi)}{\sqrt{3}} - \zeta\sin\theta \right) + \frac{2\lambda_{0I}\lambda_{0R}}{|\lambda_0|^2\chi}\left(\frac{\zeta}{\sqrt{3}}\cos\theta + \eta\sin\theta \right) \right]\hat{\mathbf{j}}$$

$$+ \left[-\frac{2\lambda_{0I}^2\xi}{|\lambda_0|^2\chi^2}\left(\sin\theta\frac{(\eta - \sqrt{2}\xi)}{\sqrt{3}} + \zeta\cos\theta \right) + \frac{2\lambda_{0I}\lambda_{0R}}{|\lambda_0|^2\chi}\left(\frac{\zeta}{\sqrt{3}}\sin\theta - \eta\cos\theta \right) \right]\hat{\mathbf{k}}, \quad (5.5)$$

where, $\hat{\mathbf{S}}_h$ is the background spin field, and $\lambda_0(= \lambda_{0R} + i\lambda_{0I})$ is the scattering parameter in the language of IST. Functions ζ, η, ξ and χ are defined below (3.11), and θ is defined below (5.3).

Energy density of the spin breather is $E_1 = |\hat{\mathbf{S}}_{1,x}|^2 = 4|\psi_1|^2$, owing to the gauge equivalence [19]. Therefore breather profile shown in Fig. 3.4 will be identical to the energy profile in $x - t$ plane, upto a scaling. It is to be noted that, the spin breather $\hat{\mathbf{S}}_1$ (5.5) is cumbersome to analyse in its entire generality. But one can still have a spatially periodic, temporally periodic or even a rogue soliton by suitably choosing the concerned parameters as described in Fig. 3.4.

Spin breather $\hat{\mathbf{S}}_1$ is shown in Fig. 5.2 with nine frames in sequence taken from its time evolution. Uniform rotation about the lattice axis present in the seed spin can be seen as a global rotation. This is not necessary for the analysis and can be avoided in the plots for the sake of simplicity. For the particular choice of parameter (in general case), there is no spatial periodicity in the spin field. Therefore a spin chain of arbitrary length is taken which initially carry '3' turns between its boundaries. Same number of turn can be seen in the last frame as well. However, in the intermediate stage shown in Fig. 5.2 (e), the net turn is found to be '1'. Dynamics of each individual spin vector is smooth and continuous. But their collective behaviour shows a singular shift when considering the net turns in the spin chain, which in this case '3' to '1' and again to '3'. This feature is treated as the 'belt trick behaviour' of the spin breather mode. Corresponding indicatrix curve is shown in Fig. 5.3.

85
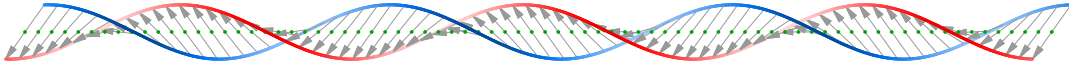
Figure 5.1: Spatially periodic dynamical spin field, $\hat{\mathbf{S}}_h$ (5.3) is shown with lattice sites lined up along the x - axis. Spin chain as a whole is rotating about the lattice axis with a time period T_0.

(a)

(b)

(c)

(d)

(e)

(f)

(g)

(h)

(i)
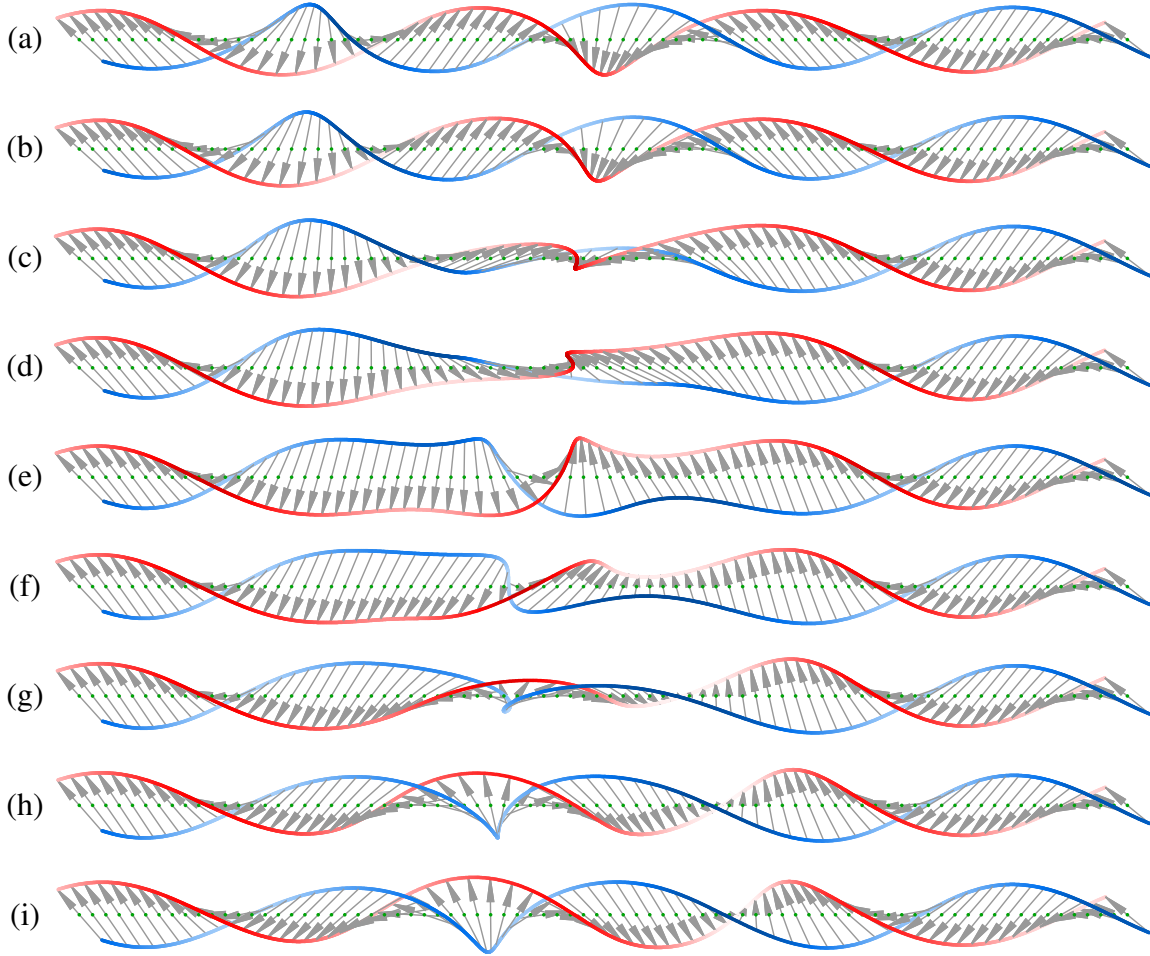
Figure 5.2: Spin breather $\hat{\mathbf{S}}_1$ (5.5) is shown at nine instances in its evolution for $\kappa_0 = 0.5$, $\lambda_0 = 0 + 0.5$. Loci of top of the spin vector is marked in color red, and that of bottom is marked in blue. (a) and (i) are shown to have '3' turns (windings) in the spin chain between its boundaries. Whereas in (e) the net turn is only '1'. This singular shift in terms of net turns — '3' to '1', is the 'belt trick behaviour' in the spin chain. Spatial periodicity is absent for this particular choice of parameter, therefore a spin chain of arbitrary length containing '3' turn is shown for the purpose of illustration. Uniform rotation about the lattice axis present in the background spin chain is canceled out for the ease of analysis. For detailed animation, see the supplementary material: belt_trick3.avi .
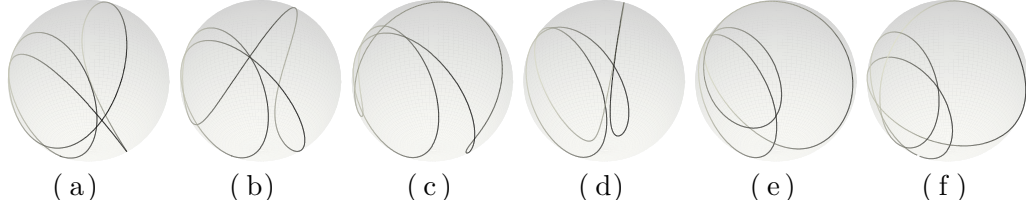
Figure 5.3: Indicatrix curve — curve spanned by $\hat{\mathbf{S}}_1$ on the surface of a unit sphere.

Spin field dynamics can also be seen in group manifold — an open sphere of radius π with antipodal points identified (for more details refer Sec. 4.7 and Fig. 4.11). The $\mathrm{SU}(2)$ connection arises from the fundamental solution to the Lax pair. For this particular breather solution one can see that the fundamental solution $\boldsymbol{\Psi}_{\mathrm{h}}$ (3.9) and $\boldsymbol{\Psi}_1$ (3.13) have a spatial period $2\sqrt{2}\pi/\kappa_0$ which does not commensurate with the spatial period $L_1 = \sqrt{2}\pi/(\sqrt{3}\kappa_0)$ of the seed spin $\hat{\mathbf{S}}_{\mathrm{h}}$ (5.3). Therefore even for the seed spin $\hat{\mathbf{S}}_{\mathrm{h}}$, the corresponding curve in the group manifold does not form a closed curve. This is shown in Fig. 5.4 (a). This open curve corresponds to the seed spin shown in Fig. 5.1 which carry '3' rotations. We note that, a matrix solution $\boldsymbol{\Psi}$ and $e^{i\Theta\sigma_3}\boldsymbol{\Psi}$ corresponds to the same spin field as shown below:

$$\mathbf{S} = \lim_{\lambda \to 0} \left(e^{i\Theta\sigma_3}\boldsymbol{\Psi}\right)^{\dagger}\sigma_3\left(e^{i\Theta\sigma_3}\boldsymbol{\Psi}\right) = \lim_{\lambda \to 0} \boldsymbol{\Psi}^{\dagger}e^{-i\Theta\sigma_3}\sigma_3 e^{i\Theta\sigma_3}\boldsymbol{\Psi} = \lim_{\lambda \to 0} \boldsymbol{\Psi}^{\dagger}\sigma_3\boldsymbol{\Psi}, \qquad (5.6)$$

where Θ is an arbitrary function of x and t. The periodicity in Θ does not reflect in the spin field. The matrix solution $\boldsymbol{\Psi}_{\mathrm{h}}$ (3.9) is in fact in the form $e^{i\Theta\sigma_3}\boldsymbol{\Psi}$, where the matrix $e^{i\Theta\sigma_3}$ has period $2\sqrt{2}\pi/\kappa_0$ that is incommensurate with the spatial period of seed spin.

As an alternative, one can analyse the rotation by constructing a triad, say Serret-Frenet triad through an identification $\hat{\mathbf{e}}_1 = \hat{\mathbf{S}}$, as discussed in Sec. 2.4. The rotation of the triad generates corresponding $\mathrm{SO}(3)$ group elements. An arbitrary fixed frame $\{\hat{\mathbf{i}}, \hat{\mathbf{j}}, \hat{\mathbf{k}}\}$ and the rotated frame $\{\hat{\mathbf{i}}', \hat{\mathbf{j}}', \hat{\mathbf{k}}'\}$ relates through nine direction cosines [51, p. 137]. These direction cosines are elements of the required rotation matrix. Then the axis angle representations of the rotation matrix is obtained via (4.40). Following the formalism detailed in Fig. 4.6, one get a closed curve in the parameter space of $\mathrm{SO}(3)$ as shown in Fig. 5.4 (b). There are '3' diametrical lines stacked together each indicating one a 2π rotation.

(a) $\boldsymbol{\Psi}_{\mathrm{h}} \in \mathrm{SU}(2)$ (b) Serret-Frenet triad
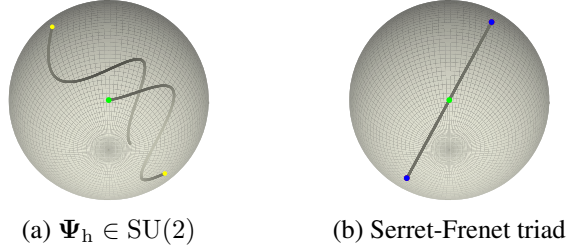
Figure 5.4: Spin field $\hat{\mathbf{S}}_{\mathrm{h}}$ in the group manifold. (a) Drawn from corresponding $\mathrm{SU}(2)$ element, which is not closed due to the non matching periods. (b) Invoking an identification, $\hat{\mathbf{e}}_1 = \hat{\mathbf{S}}$, Serret-Frenet triad is constructed and the corresponding rotation group is drawn.

5.4 Spatially periodic spin breather

One can arrive at "Akhmediev type breather" for the spin chain that reveals its spatial periodicity for a choice of

$$\lambda_{0R} = -\kappa_0/\sqrt{2}, \text{ and } \kappa_0^2 > \lambda_{0I}^2. \tag{5.7}$$

This corresponds to the Galilean transformed Akhmediev breather ψ_{GAB} (3.22), discussed previously in Sec. 3.4. We rewrite below the expression for "Akhmediev type breather":

$$\psi_{\mathrm{GAB}} = -\kappa_0 \, e^{i\sqrt{2}\kappa_0(x-x_0)} \, \frac{\cosh(rt - 2i\phi) - \cos\phi \, \cos(q(x - vt))}{\cosh(rt) - \cos\phi \, \cos(q(x - vt))}, \tag{5.8}$$

where, $q = 2\kappa_0 \sin(\phi)$, $r = 2\kappa_0^2 \sin(2\phi)$, $v = 2\sqrt{2}\kappa_0$, $\phi = \cos^{-1}(\lambda_{0I}/\kappa_0)$ and $x_0 = \pi/q$. Detailed steps are provided in section A.3 of Appendix A. It is clear that the above breather is localized in t and periodic in x.

As pointed out earlier, the spatial periodicity in the seed spin is, $L_1 = \sqrt{2}\pi/(\sqrt{3}\kappa_0)$. The breather solution has a spatial periodicity, $L_2 = 2\pi/q = \pi/\sqrt{\kappa_0^2 - \lambda_{0I}^2}$. Another spatial periodicity due to the background field $e^{i\sqrt{2}\kappa_0 x}$ does not reflect in the spin breather. So we have two kinds of periodicity,

$$L_1 = \sqrt{2}\pi/(\sqrt{3}\kappa_0), \text{ and } L_2 = \pi/\sqrt{\kappa_0^2 - \lambda_{0I}^2}. \tag{5.9}$$

In order to have a period matching in a finite spin chain of length L, we choose two integers n and m such that,

$$L = nL_1 = mL_2. \tag{5.10}$$

For a given value of κ_0, parameter λ_{0I} may be written as

$$\lambda_{0I} = \kappa_0 \sqrt{1 - \frac{3m^2}{2n^2}}. \tag{5.11}$$

A spatially periodic spin breather for $m = 2, n = 5$ is shown in Fig. 5.5. Equally spaced excitations can be seen in Fig. 5.5 (e) whereas these excitations eventually vanishes as $|t| \to \infty$, which then recreate the background field as shown in (a) and (i). One may compare this situation with that of breather profile (ψ_{GAB}) shown in Fig. 3.4 (b), where much before and after the breather excitation ($|t| \to \infty$) the profile seems quite similar — steady and smooth with no trace of 'breathing event' occurred in-between. This is not always true; some trace is left in the complex field ψ, not in its magnitude but in its phase [75]. We will explain this in detail a little later.

A close examination of Fig. 5.5 (a) and (i) clearly reveals an extra global rotation taken place in between initial and final stages of the spin chain that otherwise seem identical. The constant rotation in time, present in the background spin $\hat{\mathbf{S}}_{\mathrm{h}}$ has been cancelled out for the sake of analysis. Hence, we draw a conclusion that the additional rotation seen in the spin chain, say $\Delta\theta$, is solely due to the breather excitation.

5.5 FPUT recurrence in HF spin chain

Broadly speaking, a recurrence is when an initial state of the system is recovered either completely or as a close approximation to it. It can even be a repeated process. The phenomenon of recurrence is a fascinating concept in nonlinear dynamics which is now attributed to the integrable nature of the system [50]. First indication of the recurrence phenomena was in FPUT experiment (FPU in earlier literature [31]) which has been a paradox till the discovery of 'solitons'. Owing to the popularity of FPUT system — a discrete nonlinear lattice, recurrence behaviour in other systems are also termed as FPUT recurrence. In FPUT experiment the energy initially given to the first normal mode gradually transferred to other higher modes showing a hint of equipartition. Nonetheless, the process get reversed to reinforce the energy in the initial first mode — which is a recurrence. In the NLSE framework, especially in deep water or nonlinear optics, a similar process occurs wherein the energy in the carrier wave get shared with many of its side bands or spectral components. This happens with an increasing rate, during the initial stage of the nonlinear development of weakly modulated carrier wave. This is widely known as modulation instability (MI) or Benjamin-Feir instability [73, 26]. Nonlinear evolution of the wave trains
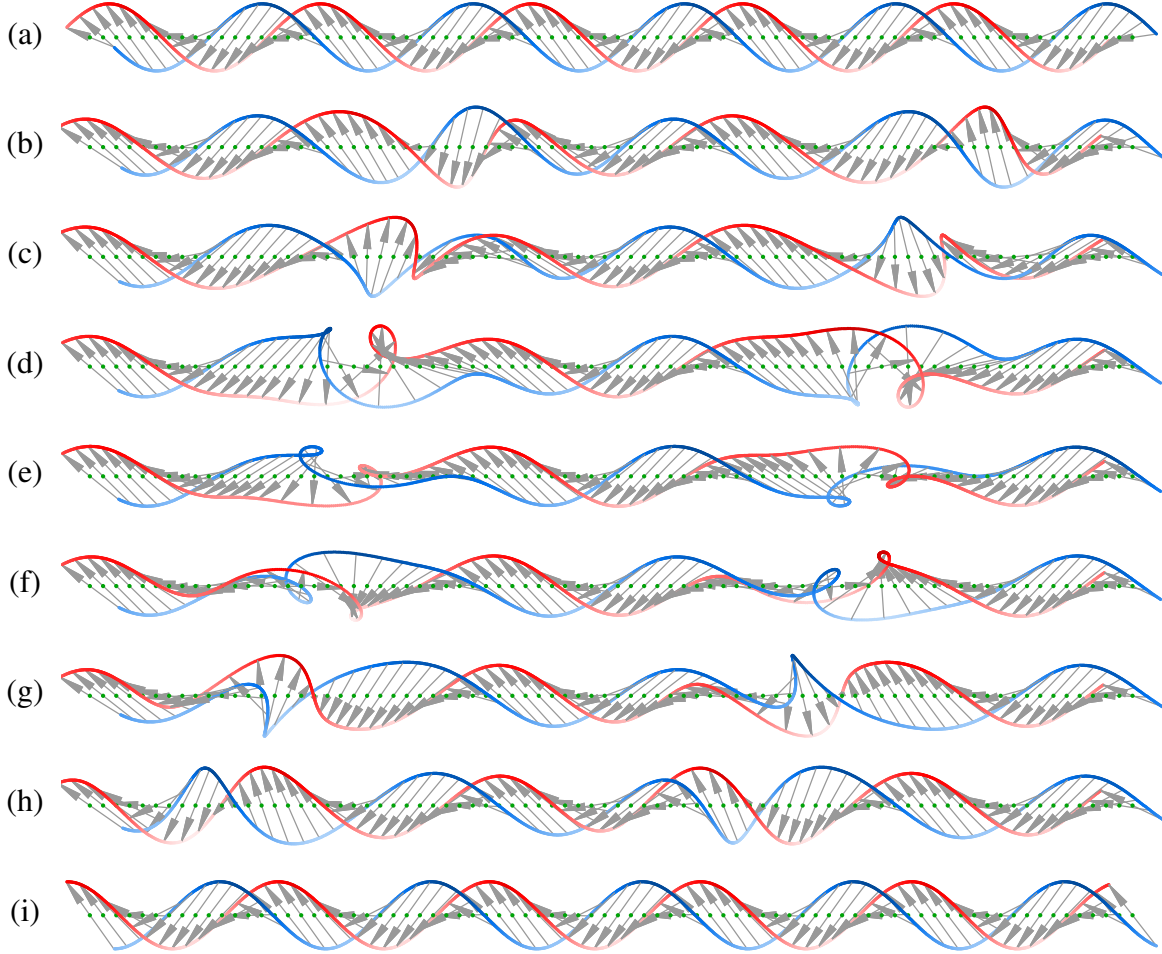
Figure 5.5: Spin breather $\hat{\mathbf{S}}_1$ (5.5) is shown in its time evolution. This is a spatially periodic case corresponds to ψ_{GAB} (3.22), obtained by choosing $\lambda_{0R} = -\kappa_0/\sqrt{2}$ and $\kappa_0^2 > \lambda_{0I}^2$. Specifically, $\kappa_0 = 1.0$ and $\lambda_{0R} = -0.7071$, $m = 2, n = 5$. Evolution of the spin chain begins from a uniform background, gradually develops localized excitations which are spaced periodically along the lattice, and eventually vanishes to get back the same uniform initial background. Uniform rotation (in time) present in the background $\hat{\mathbf{S}}_\mathrm{h}$ has been cancelled out for simplicity. However the spin chain undergoes an additional global rotation $\Delta\theta$, due to the breather excitation which is analogous to the phase shift arising in soliton – soliton interaction. In this particular case an interaction of the breather with its own background — a condensate (plane wave). For detailed animation, see the supplementary material: recurrence_hf.avi .

modeled by NLSE initially undergo modulation with energy spread over spectral components. However in the later stage carrier wave gradually regain all the energy, giving rise to the initial wave train. This modulation – demodulation process in the absence of dissipation is observed to be closely related with FPUT recurrence by Lake *et al.* [151], which is an earlier connection established in this regard both numerically and experimentally under certain circumstances. Continuous wave trains are exact solution of NLSE, which is the well known cnoidal wave expressed in terms of Jacobi elliptic function [109]. This is in fact a family of solutions. The one-soliton solution of secant hyperbolic shape — a limiting case of wave train, belongs to this family. The other extreme case is a harmonic plane wave which arises as a special case of the cnoidal wave [110]. Thus one can think of a wave train as solitonic lattice, whereas the harmonic plane wave resembles a condensate.

Propagation of a soliton over a solitonic lattice (wave train) leads to FPUT recurrence which can be explained on the basis of individual soliton-soliton interaction occurring in the system. The propagating soliton undergo a shift in position and phase during an elastic collision, but at the end of the story the lattice restore its initial state (upto a shift in position and phase) [152, 153].

Propagation of a breather (a special kind of soliton) over a condensate (plane wave) is described by the iconic solutions KMB, AB or PS where it is evident that the system returns to its initial state (with the same amplitude) giving rise to the FPUT recurrence. The condensate being a plane wave, does not have so called 'position', but it does have a phase. Therefore, FPUT recurrence in the condensate accompanied with a definite phase shift. This was proposed by Devine *et al.* [75] with a detailed study in the case of Akhmediev breather (AB). In their study, during the occurrence of AB the condensate (plane wave e^{it}) undergoes a phase shift which ranges from '0' to 2π, depending on the spatial periodicity of the breather. In the limiting case, PS is marked by a phase shift of 2π. Recently, phase evolution under Peregrine soliton has been experimentally observed in water wave and optical fibers [154].

In what follows, the phase shift observed in the condensate will be presented along with the additional rotation seen in the spin chain. Since there are two kinds of spatially periodic breather, namely ψ_{AB} and ψ_{GAB}, a qualitative difference observed between their gauge equivalent spin field will be pointed out. In the previous section we made a conjecture that the spin chain explicitly shows the change experienced by it during a 'breathing event' via the additional global rotation it picked up. This is evident from Fig. 5.5 (a) and (i). This extra rotation — call it as phase shift in the spin field, $\Delta\theta$ for convenience. This can be calculated by considering any two spin vectors at (x_0, t_0) and $(x_0, -t_0)$, where the constant

t_0 is relatively large to claim for $\pm t \to \infty$. Breather solution ψ_{GAB}, being a complex function reveals a shift it has undergone during a breathing event, via its phase factor, say $\varphi = \arg(\psi_{\mathrm{GAB}})$. Let the phase shift be $\Delta\varphi$, obtained from the difference in φ computed at t_0 and $-t_0$. Keeping κ_0 fixed (and fixed $\lambda_{0R} = -\kappa_0/\sqrt{2}$), both the phase shifts $\Delta\theta$ and $\Delta\varphi$ are calculated as a function of λ_{0I} which is shown in Fig. 5.6 (a). In the left limit, for $\lambda_{0I} \sim 0$, the breather excitation over the condensate vanishes — hence no phase shift. On the other hand, $\lambda_{0I} \sim \kappa_0$ leads to the rogue event, indicated by 2π shift. In between these two limits, both the quantities varies in a similar fashion. It is to be noted that for the spin chain, phase shift of 0 or 2π does not make any difference.

(a) Phase shift in ψ_{GAB}
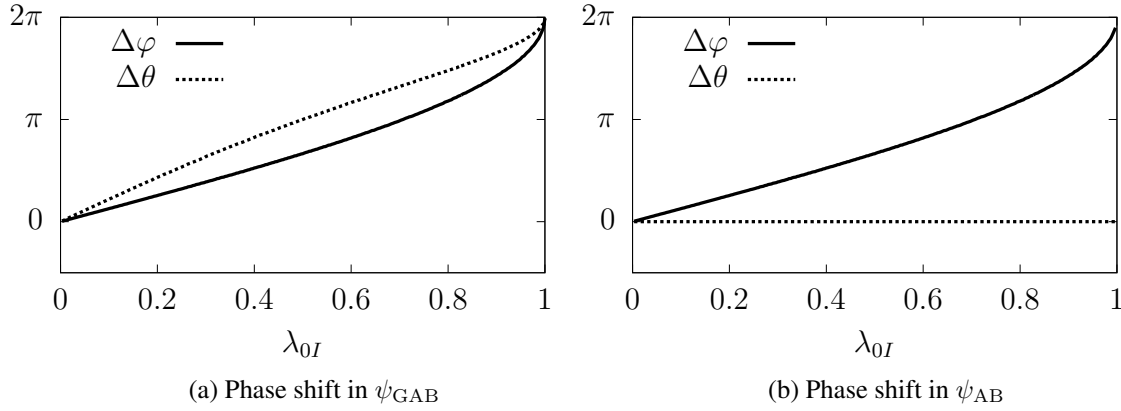
(b) Phase shift in ψ_{AB}

Figure 5.6: Phase shift $\Delta\varphi$ is the additional phase developed in the complex field ψ during a breathing event. Additional global rotation picked up by the spin chain is denoted as $\Delta\theta$. Phase shift versus λ_{0I} is shown for fixed $\kappa_0 (= 1)$. (a) Galilean transformed Akhmediev breather ψ_{GAB} and its spin counter part get phase shifted during a breather excitation. (b) Although Akhmediev breather ψ_{AB} shows a non zero phase shift, the corresponding spin chain does not show any additional global rotation during this breathing event. In both cases (a) and (b), $\lambda_{0I} \sim \kappa_0$ leads to the rogue event, marked by 2π phase shift in the complex field ψ_{GAB} and ψ_{AB}. Breather solution does not exist in the limit $\lambda_{0I} \sim 0$.

One may compare this result with that of Akhmediev breather ψ_{AB} (3.23), and its associated spin breather (4.25) with variables defined in (4.28). This is shown in Fig. 5.6 (b). Phase shift $\Delta\varphi$ in the plane wave background (condensate) ranges from '0' to 2π. Here, the plane wave is $\psi_c = \kappa_0\, e^{2i\kappa_0^2 t}$, with time dependent phase part. The phase is calculated at two different instances $\pm t_0 \to \infty$ where the time dependence of the phase part is unnecessary in the concerned problem. Therefore it is omitted to emphasise the contribution arising only from breather excitation [75]. It shows that, the additional global rotation $\Delta\theta$ picked up by the spin chain during the recurrence, is '0' for any λ_{0I}. It is quite obvious from Fig. 4.3, that the spin background is recovered exactly as before after a breathing event.

92

Although we discussed breather excitation in a finite spin chain (which is considered as a rogue in Sec. 4.5) for the convenience of explaining the 'belt trick', an extended spin chain does not alters the above observation.

There are instances in other areas of physics where an additional phase acquired by the system under a cyclic process has geometrical connections [155, 156]. In this particular context, the phase evolution experienced by the condensate can be viewed as a memory being possessed by the system regarding the breathing event it has underwent. Phase shift thus becomes the trace left after the recurrence. In the same footing, it is reasonable to consider the additional global rotation experienced by the spin chain during a recurrence, as the trace left in it. If so, spin field associated with Galilean transformed Akhmediev breather ψ_{GAB} leaves a trace, whereas the spin field associated with Akhmediev breather ψ_{AB} does not.

5.6 Conclusion

Spatially periodic spin configuration with individual spin vectors having constant rotation about a common axis constitute a solution to the 1-d LLE. Breather excitation over this dynamical spin background is studied by providing an explicit mathematical expression for the spin breather. In the most general case, evolution of the spin configuration is found to demonstrate the well known 'belt trick' wherein the number of rotation present in the spin chain between its boundaries changes by '2'. In Chapter 4 the 'belt trick' behaviour was also shown to exist in spin breather over the static spin background. Therefore a peculiar geometrical feature of this kind is seen to be associated with breather solutions in general.

A spatially periodic spin breather is studied in detail which is indeed the gauge equivalent of Galilean transformed Akhmediev breather. It is shown that the the spin chain undergoes an additional global rotation during the breather excitation. Additional global rotation experienced by this spin chain ranges from 0 to 2π, depending on the spatial periodicity of the breather. This additional rotation is closely related to the additional phase gained by the plane wave background during the same breathing event. Phase evolution of the plane wave solution in the context of Akhmediev breather is an established result emphasizing the 'trace' embedded in the system during an FPUT growth-decay cycle. Using the same analogy we draw a conclusion that the additional global rotation seen in the spin chain after an FPUT recurrence is the trace being left by the breathing event. At the same time, we observe that the spin chain which is gauge equivalent to the Akhmediev breather, does not experience any additional global rotation during the recurrence process.

In conclusion, there are two kinds of spin breathers — gauge equivalent to AB and gauge equivalent to Galilean transformed AB, which are qualitatively distinct by virtue of the closeness of FPUT recurrence. In the former, recurrence is exact in such a way that no measure can distinguish the initial and final state of the spin chain. The later, however picked up an additional global rotation that clearly distinguish the system before and after the FPUT recurrence.

Chapter 6

Conclusion and future problems

This thesis work is an exploration of the geometrical features of NLSE breather solutions, exploiting its close relationship with 1-d Heisenberg Ferromagnetic (HF) spin system and moving space curves. In a manner, we have visualized one of the remarkable properties of integrable systems — *recurrence*. A recurrence process can be exactly modelled by spatially periodic breather solutions to the NLSE (Akhmediev breather). In this framework a recurrence process receives certain unusual properties in contrast to a mere periodic process. One is that the recurrence takes place only once. Moreover, as time goes to infinity in both directions, the system asymptotically attains (nearly) identical states — a kind of settled state free of any fluctuations. The ruffling occurs only for a short duration of time. We have shown in this work, two kinds of spatially periodic breathers in the HF spin chain: one associated with the Akhmediev breather, and the other associated with a Galilean transformed Akhmediev breather. In the former, the recurrence is exact, in the sense that the initial and final configuration are indistinguishable. In the later, the spin chain has undergone an additional global rotation, which clearly distinguish the initial and final states of the spin chain. Our result shows that a one-to-one correspondence between HF model and the NLSE, seems missing in view of the recurrence phenomena.

During this investigation, we have encountered two intriguing topological features. One is a periodic *knot* formation in the associated space curves. Knotted space curves associated with breather solutions are a new feature so far not explored. Secondly, we observe a more interesting topological scenario during a breather excitation, that the spin chain demonstrates the *belt trick*. This is familiar trick using a belt or a ribbon, which easily explains the equivalence of 'two rotation' and 'no rotation'. In what follows is a brief discussion regarding the relevance of the findings and some future problems that naturally arise based on the results of this thesis.

1. Breather excitation in 1-d HF spin chain has been shown as a manifestation of the

well known 'belt trick', which is often used to demonstrate the trivialityof 4π rotation in $\mathbb{R}^3$. A finite spin chain initially having '2' complete turns in its spin configuration between its ends, as one moves along the lattice, continuously changes to a '0' turn state through a breather excitation, after which it eventually go back to its initial ('2' turn) configuration. If effects of damping are incorporated suitably, breather excitation may leads to $2 \rightarrow 0$ transition. Further, as pointed out, the minimum energy levels for the two states are clearly divided by a finite gap. The process of initiating such a breather excitation may have significant role in magnon based computing [157], since a spin chain with two such topologically distinguishable states provide a potential candidate for storing and manipulating binary data. Hence it would be of much practical interest to study the possible mechanism for breather excitation in 1-d HF spin chain. The primary quantity of interest is the total twist in the chain, experimental measurement of which holds the key to such a proposal. It is worth mentioning here that a local measurement of macro-magnetization is possible through methods such as optical techniques, antenna-based inductive techniques, Brillouin light scattering spectroscopy and spin pumping effect [157]. However, the interest in this case is in a global quantity, namely the total twist. On the experimental side measurement of such a quantity presents itself as a curious topic to be pursued, leading to greater possibilities in magnonic memory and computing.

2. We have presented a new class of breather solution to the NLSE, where the associated space curve is knotted. What is narrated in the space curve is the true essence of the solution which in fact cannot be revealed merely by looking at the complex soliton profile. A natural question arises — how and where does one witness this in a physical system? Although vortex filament motion is modelled using the equivalent LIA, as was pointed out, it fails to be a good model when long range effects are non-negotiable. Since NLSE is used to model a wide variety of physical systems, this special breather solution with its hidden periodic knotting – unknotting, does leave open the possibility of a physical observation, even if indirectly. For instance, can be optical soliton in a Kerr medium (described in NLSE) associated with a knotted breather be distinguished from one that is associated with an un-knotted breather? Can the phase of a Bose-Einstein condensate hold any additional information that relates to the knotted breather? How does one distinguish between the knotted and un-knotted breather state in a ferromagnetic spin chain? The multitude of systems that the NLSE is associated with, leaves a wide possibility for experimental realization of the knotted breather.

3. As a common characteristics of the breather excitation the final state of the system is more or less identical to the initial state, thus by providing the notion of FPUT recurrence.

However, under a space periodic breather excitation in the NLSE (Akhmediev Breather – AB), there exist a measurable quantity called phase shift that distinguish initial and final state of the complex field. Phase shift can be thought of as the 'trace' being left in the system after a recurrence process. The same description is also valid in the case of Galilean transformed AB. We have identified a similar quantity in spatially periodic spin breather — an additional global rotation picked up by the spin chain after a recurrence process which is analogous to the remnants of breather excitation. Spin breather corresponding to AB and Galilean transformed AB behaves qualitatively different in this regard, as the additional global rotation in the former is zero whereas in the later is non zero. Being gauge equivalent, both the systems NLSE and HF spin chain, must have some correlation in their dynamics which seems violated in the setting of this newly observed additional global rotation. This issue has to be addressed either by suggesting a reason behind this ambiguity or by identifying the proper counterpart for the phase shift in HF spin chain.

4. In order to obtain the knotted breather, we had started with a seed solution that corresponds to a helix (if one were to look at the associated space curve), and then using a Darboux transformation to obtain a breather mode. As was pointed out in section 3.4, this seed solution (helix) is Galilean equivalent to a seed associated with a circle. The well known Akhmediev breather is a spatially periodic case of the more general breather obtained from such a seed solution (circle) through Darboux transformation. We have shown that the spatially periodic case of the knotted breather is a Galilean equivalent to the Akhmediev breather. Therefore as a special case, we observe that, a Galilean transformation and Darboux transformation acting on a seed solution associated with a circle, at two different orders leads to the same breather solution. Although this is not explored in this thesis in detail, it is but natural to analyse this question on the commutativity of the two transformations in its generality.

5. Just as the classical continuous Heisenberg ferromagnet in one dimension is integrable, the quantum version of the problem is integrable through Bethe ansatz, and is an equally fundamental model in physics of quantum integrable systems. We noted that the solution space of the spin chain is effectively divided into two topological sectors characterized by the total twist. Further, we found that the minimum energy of the two sectors are separated by a finite gap. It would be interesting to look for its generalization to the quantum ferromagnet, and if a similar distinction can indeed be made in the state space of the quantum spin chain. Of particular interest will the look for a parallel in the energy lower bound of the two sectors, if indeed that is to be the case.

———

In the real world the dynamics of most of the systems are governed by nonlinear evolution equations. The study of nonlinear dynamics have two distinct regimes; chaos and the integrability. Integrable models are quite rare in nature, and are often approximations of rather complicated system dynamics. However ideal they seem integrable systems are of special interest owing to their exact analytical solutions.

Geometry is omnipresent in nature. Abstract things are often demonstrated geometrically in a simple and elegant manner. This thesis has studied some of the geometrical features of the NLSE breather solutions. Some peculiar geometrical features such as, *belt trick* and *knots*, show up unexpectedly during our studies, which give enough space for further investigations. What is more interesting is that the systems under investigation are simple mathematical models. They are ideal systems, that too in one dimension, they nevertheless show that geometry can play a significant role even in low dimensional systems.

$\star\,\star\,\star$

Bibliography

[1] S. STROGATZ, *Nonlinear Dynamics And Chaos*, Levant Books, Kolkata, 2007.

[2] R. M. MAY, Simple mathematical models with very complicated dynamics, *Nature* **261**: 459–467 (1976).

[3] P. S. ADDISON, *Fractals and Chaos: An Illustrated Course*, Institute of Physics Publishing, Bristol and Philadelphia, 1997.

[4] G. BOEING, Visual analysis of nonlinear dynamical systems: Chaos, fractals, self-similarity and the limits of prediction, *Systems* **4**: (4) 37 (2016).

[5] E. A. JACKSON, *Perspectives of Nonlinear Dynamics*, vol. 2, Cambridge University Press, 1990.

[6] E. FERMI, P. PASTA, S. ULAM, and M. TSINGOU, Studies of the nonlinear problems I, *Los Alamos Scientific Laboratory* (1955).

[7] J. FORD, The Fermi-Pasta-Ulam problem: Paradox turns discovery, *Physics Reports* **213**: 271–310 (1992).

[8] V. ZAKHAROV and L. OSTROVSKY, Modulation instability: The beginning, *Physica D: Nonlinear Phenomena* **238**: 540–548 (2009).

[9] N. N. AKHMEDIEV and V. I. KORNEEV, Modulation instability and periodic solutions of the nonlinear Schrödinger equation, *Theor. Math. Phys.* **69**: 1089–1093 (1986).

[10] N. N. AKHMEDIEV, *Déjà vu* in optics, *Nature* **413**: 267–268 (2001).

[11] K. B. DYSTHE and K. TRULSEN, Note on breather type solutions of the NLS as models for freak-waves, *Physica Scripta* **1999**: 48 (1999).

[12] A. SYM, Soliton surfaces, *Lettere al Nuovo Cimento (1971-1985)* **33**: 394–400 (1982).

[13] R. L. RICCA, The contributions of Da Rios and Levi-Civita to asymptotic potential theory and vortex filament dynamics, *Fluid Dynamics Research* **18**: 245–268 (1996).

[14] S. MURUGESH and M. LAKSHMANAN, Nonlinear dynamics of moving curves and surfaces: Applications to physical systems, *International Journal of Bifurcation and Chaos* **15**: 51–63 (2005).

[15] J. CIEŚLIŃSKI, P. K. H. GRAGERT, and A. SYM, Exact solution to Localized-Induction-Approximation equation modeling smoke ring motion, *Phys. Rev. Lett.* **57**: 1507–1510 (1986).

[16] M. LAKSHMANAN, Continuum spin system as an exactly solvable dynamical system, *Phys. Lett. A* **61**: 53–54 (1977).

[17] J. H. VAN VLECK, *Theory of Electric and Magnetic Susceptibilities*, Oxford, Clarendon Press, 1932.

[18] C. KITTEL, *Introduction to Solid State Physics*, 7th ed., Wiley, 1996.

[19] V. E. ZAKHAROV and L. A. TAKHTADZHYAN, Equivalence of the nonlinear Schrödinger equation and the equation of a Heisenberg ferromagnet, *Theor. Math. Phys.* **38**: 17–23 (1979).

[20] N. AKHMEDIEV, A. ANKIEWICZ, and M. TAKI, Waves that appear from nowhere and disappear without a trace, *Physics Letters A* **373**: 675 – 678 (2009).

[21] P. MÜLLER, C. GARRETT, and A. OSBORNE, Rogue waves – The fourteenth 'Aha Huliko'a Hawaiian Winter Workshop, *Oceanography* **18**: 66–75 (2005).

[22] S. HAVER, A possible freak wave measured at the Draupner Jacket January 1 1995, *Proc. Rogue waves* (2004), pp. 1–8.

[23] B. KIBLER, J. FATOME, C. FINOT, G. MILLOT, F. DIAS, G. GENTY, N. AKHMEDIEV, and J. M. DUDLEY, The Peregrine soliton in nonlinear fibre optics, *Nature Physics* **6**: 790–795 (2010).

[24] Y. Tsai, J. Tsai, and I. Lin, Generation of acoustic rogue waves in dusty plasmas through three-dimensional particle focusing by distorted waveforms, *Nature Physics* **12**: 573 (2016).

[25] Y. V. Bludov, V. V. Konotop, and N. Akhmediev, Matter rogue waves, *Phys. Rev. A* **80**: 033610 (2009).

[26] H. C. Yuen and B. M. Lake, Nonlinear dynamics of deep-water gravity waves, *Advances in Applied Mechanics* **22**: 67–229 (1982).

[27] A. Hasegawa, *Optical Solitons in Fibers*, 2nd ed., Springer Berlin Heidelberg, 1990.

[28] W. Bao, The nonlinear Schrödinger equation and applications in Bose-Einstein condensation and plasma physics, Dynamics in Models of Coarsening, Coagulation, Condensation and Quantization, (Editors) W. Bao and J. Liu, World Scientific, 2007, pp. 141–239.

[29] H. Salman, Breathers on quantized superfluid vortices, *Phys. Rev. Lett.* **111**: 165301 (2013).

[30] V. E. Zakharov and A. B. Shabat, Exact theory of two-dimensional self-focusing and one-dimensional self-modulation of waves in nonlinear media, *Soviet Phys. JETP* **34**: 62 (1972).

[31] T. Dauxois, Fermi, Pasta, Ulam, and a mysterious lady, *Phys. Today* **61**: 55 (2008).

[32] M. Lakshmanan, The fascinating world of the Landau-Lifshitz-Gilbert equation: an overview, *Philos. Trans. Royal Soc. A* **369**: 1280–1300 (2011).

[33] L. Takhtajan, Integration of the continuous Heisenberg spin chain through the inverse scattering method, *Physics Letters A* **64**: 235–237 (1977).

[34] M. Lakshmanan, T. Ruijgrok, and C. Thompson, On the dynamics of a continuum spin system, *Physica A* **84**: 577–590 (1976).

[35] J. Tjon and J. Wright, Solitons in the continuous Heisenberg spin chain, *Phys. Rev. B* **15**: 3470–3476 (1977).

[36] R. L. Ricca, Rediscovery of Da Rios equations, *Nature* **352**: 561–562 (1991).

[37] H. HASIMOTO, A soliton on a vortex filament, *J. Fluid Mech.* **51**: 477–485 (1972).

[38] A. ANDERSEN, T. BOHR, B. STENUM, J. J. RASMUSSEN, and B. LAUTRUP, Anatomy of a bathtub vortex, *Phys. Rev. Lett.* **91**: 104502 (2003).

[39] E. HUGGINS, Smoke ring physics, *The Physics Teacher* **49**: 488–491 (2011).

[40] S. V. ALEKSEENKO, P. A. KUIBIN, V. L. OKULOV, and S. I. SHTORK, Helical vortices in swirl flow, *Journal of Fluid Mechanics* **382**: 195–243 (1999).

[41] E. J. HOPFINGER, F. K. BROWAND, and Y. GAGNE, Turbulence and waves in a rotating tank, *Journal of Fluid Mechanics* **125**: 505–534 (1982).

[42] H. AREF and E. P. FLINCHEM, Dynamics of a vortex filament in a shear flow, *Journal of Fluid Mechanics* **148**: 477–497 (1984).

[43] G. L. LAMB, Solitons and the motion of helical curves, *Phys. Rev. Lett.* **37**: 235–237 (1976).

[44] A. SYM, Soliton surfaces II – Geometric unification of solvable nonlinearities, *Lettere al Nuovo Cimento (1971-1985)* **36**: 307–312 (1983).

[45] A. SYM, Soliton surfaces and their applications (soliton geometry from spectral problems), Geometric aspects of the Einstein equations and integrable systems, (Editor) R. MARTINI, Springer Berlin Heidelberg, 1985 pp. 154–231.

[46] D. LEVI, A. SYM, and S. WOJCIECHOWSKI, N-Solitons on a vortex filament, *Physics Letters A* **94**: 408–411 (1983).

[47] M. A. PORTER, N. J. ZABUSKY, BAMBI HU, and D. K. CAMPBELL, Fermi, Pasta, Ulam and the birth of experimental mathematics, *American Scientist* **97**: 214–221 (2009).

[48] M. ONORATO, L. VOZELLA, D. PROMENT, and Y. V. LVOV, Route to thermalization in the α- Fermi-Pasta-Ulam system, *Proceedings of the National Academy of Sciences* **112**: 4208–4213 (2015).

[49] A. CARATI, L. GALGANI, A. MAIOCCHI, F. GANGEMI, and R. GANGEMI, The FPU problem as a statistical-mechanical counterpart of the KAM problem, and its relevance for the foundations of physics, *Regular and Chaotic Dynamics* **23**: 704–719 (2018).

[50] D. PIERANGELI, M. FLAMMINI, L. ZHANG, G. MARCUCCI, A. J. AGRANAT, P. G. GRINEVICH, P. M. SANTINI, C. CONTI, and E. DELRE, Observation of Fermi-Pasta-Ulam-Tsingou recurrence and its exact dynamics, *Phys. Rev. X* **8**: 041017 (2018).

[51] H. GOLDSTEIN, *Classical Mechanics*, 3rd ed., Addison-Wesley Press, 1950.

[52] G. BENETTIN, A. CARATI, L. GALGANI, and A. GIORGILLI, The Fermi-Pasta-Ulam problem and the metastability perspective, The Fermi-Pasta-Ulam Problem: A Status Report, (Editor) G. GALLAVOTTI, Springer Berlin Heidelberg, 2008, pp. 151–189.

[53] J. MOSER, *Stable and Random Motions in Dynamical Systems: With Special Emphasis on Celestial Mechanics (AM-77)*, Revised ed., Princeton University Press, 1973.

[54] E. WHITTAKER, *A Treatise on the Analytical Dynamics of Particles and Rigid Bodies: With an Introduction to the Problem of Three Bodies*, 4th ed., Dover Publications, 1944.

[55] M. TABOR, *Chaos and integrability in nonlinear dynamics: an introduction*, Wiley, 1989.

[56] M. FALCIONI and A. VULPIANI, Enrico Fermis's contribution to non-linear systems: The influence of an unpublished article, Enrico Fermi: His Work and Legacy, (Editors) C. BERNARDINI and L. BONOLIS, Springer Berlin Heidelberg, 2004, pp. 271–285.

[57] E. FERMI, *Collected Papers:(Note E Memorie)*, vol. 2, University of Chicago Press, 1965.

[58] N. J. ZABUSKY, A synergetic approach to problems of nonlinear dispersive wave propagation and interaction, Nonlinear Partial Differential Equations, (Editor) W. F. AMES, Academic Press, 1967, pp. 223–258.

[59] J. TUCK and M. MENZEL, The superperiod of the nonlinear weighted string (FPU) problem, *Advances in Mathematics* **9**: 399–407 (1972).

[60] A. CARATI, L. GALGANI, and A. GIORGILLI, The Fermi-Pasta-Ulam problem as a challenge for the foundations of physics, *Chaos* **15**: 015105 (2005).

[61] G. P. BERMAN and F. M. IZRAILEV, The Fermi-Pasta-Ulam problem: Fifty years of progress, *Chaos* **15**: 015104 (2005).

[62] D. K. CAMPBELL, P. ROSENAU, and G. M. ZASLAVSKY, Introduction: The Fermi-Pasta-Ulam problem – The first fifty years, *Chaos* **15**: 015101 (2005).

[63] G. M. ZASLAVSKY, Long way from the FPU-problem to chaos, *Chaos* **15**: 015103 (2005).

[64] N. J. ZABUSKY, Exact solution for the vibrations of a nonlinear continuous model string, *Journal of Mathematical Physics* **3**: 1028–1039 (1962).

[65] M. D. KRUSKAL and N. J. ZABUSKY, Stroboscopic-perturbation procedure for treating a class of nonlinear wave equations, *J. Math. Phys.* **5**: 231–244 (1964).

[66] M. TODA, Wave propagation in anharmonic lattices, *J. Phys. Soc. JPN* **23**: 501–506 (1967).

[67] D. J. KORTEWEG and G. DE VRIES, On the change of form of long waves advancing in a rectangular canal, and on a new type of long stationary waves, *Philosophical Magazine and Journal of Science* **39**: 422–443 (1895).

[68] C. GARDNER and G. MORIKAWA, *Similarity in the asymptotic behaviour of collision-free hydromagnetic waves and water waves*, vol. 18, Courant Institute, New York University, Rep. NYO 9082, 1960.

[69] P. G. DRAZIN, *Solitons*, London Mathematical Society Lecture Note Series (85), Cambridge University Press, 1983.

[70] N. J. ZABUSKY and M. D. KRUSKAL, Interaction of "solitons" in a collisionless plasma and the recurrence of initial states, *Phys. Rev. Lett.* **15**: 240–243 (1965).

[71] A. C. NEWELL, *Solitons in mathematics and physics*, Society for Industrial and Applied Mathematics Philadelphia, Pa, 1985.

[72] C. S. GARDNER, J. M. GREENE, M. D. KRUSKAL, and R. M. MIURA, Method for solving the Korteweg-deVries equation, *Phys. Rev. Lett.* **19**: 1095–1097 (1967).

[73] T. B. BENJAMIN and J. E. FEIR, The disintegration of wave trains on deep water Part 1. Theory, *Journal of Fluid Mechanics* **27**: 417–430 (1967).

[74] G. VAN SIMAEYS, P. EMPLIT, and M. HAELTERMAN, Experimental demonstration of the Fermi-Pasta-Ulam recurrence in a modulationally unstable optical wave, *Phys. Rev. Lett.* **87**: 033902 (2001).

[75] N. DEVINE, A. ANKIEWICZ, G. GENTY, J. DUDLEY, and N. AKHMEDIEV, Recurrence phase shift in Fermi-Pasta-Ulam nonlinear dynamics, *Physics Letters A* **375**: 4158–4161 (2011).

[76] K. HAMMANI, B. WETZEL, B. KIBLER, J. FATOME, C. FINOT, G. MILLOT, N. AKHMEDIEV, and J. M. DUDLEY, Spectral dynamics of modulation instability described using Akhmediev breather theory, *Opt. Lett.* **36**: 2140–2142 (2011).

[77] P. D. LAX, Integrals of nonlinear equations of evolution and solitary waves, *Communications on Pure and Applied Mathematics* **21**: 467–490 (1968).

[78] M. J. ABLOWITZ, D. J. KAUP, A. C. NEWELL, and H. SEGUR, The inverse scattering transform - fourier analysis for nonlinear problems, *Studies in Applied Mathematics* **53**: 249–315 (1974).

[79] L. D. FADDEEV and L. A. TAKHTAJAN, *Hamiltonian Methods in the Theory of Solitons*, Springer Berlin, 1987.

[80] C. ROGERS and W. K. SCHIEF, *Bäcklund and Darboux Transformations: Geometry and Modern Applications in Soliton Theory*, Cambridge University Press, 2002.

[81] CHAOHAO GU, HESHENG HU, and ZIXIANG ZHOU, *Darboux Transformations in Integrable Systems: Theory and Their Applications to Geometry*, Springer, 2005.

[82] E. CHARLES P, Heisenberg's applications of quantum mechanics (1926-33): or the settling of the new land, *Helvetica Physica Acta* **56**: 993–1001 (1983).

[83] J. H. VAN VLECK, A survey of the theory of ferromagnetism, *Rev. Mod. Phys.* **17**: 27–47 (1945).

[84] N. W. ASHCROFT and N. D. MERMIN, *Solid state physics*, 1st ed., Holt, Rinehart and Winston, 1976.

[85] H. E. STANLEY, Dependence of critical properties on dimensionality of spins, *Phys. Rev. Lett.* **20**: 589–592 (1968).

[86] H. W. BLÖTE and B. NIENHUIS, The phase diagram of the O(n) model, *Physica A* **160**: 121–134 (1989).

[87] L. D. LANDAU and E. LIFSHITZ, On the theory of the dispersion of magnetic permeability in ferromagnetic bodies, *Phys. Z. Sowjet.* **8**: 153–164 (1935).

[88] C. HERRING and C. KITTEL, On the theory of spin waves in ferromagnetic media, *Phys. Rev.* **81**: 869–880 (1951).

[89] D. J. STRUIK, *Lectures on Classical Differential Geometry*, 2nd ed., Dover Publications, 1988.

[90] J. STOKER, *Differential Geometry*, *Pure and applied mathematics* Wiley, 1989.

[91] M. LAKSHMANAN, On the geometrical interpretation of solitons, *Physics Letters A* **64**: 354–356 (1978).

[92] M. LAKSHMANAN and K. M. TAMIZHMANI, Motion of strings, embedding problem and soliton equations, *Applied Scientific Research* **37**: 127–143 (1981).

[93] R. J. ARMS and F. R. HAMA, Localized-induction concept on a curved vortex and motion of an elliptic vortex ring, *The Physics of Fluids* **8**: 553–559 (1965).

[94] R. BETCHOV, On the curvature and torsion of an isolated vortex filament, *Journal of Fluid Mechanics* **22**: 471–479 (1965).

[95] G. L. LAMB, Solitons on moving space curves, *Journal of Mathematical Physics* **18**: 1654–1661 (1977).

[96] J. CIEŚLIŃSKI, The Darboux-Bianchi-Bäcklund transformation and soliton surfaces, Nonlinearity and Geometry, (Editors) D. WÓJCIK and J. CIEŚLIŃSKI, Polish Scientific Publishers, Warsaw, 1998 pp. 81–107. Preprint arXiv:1303.5472.

[97] G. DARBOUX, Sur une proposition relative aux equations lineaires (On a proposition relative to linear equations), *Comptes Rendus Acad. Sci.* **94**: 1456–1459 (1882).

[98] V. B. MATVEEV, Darboux transformation and explicit solutions of the Kadomtcev-Petviaschvily equation, depending on functional parameters, *Letters in Mathematical Physics* **3**: 213–216 (1979).

[99] V. MATVEEV and M. SALLE, *Darboux Transformations and Solitons*, Springer-Verlag, 1991.

[100] R. M. MIURA, Korteweg-de Vries equation and generalizations. I. A remarkable explicit nonlinear transformation, *J. Math. Phys.* **9**: 1202–1204 (1968).

[101] G. NEUGEBAUER and R. MEINEL, General N-soliton solution of the AKNS class on arbitrary background, *Physics Letters A* **100**: 467–470 (1984).

[102] E. A. KUZNETSOV, Solitons in a parametrically unstable plasma, *Akademiia Nauk SSSR Doklady* **236**: 575–577 (1977).

[103] MA YAN CHOW, The perturbed plane-wave solutions of the cubic Schrödinger equation, *Stud. Appl. Math.* **60**: 43–58 (1979).

[104] D. H. PEREGRINE, Water waves, nonlinear Schrödinger equations and their solutions, *J. Austral. Math. Soc. Ser. B* **25**: 16–43 (1983).

[105] K. KONNO, M. MITUHASHI, and Y. H. ICHIKAWA, Soliton on thin vortex filament, *Chaos, Solitons & Fractals* **1**: 55–65 (1991).

[106] S. KIDA, A vortex filament moving without change of form, *Journal of Fluid Mechanics* **112**: 397–409 (1981).

[107] A. DOLIWA and A. SYM, On Kida class of vortex filament motions, Symmetries in Science III, (Editors) B. GRUBER and F. IACHELLO, Springer, Boston, MA, 1989 pp. 389–398.

[108] H. HASIMOTO, Motion of a vortex filament and its relation to elastica, *Journal of the Physical Society of Japan* **31**: 293–294 (1971).

[109] J. MERTSCHING, Quasiperiodic solutions of the nonlinear Schrödinger equation, *Fortschritte der Physik* **35**: 519–536 (1987).

[110] A. SYM, Vortex filament motion in terms of Jacobi theta functions, *Fluid Dynamics Research* **3**: 151–156 (1988).

[111] R. L. RICCA, D. C. SAMUELS, and C. F. BARENGHI, Evolution of vortex knots, *Journal of Fluid Mechanics* **391**: 29–44 (1999).

[112] A. CALINI and T. IVEY, Stability of small-amplitude torus knot solutions of the localized induction approximation, *J. Phys. A: Math. Theor.* **44**: 335204 (2011).

[113] R. L. RICCA, Torus knots and polynomial invariants for a class of soliton equations, *Chaos* **3**: 83–91 (1993). (Erratum) R. L. RICCA, *Chaos* **5**: 346 (1995).

[114] N. AKHMEDIEV, J. SOTO-CRESPO, and A. ANKIEWICZ, Extreme waves that appear from nowhere: On the nature of rogue waves, *Physics Letters A* **373**: 2137–2145 (2009).

[115] H. SALMAN, Multiple breathers on a vortex filament, *Journal of Physics: Conference Series* **544**: 012005 (2014).

[116] J. HASS, J. C. LAGARIAS, and N. PIPPENGER, The computational complexity of knot and link problems, *Journal of the ACM (JACM)* **46**: 185–211 (1999).

[117] P. G. SAFFMAN, *Vortex Dynamics*, Cambridge University Press, 1993.

[118] S. ALEKSEENKO, P. KUIBIN, and V. OKULOV, *Theory of Concentrated Vortices: An Introduction*, Springer Berlin Heidelberg, 2007.

[119] J. C. HARDIN, The velocity field induced by a helical vortex filament, *The Physics of Fluids* **25**: 1949–1952 (1982).

[120] R. L. RICCA, The effect of torsion on the motion of a helical vortex filament, *Journal of Fluid Mechanics* **273**: 241–259 (1994).

[121] E. B. SONIN, Dynamics of helical vortices and helical-vortex rings, *EPL (Europhysics Letters)* **97**: 46002 (2012).

[122] S. V. ALEKSEENKO, P. A. KUIBIN, S. I. SHTORK, S. G. SKRIPKIN, and M. A. TSOY, Vortex reconnection in a swirling flow, *JETP Letters* **103**: 455–459 (2016).

[123] M. A. TSOY, S. G. SKRIPKIN, P. A. KUIBIN, S. I. SHTORK, and S. V. ALEKSEENKO, Kelvin waves on helical vortex tube in swirling flow, *Journal of Physics: Conference Series* **980**: 012003 (2018).

[124] D. KLECKNER and W. T. M. IRVINE, Creation and dynamics of knotted vortices, *Nature Physics* **9**: 253–258 (2013).

[125] YAN ZHANG, XIAN-JIA NIE, and QI-LAO ZHA, Rogue wave solutions for the Heisenberg ferromagnet equations, *Chinese Physics Letters* **31**: 060201 (2014).

[126] L. ZAI-DONG, L. QIU-YAN, X. TIAN-FU, and H. PENG-BIN, Breathers and rogue waves excited by all-magnonic spin-transfer torque, *Phys. Rev. E* **94**: 042220 (2016).

[127] A. K. MUKHOPADHYAY, V. M. VYAS, and P. K. PANIGRAHI, Rogue waves and breathers in Heisenberg spin chain, *The European Physical Journal B* **88**: 188 (2015).

[128] R. L. RICCA and B. NIPOTI, Gauss' linking number revisited, *Journal of Knot Theory and Its Ramifications* **20**: 1325–1343 (2011).

[129] F. H. CRICK, Linking numbers and nucleosomes, *Proc. Natl. Acad. Sci. USA* **73**: 2639–2643 (1976).

[130] M. A. BERGER and C. PRIOR, The writhe of open and closed curves, *Journal of Physics A: Mathematical and General* **39**: 8321 (2006).

[131] G. CĂLUGĂREANU, L'intégrale de Gauss et l'analyse des nœuds tridimensionnels, *Rev. Math. pures appl* **4** (1959), no. 5.

[132] J. H. WHITE, Self-linking and the Gauss integral in higher dimensions, *Am. J. Math.* **91**: 693–728 (1969).

[133] F. B. FULLER, The writhing number of a space curve, *Proc. Natl. Acad. Sci. USA* **68**: 815–819 (1971).

[134] F. B. FULLER, Decomposition of the linking number of a closed ribbon: A problem from molecular biology, *Proc. Natl. Acad. Sci. USA* **75**: 3557–3561 (1978).

[135] G. COSTA and G. FOGLI, *Symmetries and Group Theory in Particle Physics: An Introduction to Space-Time and Internal Symmetries*, 1 ed., Springer-Verlag Berlin Heidelberg, 2012.

[136] E. VAN BEVEREN, Some notes on group theory (2012). Universidade de Coimbra. URL http://cft.fis.uc.pt/eef/evbgroups.pdf.

[137] W. ROSSMANN, *Lie Groups: An Introduction Through Linear Groups*, Oxford University Press, 2002.

[138] B. C. HALL, *Lie Groups, Lie Algebras, and Representations: An Elementary Introduction*, Springer New York, 2003.

[139] WU-KI TUNG, *Group Theory in Physics*, World Scientific Publishing, 1985.

[140] J. SAMUEL, Mirrors and merry-go-rounds, *Resonance* **15**: 711–722 (2010).

[141] M. STALEY, Understanding quaternions and the Dirac belt trick, *European Journal of Physics* **31**: 467–478 (2010).

[142] J. J. SAKURAI, *Modern Quantum Mechanics*, Revised ed., Addison-Wesley, 1994.

[143] J. GALLIER, Basics of classical lie groups: The exponential map, lie groups, and lie algebras, Geometric Methods and Applications: For Computer Science and Engineering, Springer New York, 2001, pp. 367–414.

[144] A. M. STEANE, An introduction to spinors, *preprint arXiv:1312.3824* (2013).

[145] G. CODDENS, Spinors for everyone (2017). URL `https://hal-cea.archives-ouvertes.fr/cea-01572342`.

[146] R. D. KAMIEN, The geometry of soft materials: a primer, *Rev. Mod. Phys.* **74**: 953–971 (2002).

[147] W. FENCHEL, Über krümmung und windung geschlossener raumkurven, *Mathematische Annalen* **101**: 238–252 (1929).

[148] W. FENCHEL, On the differential geometry of closed space curves, *Bull. Amer. Math. Soc.* **57**: 44–54 (1951).

[149] R. DANDOLOFF, New topological configurations in the continuous Heisenberg spin chain: Lower bound for the energy, *Adv. Condens. Matter Phys.* **2015**: 1–3 (2015).

[150] T. L. GILBERT, A phenomenological theory of damping in ferromagnetic materials, *IEEE Transactions on Magnetics* **40**: 3443–3449 (2004).

[151] B. M. LAKE, H. C. YUEN, H. RUNGALDIER, and W. E. FERGUSON, Nonlinear deep-water waves: theory and experiment. Part 2. Evolution of a continuous wave train, *Journal of Fluid Mechanics* **83**: 49–74 (1977).

[152] E. A. KUZNETSOV, Fermi-Pasta-Ulam recurrence and modulation instability, *JETP Letters* **105**: 125–129 (2017).

[153] H. J. SHIN, Soliton scattering from a finite cnoidal wave train in a fiber, *Phys. Rev. E* **63**: 026606 (2001).

[154] X. GANG, K. HAMMANI, A. CHABCHOUB, J. M. DUDLEY, B. KIBLER, and C. FINOT, Phase evolution of Peregrine-like breathers in optics and hydrodynamics, *Phys. Rev. E* **99**: 012207 (2019).

[155] M. V. BERRY, Quantal phase factors accompanying adiabatic changes, *Proceedings of the Royal Society of London. A. Mathematical and Physical Sciences* **392**: 45–57 (1984).

[156] M. KUGLER and S. SHTRIKMAN, Berry's phase, locally inertial frames, and classical analogues, *Phys. Rev. D* **37**: 934–937 (1988).

[157] A. V. CHUMAK, V. I. VASYUCHKA, A. A. SERGA, and B. HILLEBRANDS, Magnon spintronics, *Nat. Phys.* **11**: 453–461 (2015).

Appendix A

NLS Helix: Darboux transformation and breather solutions

We choose an informal name "NLS Helix" to label the broad class of solutions and expressions that are associated with seed solution, $\psi_{\mathrm{h}} = \kappa_0 e^{i\sqrt{2}\,\kappa_0 x}$, for which the associated space curve is a helix. In this chapter, we provide mathematical steps for the DT technique.

A.1   NLSE and the Lax pair

The nonlinear Schrödinger equation (NLSE)

$$i\psi_t + \psi_{xx} + 2|\psi|^2\psi = 0, \tag{A.1}$$

arises as the compatibility condition for the linear system, also known as Lax pair

$$\mathbf{\Psi}_x = U\mathbf{\Psi}, \quad \mathbf{\Psi}_t = V\mathbf{\Psi}, \tag{A.2}$$

where the connections U and V are in general functions of x, t and spectral parameter λ. For convenience one can treat them as functions of ψ and its derivatives, as given below:

$$U(\psi) = \begin{pmatrix} 0 & \psi \\ -\overline{\psi} & 0 \end{pmatrix} + \lambda \begin{pmatrix} -i & 0 \\ 0 & i \end{pmatrix}, \tag{A.3}$$

$$V(\psi) = \begin{pmatrix} i|\psi|^2 & i\,\psi_x \\ i\,\overline{\psi}_x & -i|\psi|^2 \end{pmatrix} + \lambda \begin{pmatrix} 0 & 2\psi \\ -2\overline{\psi} & 0 \end{pmatrix} + \lambda^2 \begin{pmatrix} -2i & 0 \\ 0 & 2i \end{pmatrix}. \tag{A.4}$$

A.2 Darboux transformation

Each solution to the NLSE (A.1) corresponds to a matrix solution to the Lax pair (A.2). We employ Darboux transformation detailed in section 2.6.2, to obtain a new breather solution — knotted breather, by starting from a seed solution

$$\psi_{\mathrm{h}} = \kappa_0 e^{i\sqrt{2}\,\kappa_0 x}, \tag{A.5}$$

for a real constant κ_0.

A.2.1 Seed solution and related functions

Seed solution ψ_{h} corresponds to a matrix solution $\boldsymbol{\Psi}_{\mathrm{h}}(x, t, \lambda)$ to the below Lax pair

$$
\begin{aligned}
\boldsymbol{\Psi}_{\mathrm{h},x} &= U_{\mathrm{h}}\boldsymbol{\Psi}_{\mathrm{h}}, \\
\boldsymbol{\Psi}_{\mathrm{h},t} &= V_{\mathrm{h}}\boldsymbol{\Psi}_{\mathrm{h}},
\end{aligned} \tag{A.6}
$$

where $U_{\mathrm{h}} = U(\psi_{\mathrm{h}})$, and $V_{\mathrm{h}} = V(\psi_{\mathrm{h}})$. We explicitly write the matrix solution $\boldsymbol{\Psi}_{\mathrm{h}}$ in the form,

$$\boldsymbol{\Psi}_{\mathrm{h}}(x, t, \lambda) = \frac{1}{\sqrt{d}} \begin{pmatrix} \varphi_1 & -\overline{\varphi_2} \\ \varphi_2 & \overline{\varphi_1} \end{pmatrix}, \tag{A.7}$$

where,

$$
\begin{aligned}
\varphi_1 &= \left(a\, e^{i\Omega/2} + b\, e^{-i\Omega/2}\right) e^{i\frac{1}{\sqrt{2}}\kappa_0 x}, \\
\varphi_2 &= -\left(b\, e^{i\Omega/2} + a\, e^{-i\Omega/2}\right) e^{-i\frac{1}{\sqrt{2}}\kappa_0 x}, \\
\Omega &= 2\,f\,(x - \sqrt{2}\mu t), \quad f = \frac{1}{\sqrt{2}}\sqrt{\nu^2 + 2\,\kappa_0^2}, \\
\mu &= \kappa_0 - \sqrt{2}\,\lambda, \quad \nu = \kappa_0 + \sqrt{2}\,\lambda, \\
a &= i(\nu - \sqrt{2}f) - \sqrt{2}\kappa_0, \quad b = i(\nu + \sqrt{2}f) - \sqrt{2}\kappa_0, \quad d = 16f^2.
\end{aligned} \tag{A.8}
$$

We have assumed the form of φ_1 and φ_2 in (A.7), then substituted in (A.6) to obtain its exact expression as given in (A.8).

114

A.2.2 Calculation for G_0

If $\phi_{[1]}$ and $\phi_{[2]}$ are two known vector valued eigenfunctions of the Lax pair (A.6) corresponding to the parameters λ_0 and $\overline{\lambda}_0$. Using the matrices

$$M_0 = \mathrm{diag}(\lambda_0, \overline{\lambda}_0), \quad H = \begin{pmatrix} \phi_{[1]} & \phi_{[2]} \end{pmatrix}, \quad G_0 = -HM_0H^{-1}, \tag{A.9}$$

the Darboux matrix $G_1(\lambda)$ can be found in the form

$$G_1(\lambda) = \lambda \mathbf{I} + G_0. \tag{A.10}$$

We will first obtain suitable $\phi_{[1]}$ and $\phi_{[2]}$ from (A.7) by considering its column matrices, and then calculate the Darboux matrix.

Let $\phi_{[1]}$ and $\phi_{[2]}$ be

$$\phi_{[1]} = \frac{1}{\sqrt{d_0}} \begin{pmatrix} \phi_1 \\ \phi_2 \end{pmatrix}, \quad \phi_{[2]} = \frac{1}{\sqrt{d_0}} \begin{pmatrix} -\overline{\phi}_2 \\ \overline{\phi}_1 \end{pmatrix}, \tag{A.11}$$

where,

$$
\begin{aligned}
\phi_1 &= \left(a_0 \, e^{i\Omega_0/2} + b_0 \, e^{-i\Omega_0/2} \right) e^{i\frac{1}{\sqrt{2}}\kappa_0 x}, \\
\phi_2 &= -\left(b_0 \, e^{i\Omega_0/2} + a_0 \, e^{-i\Omega_0/2} \right) e^{-i\frac{1}{\sqrt{2}}\kappa_0 x}, \\
\Omega_0 &= 2\,f_0\,(x - \sqrt{2}\mu_0 t), \quad f_0 = \frac{1}{\sqrt{2}} \sqrt{\nu_0^2 + 2\,\kappa_0^2}, \\
\mu_0 &= \kappa_0 - \sqrt{2}\,\lambda_0, \quad \nu_0 = \kappa_0 + \sqrt{2}\,\lambda_0, \\
a_0 &= i(\nu_0 - \sqrt{2}f_0) - \sqrt{2}\kappa_0, \quad b_0 = i(\nu_0 + \sqrt{2}f_0) - \sqrt{2}\kappa_0, \quad d_0 = 16f_0^2.
\end{aligned}
\tag{A.12}
$$

One can verify that $\phi_{[1]}$ and $\phi_{[2]}$ defined in (A.11) satisfy the Lax pair (A.6) corresponding to the parameters λ_0 and $\overline{\lambda}_0$, i.e., the connections U_{h} and V_{h} computed at $\lambda = \lambda_0$ and $\lambda = \overline{\lambda}_0$ respectively. Then the matrices (A.9) may be written as

$$M_0 = \begin{pmatrix} \lambda_0 & 0 \\ 0 & \overline{\lambda}_0 \end{pmatrix}, \quad H = \frac{1}{\sqrt{d_0}} \begin{pmatrix} \phi_1 & -\overline{\phi}_2 \\ \phi_2 & \overline{\phi}_1 \end{pmatrix}, \quad G_0 = -HM_0H^{-1}. \tag{A.13}$$

A direct matrix multiplication gives G_0 as,

$$G_0 = -\frac{1}{\sqrt{d_0}} \begin{pmatrix} \phi_1 & -\overline{\phi}_2 \\ \phi_2 & \overline{\phi}_1 \end{pmatrix} \begin{pmatrix} \lambda_0 & 0 \\ 0 & \overline{\lambda}_0 \end{pmatrix} \frac{\sqrt{d_0}}{|\phi_1|^2 + |\phi_2|^2} \begin{pmatrix} \overline{\phi}_1 & \overline{\phi}_2 \\ -\phi_2 & \phi_1 \end{pmatrix}. \qquad \text{(A.14)}$$

Further simplification leads to,

$$G_0 = \begin{pmatrix} -\lambda_{0R} & 0 \\ 0 & -\lambda_{0R} \end{pmatrix} + \frac{i\lambda_{0I}}{|\phi_1|^2 + |\phi_2|^2} \begin{pmatrix} -(|\phi_1|^2 - |\phi_2|^2) & -2\phi_1\overline{\phi}_2 \\ -2\overline{\phi}_1\phi_2 & (|\phi_1|^2 - |\phi_2|^2) \end{pmatrix}. \qquad \text{(A.15)}$$

where the matrix elements can be found from functions defined in (A.12) as follows:

$$|\phi_1|^2 + |\phi_2|^2 = 2(\overline{a}_0 b_0 + \overline{b}_0 a_0)\cos\Omega_{0R} + 2(\overline{a}_0 a_0 + \overline{b}_0 b_0)\cosh\Omega_{0I},$$
$$|\phi_1|^2 - |\phi_2|^2 = -2i(\overline{a}_0 b_0 - \overline{b}_0 a_0)\sin\Omega_{0R} - 2(\overline{a}_0 a_0 - \overline{b}_0 b_0)\sinh\Omega_{0I},$$
$$(-2\phi_1\overline{\phi}_2)/(e^{i\sqrt{2}\kappa_0 x}) = 2(\overline{a}_0 a_0)e^{i\Omega_{0R}} + 2(\overline{b}_0 b_0)e^{-i\Omega_{0R}} + 2(\overline{a}_0 b_0)e^{\Omega_{0I}} + 2(\overline{b}_0 a_0)e^{-\Omega_{0I}}.$$
$$\text{(A.16)}$$

Define constants c_1, c_2, c_3 and c_4 as shown below

$$\begin{aligned} c_1 &= 2(\overline{a}_0 a_0 + \overline{b}_0 b_0), \\ c_2 &= 2(\overline{a}_0 b_0 + \overline{b}_0 a_0), \\ c_3 &= -2(\overline{a}_0 a_0 - \overline{b}_0 b_0), \\ c_4 &= -2i(\overline{a}_0 b_0 - \overline{b}_0 a_0). \end{aligned} \qquad \text{(A.17)}$$

Substitute these constants in (A.16). Then G_0 may be written as

$$G_0 = \begin{pmatrix} -\lambda_{0R} & 0 \\ 0 & -\lambda_{0R} \end{pmatrix} + i\frac{\lambda_{0I}}{\chi} \begin{pmatrix} -\xi & e^{i\sqrt{2}\kappa_0 x}(\zeta - i\,\eta) \\ e^{-i\sqrt{2}\kappa_0 x}(\zeta + i\,\eta) & \xi \end{pmatrix}, \qquad \text{(A.18)}$$

where,

$$\begin{aligned} \zeta &= c_1\,\cos(\Omega_{0R}) + c_2\,\cosh(\Omega_{0I}), \\ \eta &= c_3\,\sin(\Omega_{0R}) - c_4\,\sinh(\Omega_{0I}), \\ \xi &= c_4\,\sin(\Omega_{0R}) + c_3\,\sinh(\Omega_{0I}), \\ \chi &= c_2\,\cos(\Omega_{0R}) + c_1\,\cosh(\Omega_{0I}). \end{aligned} \qquad \text{(A.19)}$$

A straightforward calculation of (A.17) gives,

$$
\begin{aligned}
c_1 &= 2\left(4\,\kappa_0^2 + 2\,|\nu_0|^2 + 4\sqrt{2}\,\kappa_0\,\nu_{0I} + 4\,|f_0|^2\right), \\
c_2 &= 2\left(4\,\kappa_0^2 + 2\,|\nu_0|^2 + 4\sqrt{2}\,\kappa_0\,\nu_{0I} - 4\,|f_0|^2\right), \\
c_3 &= 2\left(8\,\kappa_0\,f_{0I} + 4\sqrt{2}\,(\nu_{0R}\,f_{0R} + \nu_{0I}\,f_{0I})\right), \\
c_4 &= -2\left(8\,\kappa_0\,f_{0R} + 4\sqrt{2}\,(\nu_{0I}\,f_{0R} - \nu_{0R}\,f_{0I})\right).
\end{aligned}
\tag{A.20}
$$

As a remark — G_0 (A.18) is independent of λ, and $G_0 G_0^\dagger = |\lambda_0|^2 \mathbf{I}$.

A.2.3   1-soliton solution

Starting with a known solution ψ_{h}, a new solution ψ_1 can be obtained by,

$$
\psi_1 = \psi_{\mathrm{h}} - 2i(G_0)_{12},
\tag{A.21}
$$

where $(G_0)_{12}$ is the second element of the first row in G_0 (A.18). Therefore the required solution, 1-breather is given by,

$$
\psi_1 = e^{i\sqrt{2}\kappa_0 x}\left(\kappa_0 - 2\,\lambda_{0I}\,\frac{(\zeta - i\,\eta)}{\chi}\right).
\tag{A.22}
$$

Note that $\psi_{\mathrm{h}}, -\psi_{\mathrm{h}}, \psi_1$ and $-\psi_1$ are all equally satisfy NLSE (A.1). Hence suitable sign changes are allowed in (A.22).

A.2.4   Darboux matrix $G_1(\lambda)$

The Darboux matrix $G_1(\lambda)$ can be found in the form $G_1(\lambda) = \lambda \mathbf{I} + G_0$. We write it explicitly as,

$$
G_1 = \begin{pmatrix} \lambda - \lambda_{0R} & 0 \\ 0 & \lambda - \lambda_{0R} \end{pmatrix} + i\,\frac{\lambda_{0I}}{\chi}\begin{pmatrix} -\xi & e^{i\sqrt{2}\kappa_0 x}(\zeta - i\,\eta) \\ e^{-i\sqrt{2}\kappa_0 x}(\zeta + i\,\eta) & \xi \end{pmatrix}.
\tag{A.23}
$$

Darboux transformation gives a new $\boldsymbol{\Psi}_1$ by,

$$
\boldsymbol{\Psi}_1(x,t,\lambda,\lambda_0) = \frac{1}{\sqrt{d_1}}\,G_1(x,t,\lambda,\lambda_0)\,\boldsymbol{\Psi}_{\mathrm{h}}(x,t,\lambda),
\tag{A.24}
$$

117

where $d_1 = |G_1| = (\lambda^2 + |\lambda_0|^2 - 2\lambda\lambda_{0R})$. Matrix solution $\boldsymbol{\Psi}_1$ satisfies the Lax pair

$$
\begin{aligned}
\boldsymbol{\Psi}_{1,x} &= U_1\boldsymbol{\Psi}_1, \\
\boldsymbol{\Psi}_{1,t} &= V_1\boldsymbol{\Psi}_1,
\end{aligned}
\tag{A.25}
$$

where $U_1 = U(\psi_1)$, and $V_1 = V(\psi_1)$. One may compare (A.25) with (A.6) to see how Darboux transformation transform ψ and $\boldsymbol{\Psi}$ systematically.

A.3 Akhmediev type breather

Akhmediev breather (AB) [11] is a spatially periodic breather. We note that, the new breather solution ψ_1 (A.22) shows spatial periodicity under suitable conditions. This section elaborate the derivation for this special case — Akhmediev type breather.

In this case, the largest modulation occurs at $t = 0$; that too only once. From the functional form of ζ, η and χ given in (A.19), one can infer that the largest modulation arises from hyperbolic function for which the argument is Ω_{0I}. On the other hand, periodicity comes from Ω_{0R} via trigonometric functions. We will discuss a special case where $\Omega_{0I} \equiv \Omega_{0I}(t)$, a function of t alone, so that the breather peaks align at $t = 0$ line in the $x-t$ plane. But in this case it is not possible to impose any restriction in Ω_{0R}. Nevertheless, a spatially periodic solution qualitatively similar to Akhmediev breather can be achieved.

Recall the functions defined in (A.12). Consider,

$$
2\,f_0^2 = \nu_0^2 + 2\,\kappa_0^2,
\tag{A.26}
$$

where, $\nu_0 = \nu_{0R} + i\,\nu_{0I} = (\kappa_0 + \sqrt{2}\,\lambda_{0R}) + i\sqrt{2}\,\lambda_{0I}$. Let $\nu_{0R} = 0$, (i.e., $\lambda_{0R} = -\frac{\kappa_0}{\sqrt{2}}$). Then (A.26) becomes,

$$
f_0^2 = \kappa^2 - \lambda_{0I}^2.
\tag{A.27}
$$

Note that the right hand side of Eq. (A.27) is real, whereas f_0 is complex in general. Thus we have two cases as shown below:

- case 1: $\kappa_0^2 < \lambda_{0I}^2$

$$
f_{0I}^2 = \lambda_{0I}^2 - \kappa_0^2, \quad f_{0R} = 0.
\tag{A.28}
$$

- case 2: $\kappa_0^2 > \lambda_{0I}^2$

$$
f_{0R}^2 = \kappa_0^2 - \lambda_{0I}^2, \quad f_{0I} = 0.
\tag{A.29}
$$

We write Ω_{0R} and Ω_{0I} explicitly,

$$\begin{aligned}
\Omega_{0R} &= 2\, f_{0R}\, x + 2\sqrt{2}\, t\, (f_{0I}\, \mu_{0I} - f_{0R}\, \mu_{0R}), \\
\Omega_{0I} &= 2\, f_{0I}\, x - 2\sqrt{2}\, t\, (f_{0I}\, \mu_{0R} + f_{0R}\, \mu_{0I}).
\end{aligned} \tag{A.30}$$

As pointed out earlier, we are interested in a special case with $\Omega_{0I} \equiv \Omega_{0I}(t)$. Therefore we choose case 2, where $f_{0I} = 0$. Thus there is no x dependence in Ω_{0I} and our condition is met. We will not discuss case 1 here, since it does not give anything special. In brief, the condition for Akhmediev type breather is,

$$\lambda_{0R} = -\frac{\kappa_0}{\sqrt{2}}, \quad \text{and} \quad \kappa_0^2 > \lambda_{0I}^2. \tag{A.31}$$

Equation (A.29), $\kappa_0^2 = \lambda_{0I}^2 + f_{0R}^2$ can be expressed conveniently by introducing a real parameter ϕ such that,

$$\lambda_{0I} = \kappa_0 \cos\phi, \quad \text{and} \quad f_{0R} = \kappa_0 \sin\phi. \tag{A.32}$$

It follows that $\mu_{0R} = 2\kappa_0$, $\mu_{0I} = -\sqrt{2}\lambda_{0I}$ along with $f_{0I} = 0$. Equation (A.30) get simplified as follows:

$$\begin{aligned}
\Omega_{0R} &= q(x - 2\sqrt{2}\kappa_0 t), \\
\Omega_{0I} &= rt,
\end{aligned} \tag{A.33}$$

where $q = 2\kappa_0 \sin\phi$ and $r = 2\kappa_0^2 \sin(2\phi)$. Constants c_i given in (A.20) become,

$$c_1 = 16(\kappa_0 + \lambda_{0I})\kappa_0, \quad c_2 = c_1 \cos\phi, \quad c_3 = 0, \quad c_4 = -c_1 \sin\phi. \tag{A.34}$$

Functions ζ, η, χ in (A.19) now get simplified to

$$\begin{aligned}
\zeta &= c_1 \big(\cos(q(x - 2\sqrt{2}\kappa_0 t)) + \cos\phi \, \cosh(rt) \big), \\
\eta &= c_1 \sin\phi \, \sinh(rt), \\
\chi &= c_1 \big(\cos\phi \, \cos(q(x - 2\sqrt{2}\kappa_0 t)) + \cosh(rt) \big).
\end{aligned} \tag{A.35}$$

Finally the breather solution ψ_1 (A.22) reduces to,

$$\psi_{\text{GAB}} = -\kappa_0\, e^{i\sqrt{2}\kappa_0(x-x_0)}\, \frac{\cosh(rt - 2i\phi) - \cos\phi \, \cos(q(x - vt))}{\cosh(rt) - \cos\phi \, \cos(q(x - vt))}, \tag{A.36}$$

where, $q = 2\kappa_0 \sin(\phi)$, $r = 2\kappa_0^2 \sin(2\phi)$, $v = 2\sqrt{2}\kappa_0$, $\phi = \cos^{-1}(\lambda_{0I}/\kappa_0)$ and $x_0 = \pi/q$.

119

It is clear that, the breather solution ψ_{GAB} is localized in t and periodic in x. Comparing (A.36) with Akhmediev breather ψ_{AB} (B.39), one can infer that, a Galilean transformation of ψ_{AB} leads to ψ_{GAB}. Hence the name ψ_{GAB} – Galilean transformed Akhmediev Breather.

Appendix B

NLS Circle: Darboux transformation and breather solutions

We choose an informal name "NLS Circle" to label the broad class of solutions and expressions that are associated with seed solution, $\psi_{\mathrm{c}} = \kappa_0\, e^{2i\kappa_0^2 t}$. Space curve associated with this seed is a circle. In this chapter, we provide mathematical steps for the DT technique. We will also provide the derivation of the well known breather solutions AB, KMB, PS and their space curve description.

B.1 NLSE and the Lax pair

The nonlinear Schrödinger equation (NLSE)

$$i\psi_t + \psi_{xx} + 2|\psi|^2\psi = 0, \tag{B.1}$$

arises as the compatibility condition for the linear system, also known as Lax pair

$$\boldsymbol{\Psi}_x = U\boldsymbol{\Psi}, \quad \boldsymbol{\Psi}_t = V\boldsymbol{\Psi}, \tag{B.2}$$

where the connections U and V are in general functions of x, t and spectral parameter λ. For convenience one can treat them as functions of ψ and its derivatives, as given below:

$$U(\psi) = \begin{pmatrix} 0 & \psi \\ -\overline{\psi} & 0 \end{pmatrix} + \lambda \begin{pmatrix} -i & 0 \\ 0 & i \end{pmatrix}, \tag{B.3}$$

$$V(\psi) = \begin{pmatrix} i|\psi|^2 & i\,\psi_x \\ i\,\overline{\psi}_x & -i|\psi|^2 \end{pmatrix} + \lambda \begin{pmatrix} 0 & 2\psi \\ -2\overline{\psi} & 0 \end{pmatrix} + \lambda^2 \begin{pmatrix} -2i & 0 \\ 0 & 2i \end{pmatrix}. \tag{B.4}$$

B.2 Darboux transformation

Each solution to the NLSE (B.1) corresponds to a matrix solution to the Lax pair (B.2). We employ Darboux transformation detailed in section 2.6.2, to obtain a new breather solution, by starting from a seed solution

$$\psi_{\mathrm{c}} = \kappa_0 \, e^{2i\kappa_0^2 t}, \tag{B.5}$$

for a real constant κ_0.

B.2.1 Seed solution and related functions

Seed solution ψ_{c} corresponds to a matrix solution $\boldsymbol{\Psi}_{\mathrm{c}}(x,t,\lambda)$ to the below Lax pair

$$\begin{aligned}
\boldsymbol{\Psi}_{\mathrm{c},x} &= U_{\mathrm{c}}\boldsymbol{\Psi}_{\mathrm{c}}, \\
\boldsymbol{\Psi}_{\mathrm{c},t} &= V_{\mathrm{c}}\boldsymbol{\Psi}_{\mathrm{c}},
\end{aligned} \tag{B.6}$$

where $U_{\mathrm{c}} = U(\psi_{\mathrm{c}})$, and $V_{\mathrm{c}} = V(\psi_{\mathrm{c}})$. We explicitly write the matrix solution $\boldsymbol{\Psi}_{\mathrm{c}}$ in the form,

$$\boldsymbol{\Psi}_{\mathrm{c}}(x,t,\lambda) = \frac{1}{\sqrt{d}} \begin{pmatrix} \varphi_1 & -\overline{\varphi}_2 \\ \varphi_2 & \overline{\varphi}_1 \end{pmatrix}, \tag{B.7}$$

where,

$$\begin{aligned}
\varphi_1 &= \left(e^{-i\omega/2} + i\,\frac{(\lambda - p)}{\kappa_0}\, e^{i\omega/2} \right) e^{i\kappa_0^2 t}, \\
\varphi_2 &= \left(i\,\frac{(\lambda - p)}{\kappa_0}\, e^{-i\omega/2} + e^{i\omega/2} \right) e^{-i\kappa_0^2 t}, \\
\omega &= 2\,p(x + 2\lambda t), \quad p = (\kappa_0^2 + \lambda^2)^{1/2}, \quad d = 4(\kappa_0^2 + \lambda^2 - \lambda p)/\kappa_0^2.
\end{aligned} \tag{B.8}$$

We have assumed the form of φ_1 and φ_2 in (B.7), similar to the form given by Yan-Chow Ma [103, Sec. II], then substituted in (B.6) to obtain its exact expression as given in (B.8).

B.2.2 Calculation for G_0

If $\boldsymbol{\phi}_{[1]}$ and $\boldsymbol{\phi}_{[2]}$ are two known vector valued eigenfunctions of the Lax pair (B.6) corresponding to the parameters λ_0 and $\overline{\lambda}_0$. Using the matrices

$$M_0 = \mathrm{diag}(\lambda_0, \overline{\lambda}_0), \quad H = \begin{pmatrix} \boldsymbol{\phi}_{[1]} & \boldsymbol{\phi}_{[2]} \end{pmatrix}, \quad G_0 = -HM_0H^{-1}, \tag{B.9}$$

122

the Darboux matrix $\mathbf{P}_1(\lambda)$ can be found in the form

$$\mathbf{P}_1(\lambda) = \lambda\mathbf{I} + G_0. \tag{B.10}$$

We will first obtain suitable $\phi_{[1]}$ and $\phi_{[2]}$ from (B.7) by considering its column matrices, and then calculate the Darboux matrix.

Let $\phi_{[1]}$ and $\phi_{[2]}$ be

$$\phi_{[1]} = \frac{1}{\sqrt{d_0}} \begin{pmatrix} \phi_1 \\ \phi_2 \end{pmatrix}, \quad \phi_{[2]} = \frac{1}{\sqrt{d_0}} \begin{pmatrix} -\overline{\phi}_2 \\ \overline{\phi}_1 \end{pmatrix}, \tag{B.11}$$

where,

$$\phi_1 = \left(e^{-i\omega_0/2} + \frac{i\mu_0}{\kappa_0} e^{i\omega_0/2} \right) e^{i\kappa_0^2 t},$$

$$\phi_2 = \left(\frac{i\mu_0}{\kappa_0} e^{-i\omega_0/2} + e^{i\omega_0/2} \right) e^{-i\kappa_0^2 t}, \tag{B.12}$$

$$\omega_0 = 2\,p_0(x + 2\lambda_0 t), \quad \mu_0 = (\lambda_0 - p_0),$$

$$p_0 = (\kappa_0^2 + \lambda_0^2)^{1/2}, \quad d_0 = 4(\kappa_0^2 + \lambda_0^2 - \lambda_0 p_0)/\kappa_0^2.$$

One can verify that $\phi_{[1]}$ and $\phi_{[2]}$ defined in (B.11) satisfy the Lax pair (B.6) corresponding to the parameters λ_0 and $\overline{\lambda}_0$, i.e., the connections U_c and V_c computed at $\lambda = \lambda_0$ and $\lambda = \overline{\lambda}_0$ respectively. Then the matrices (B.9) may be written as

$$M_0 = \begin{pmatrix} \lambda_0 & 0 \\ 0 & \overline{\lambda}_0 \end{pmatrix}, \quad H = \frac{1}{\sqrt{d_0}} \begin{pmatrix} \phi_1 & -\overline{\phi}_2 \\ \phi_2 & \overline{\phi}_1 \end{pmatrix}, \quad G_0 = -HM_0H^{-1}. \tag{B.13}$$

A direct matrix multiplication gives G_0 as,

$$G_0 = -\frac{1}{\sqrt{d_0}} \begin{pmatrix} \phi_1 & -\overline{\phi}_2 \\ \phi_2 & \overline{\phi}_1 \end{pmatrix} \begin{pmatrix} \lambda_0 & 0 \\ 0 & \overline{\lambda}_0 \end{pmatrix} \frac{\sqrt{d_0}}{|\phi_1|^2 + |\phi_2|^2} \begin{pmatrix} \overline{\phi}_1 & \overline{\phi}_2 \\ -\phi_2 & \phi_1 \end{pmatrix}. \tag{B.14}$$

Further simplification leads to

$$G_0 = \begin{pmatrix} -\lambda_{0R} & 0 \\ 0 & -\lambda_{0R} \end{pmatrix} + \frac{i\lambda_{0I}}{|\phi_1|^2 + |\phi_2|^2} \begin{pmatrix} -(|\phi_1|^2 - |\phi_2|^2) & -2\phi_1\overline{\phi}_2 \\ -2\overline{\phi}_1\phi_2 & (|\phi_1|^2 - |\phi_2|^2) \end{pmatrix}. \tag{B.15}$$

123

where the matrix elements can be found from functions defined in (B.12) as follows:

$$|\phi_1|^2 + |\phi_2|^2 = \big(2\kappa_0(p_{0I} - \lambda_{0I})\cos\omega_{0R} + (\kappa_0^2 + |\mu_0|^2)\cosh\omega_{0I}\big)/\kappa_0^2,$$

$$|\phi_1|^2 - |\phi_2|^2 = \big(2\kappa_0(p_{0R} - \lambda_{0R})\sin\omega_{0R} + (\kappa_0^2 - |\mu_0|^2)\sinh\omega_{0I}\big)/\kappa_0^2, \qquad \text{(B.16)}$$

$$-2\phi_1\overline{\phi}_2 = -e^{2i\kappa_0^2 t}\big(|\mu_0|^2 e^{i\omega_{0R}} + \kappa_0^2 e^{-i\omega_{0R}} + i\mu\frac{\kappa_0}{2}e^{-\omega_{0I}} - i\overline{\mu}\frac{\kappa_0}{2}e^{\omega_{0I}}\big)/\kappa_0^2.$$

Define constants b_1, b_2, b_3 and b_4 as shown below

$$
\begin{aligned}
b_1 &= \kappa_0^2 + |\mu_0|^2, \\
b_2 &= 2\kappa_0(p_{0I} - \lambda_{0I}), \\
b_3 &= \kappa_0^2 - |\mu_0|^2, \\
b_4 &= 2\kappa_0(p_{0R} - \lambda_{0R}).
\end{aligned}
\qquad \text{(B.17)}
$$

Substitute these constants in (B.16). Then G_0 may be written as

$$
G_0 = \begin{pmatrix} -\lambda_{0R} & 0 \\ 0 & -\lambda_{0R} \end{pmatrix} + i\frac{\lambda_{0I}}{\Delta}\begin{pmatrix} -\gamma & -e^{2i\kappa_0^2 t}(\alpha - i\beta) \\ -e^{-2i\kappa_0^2 t}(\alpha + i\beta) & \gamma \end{pmatrix}, \qquad \text{(B.18)}
$$

where,

$$
\begin{aligned}
\alpha &= b_1\cos\omega_{0R} + b_2\cosh\omega_{0I}, \\
\beta &= b_3\sin\omega_{0R} - b_4\sinh\omega_{0I}, \\
\gamma &= b_4\sin\omega_{0R} + b_3\sinh\omega_{0I}, \\
\Delta &= b_2\cos\omega_{0R} + b_1\cosh\omega_{0I}
\end{aligned}
\qquad \text{(B.19)}
$$

A straightforward calculation of (B.17) gives,

$$
\begin{aligned}
b_1 &= 2(\lambda_{0I}^2 + p_{0R}^2 - \lambda_{0R}p_{0R} - \lambda_{0I}p_{0I}), \\
b_2 &= 2\kappa_0(p_{0I} - \lambda_{0I}), \\
b_3 &= -2(\lambda_{0R}^2 + p_{0I}^2 - \lambda_{0R}p_{0R} - \lambda_{0I}p_{0I}), \\
b_4 &= 2\kappa_0(p_{0R} - \lambda_{0R}).
\end{aligned}
\qquad \text{(B.20)}
$$

As a remark — G_0 (B.18) is independent of λ, and $G_0 G_0^\dagger = |\lambda_0|^2\mathbf{I}$.

B.2.3   1-soliton solution

Starting with a known solution ψ_c, a new solution ψ_{cb} can be obtained by,

$$\psi_{cb} = \psi_c - 2i(G_0)_{12}, \tag{B.21}$$

where $(G_0)_{12}$ is the second element of the first row in G_0 (B.18). The required solution, 1-breather is given by,

$$\psi_{cb} = e^{2i\kappa_0^2 t}\left(\kappa_0 + 2\lambda_{0I}\frac{(\alpha - i\beta)}{\Delta}\right), \tag{B.22}$$

where λ_0 is a complex parameter, and the functions α, β and Δ are defined in (B.19). Note that $\psi_c, -\psi_c, \psi_{cb}$ and $-\psi_{cb}$ are all equally satisfy the NLSE, hence suitable sign changes are allowed in (B.22).

B.2.4   Darboux matrix $\mathbf{P}_1(\lambda)$

The Darboux matrix $\mathbf{P}_1(\lambda)$ can be found in the form $\mathbf{P}_1(\lambda) = \lambda\mathbf{I} + G_0$. We write it explicitly as,

$$\mathbf{P}_1 = \begin{pmatrix} \lambda - \lambda_{0R} & 0 \\ 0 & \lambda - \lambda_{0R} \end{pmatrix} + i\frac{\lambda_{0I}}{\Delta}\begin{pmatrix} -\gamma & -e^{2i\kappa_0^2 t}(\alpha - i\beta) \\ -e^{-2i\kappa_0^2 t}(\alpha + i\beta) & \gamma \end{pmatrix}, \tag{B.23}$$

where λ_0 is a complex parameter, and the functions α, β, γ and Δ are defined in (B.19). Darboux transformation gives a new $\boldsymbol{\Psi}_{cb}$ by,

$$\boldsymbol{\Psi}_{cb}(x, t, \lambda, \lambda_0) = \frac{1}{\sqrt{d_1}}\,\mathbf{P}_1(x, t, \lambda, \lambda_0)\,\boldsymbol{\Psi}_c(x, t, \lambda), \tag{B.24}$$

where $d_1 = |\mathbf{P}_1| = (\lambda^2 + |\lambda_0|^2 - 2\lambda\lambda_{0R})$. Matrix solution $\boldsymbol{\Psi}_{cb}$ satisfies the Lax pair

$$\begin{aligned} \boldsymbol{\Psi}_{cb,x} &= U_{cb}\boldsymbol{\Psi}_{cb}, \\ \boldsymbol{\Psi}_{cb,t} &= V_{cb}\boldsymbol{\Psi}_{cb}, \end{aligned} \tag{B.25}$$

where $U_{cb} = U(\psi_{cb})$, and $V_{cb} = V(\psi_{cb})$. One may compare (B.25) with (B.6) to see how Darboux transformation transform ψ and $\boldsymbol{\Psi}$ systematically.

B.3 Fundamental solutions in the limit $\lambda \to 0$

We have given the fundamental solutions $\boldsymbol{\Psi}_{\mathrm{c}}$ (B.7) and $\boldsymbol{\Psi}_{\mathrm{cb}}$ (B.24) in the previous sections. In order to calculate the spin configuration, the above matrices in the limit $\lambda \to 0$ is required. Matrix $\boldsymbol{\Psi}_{\mathrm{c}}$ is written in terms of two complex functions φ_1 and φ_2. We will write these complex functions in the required limit.

Setting $\lambda = 0$, it follows that,

$$d = 4, \quad p = \kappa_0, \quad \omega = 2\kappa_0 x. \tag{B.26}$$

Substituting this in (B.8), φ_1 can be simplified as follows:

$$
\begin{aligned}
\varphi_1 &= \left(e^{-i\kappa_0 x} - i e^{i\kappa_0 x}\right) e^{i\kappa_0^2 t} \\
&= \left(e^{-i\kappa_0 x} + e^{i(\kappa_0 x - \pi/2)}\right) e^{i\kappa_0^2 t} \qquad \left(-i = e^{-i\pi/2}\right) \\
&= \left(e^{-i(\kappa_0 x - \pi/4)} + e^{i(\kappa_0 x - \pi/4)}\right) e^{i\kappa_0^2 t} e^{-i\pi/4} \\
&= 2\cos(\kappa_0 x - \pi/4)\, e^{i(\kappa_0^2 t - \pi/4)}.
\end{aligned}
\tag{B.27}
$$

Similarly φ_2 can be simplified as follows:

$$
\begin{aligned}
\varphi_2 &= \left(-i e^{-i\kappa_0 x} + e^{i\kappa_0 x}\right) e^{-i\kappa_0^2 t} \\
&= \left(-e^{-i(\kappa_0 x - \pi/2)} + e^{i\kappa_0 x}\right) e^{-i\kappa_0^2 t} \qquad \left(i = e^{i\pi/2}\right) \\
&= \left(-e^{-i(\kappa_0 x - \pi/4)} + e^{i(\kappa_0 x - \pi/4)}\right) e^{-i\kappa_0^2 t} e^{i\pi/4} \\
&= 2i\sin(\kappa_0 x - \pi/4)\, e^{-i(\kappa_0^2 t - \pi/4)}.
\end{aligned}
\tag{B.28}
$$

Matrix $\boldsymbol{\Psi}_{\mathrm{cb}}$ (B.24) is expressed as a product of $\mathbf{P}_1$ and $\boldsymbol{\Psi}_{\mathrm{c}}$. Since $\boldsymbol{\Psi}_{\mathrm{c}}$ is already given in the required limit, here we will deal with $\mathbf{P}_1$ alone. In Chapter 4, our discussion is mainly based on a special case with $\lambda_{0R} = 0$. So we apply both the limits together, i.e.,

$$\lambda_{0R} = 0, \quad \text{and} \quad \lambda = 0. \tag{B.29}$$

It follows that,

$$d_1 = |\mathbf{P}_1| = \left(\lambda^2 + |\lambda_0|^2 - 2\lambda\lambda_{0R}\right) = \lambda_{0I}^2, \tag{B.30}$$

and

$$\frac{1}{\sqrt{d_1}}\, \mathbf{P}_1 = \frac{1}{\Delta} \begin{pmatrix} -i\gamma & -e^{2i\kappa_0^2 t}(\beta + i\alpha) \\ e^{-2i\kappa_0^2 t}(\beta - i\alpha) & i\gamma \end{pmatrix}. \tag{B.31}$$

B.4 Akhmediev Breather (AB)

Recall the general expression for $\psi_{\mathrm{cb}}(x,t)$ (B.22) and necessary functions and constants defined in (B.19) and (B.20) respectively. It is to be noted that the functions α, β, γ and Δ are depending on x and t through ω_0. Hence, we write its real and imaginary parts explicitly as,

$$\omega_{0R} = 2p_{0R}\,x + 4t(p_{0R}\,\lambda_{0R} - p_{0I}\,\lambda_{0I}),$$
$$\omega_{0I} = 2p_{0I}\,x + 4t(p_{0R}\,\lambda_{0I} + p_{0I}\,\lambda_{0R}). \tag{B.32}$$

The condition for obtaining Akhmediev breather is,

$$\lambda_{0R} = 0; \text{ and } \kappa_0^2 > \lambda_{0I}^2, \tag{B.33}$$

which readily give $p_{0I} = 0$ along with a relation, $\lambda_{0I}^2 + p_{0R}^2 = \kappa_0^2$. Now introduce ϕ such that,

$$\lambda_{0I} = \kappa_0 \cos\phi, \quad p_{0R} = \kappa_0 \sin\phi. \tag{B.34}$$

Constants b_1, b_2, b_3 and b_4 in (B.20) reduces to

$$b_1 = 2\kappa_0^2, \quad b_2 = -2\kappa_0^2 \cos\phi, \quad b_3 = 0, \quad b_4 = 2\kappa_0^2 \sin\phi. \tag{B.35}$$

Simplifying (B.32) by introducing q and r as follows:

$$\omega_{0R} = 2\kappa_0 \sin(\phi)x = qx,$$
$$\omega_{0I} = 4\kappa_0^2 t \sin\phi \cos\phi = 2\kappa_0^2 \sin(2\phi)\,t = rt, \tag{B.36}$$

where q and r are coefficients of x and t respectively. Functions α, β, γ, and Δ (B.19) get reduced to,

$$\alpha = 2\kappa_0^2\big(\cos(qx) - \cos\phi\,\cosh(rt)\big),$$
$$\beta = -2\kappa_0^2 \sin\phi\,\sinh(rt),$$
$$\gamma = 2\kappa_0^2 \sin\phi\,\cos(qx), \tag{B.37}$$
$$\Delta = -2\kappa_0^2\big(\cos\phi\,\cos(qx) - \cosh(rt)\big).$$

Making use of the relation

$$\cosh(rt - 2i\phi) = \cosh(rt)\cos(2\phi) - i\sinh(rt)\sin(2\phi), \tag{B.38}$$

127

equation (B.22) can be simplified to get the well known Akhmediev Breather (AB),

$$\psi_{\mathrm{AB}} = -\kappa_0 e^{2i\kappa_0^2 t} \frac{\cosh(rt - 2i\phi) - \cos\phi\;\cos(qx)}{\cosh(rt) - \cos\phi\;\cos(qx)}, \tag{B.39}$$

where, $q = 2\kappa_0 \sin(\phi)$, $r = 2\kappa_0^2 \sin(2\phi)$ and $\phi = \cos^{-1}(\lambda_{0I}/\kappa_0)$. It is clear from the expression that the above breather is localized in t but periodic in x.

B.5   Peregrine Soliton (PS)

Peregrine soliton arises as a special case of ψ_{AB} (B.39) in the limit $\phi \to 0$. Taylor expansion of (B.39) followed by a straightforward simplification, leads to

$$\psi_{\mathrm{PS}} = -\kappa_0 e^{2i\kappa_0^2 t} \left(1 - \frac{4(1 + 4i\kappa_0^2 t)}{1 + 4\kappa_0^2 x^2 + 16\kappa_0^4 t^2} \right), \tag{B.40}$$

as discussed in Ref. [11, Sec. 3] (wherein authors set $\kappa_0 = 1$ for simplicity).

B.6   Kuznetsov-Ma Breather (KMB)

The condition for KMB is

$$\lambda_{0R} = 0; \text{ and } \quad \kappa_0^2 < \lambda_{0I}^2, \tag{B.41}$$

which give $p_{0R} = 0$ along with a relation, $\lambda_{0I}^2 - p_{0I}^2 = \kappa_0^2$. Here we introduce ϕ (note the difference from (B.34)) such that,

$$\lambda_{0I} = \kappa_0 \cosh\phi, \text{ and } \quad p_{0I} = \kappa_0 \sinh\phi. \tag{B.42}$$

Constants b_1, b_2, b_3 and b_4 in (B.20) get reduced to

$$\begin{aligned}
b_1 &= 2\kappa_0^2 \cosh\phi(\cosh\phi - \sinh\phi), \\
b_2 &= -2\kappa_0^2(\cosh\phi - \sinh\phi), \\
b_3 &= 2\kappa_0^2 \sinh\phi(\cosh\phi - \sinh\phi), \\
b_4 &= 0.
\end{aligned} \tag{B.43}$$

Simplifying (B.32) as,

$$\omega_{0R} = -4\kappa_0^2 \sinh\phi \cosh\phi\, t = -2\kappa_0^2 \sinh(2\phi)\, t = -rt,$$
$$\omega_{0I} = 2\kappa_0 \sinh\phi\, x = qx,$$

(B.44)

where q and r are coefficients of x and t respectively. Functions α, β, γ,and Δ (B.19) get reduced to,

$$
\begin{aligned}
\alpha &= 2\kappa_0^2(\cosh\phi - \sinh\phi)\big(\cosh\phi\ \cos(rt) - \cosh(qx)\big), \\
\beta &= -2\kappa_0^2(\cosh\phi - \sinh\phi)\sinh\phi\ \sin(rt), \\
\gamma &= 2\kappa_0^2(\cosh\phi - \sinh\phi)\sinh\phi\ \sinh(qx), \\
\Delta &= 2\kappa_0^2(\cosh\phi - \sinh\phi)\big(\cosh\phi\ \cosh(qx) - \cos(rt)\big).
\end{aligned}
$$

(B.45)

Making use of the relation

$$\cos(rt - 2i\phi) = \cos(rt)\cosh(2\varphi) + i\sin(rt)\sinh(2\varphi),$$

(B.46)

equation (B.22) can be simplified to get the well known Kuznetsov-Ma Breather (KMB),

$$\psi_{\text{KMB}} = -\kappa_0 e^{2i\kappa_0^2 t}\, \frac{\cos(rt - 2i\phi) - \cosh\phi\ \cosh(qx)}{\cos(rt) - \cosh\phi\ \cosh(qx)},$$

(B.47)

where, $q = 2\kappa_0 \sinh(\phi)$, $r = 2\kappa_0^2 \sinh(2\phi)$ and $\phi = \cosh^{-1}(\lambda_{0I}/\kappa_0)$. Interested readers may see Ref. [11, Sec. 3], and further reduction to Peregrine soliton in the limit $\phi \to 0$.

B.7 Space curve associated with NLSE breather

Space curves associated with the above discussed well known breather solutions were studied by Cieśliński *et al.* [15] in 1986. Nevertheless we would like to write down those results here the way we obtained them, in line with with the other related expressions in this thesis. This is to get a better comparison and for the completeness of the topic.

Each solution ψ to the NLSE can be mapped to a moving space curve $\mathbf{R}$ which satisfies the LIA equation (2.22), $\mathbf{R}_t = \mathbf{R}_x \times \mathbf{R}_{xx}$, as described in Sec. 2.4. Space curve can be constructed using the expression, $\mathbf{R} = \lim_{\lambda \to 0} \mathbf{\Psi}^{-1}\mathbf{\Psi}_\lambda$, where $\mathbf{\Psi}$ is the fundamental solution to the Lax pair (B.2), and the subscript λ denotes differentiation with respect to λ.

The seed solution $\psi_{\mathrm{c}} = \kappa_0 \, e^{2i\kappa_0^2 t}$ thus corresponds to a space curve

$$\mathbf{R}_{\mathrm{c}} = \lim_{\lambda \to 0} \mathbf{\Psi}_{\mathrm{c}}^{-1} \mathbf{\Psi}_{\mathrm{c},\lambda}, \tag{B.48}$$

where $\mathbf{\Psi}_{\mathrm{c}}$ (B.7) is the matrix solution to the Lax pair (B.6). The space curve may be written as

$$\mathbf{R}_{\mathrm{c}}(x,t) = \frac{1}{2\kappa_0} \left[4\kappa_0^2 t \, \hat{\mathbf{i}} + \sin(2\kappa_0 x) \, \hat{\mathbf{j}} - \cos(2\kappa_0 x) \, \hat{\mathbf{k}} \right], \tag{B.49}$$

which is a circle of radius $\frac{1}{2\kappa_0}$ moving with a constant velocity $2\kappa_0$ along the $\hat{\mathbf{i}}$ direction. This models the smoke-ring motion [15]. The 1-soliton excitation of this circular vortex, namely $\mathbf{R}_{\mathrm{cb}}$, the associated space curve of the breather solution ψ_{c} (B.22), can be found by

$$\mathbf{R}_{\mathrm{cb}} = \lim_{\lambda \to 0} \mathbf{\Psi}_{\mathrm{cb}}^{-1} \mathbf{\Psi}_{\mathrm{cb},\lambda}, \tag{B.50}$$

where $\mathbf{\Psi}_{\mathrm{cb}}$ (B.24) is the matrix solution to the Lax pair (B.25). The space curve may be explicitly written as

$$\mathbf{R}_{\mathrm{cb}} = \mathbf{R}_{\mathrm{c}} + \frac{\lambda_{0I}}{|\lambda_0|^2 \Delta} \left\{ \beta \, \hat{\mathbf{i}} + \left[\alpha \sin(2\kappa_0 x) - \gamma \cos(2\kappa_0 x) \right] \hat{\mathbf{j}} + \left[-\alpha \cos(2\kappa_0 x) - \gamma \sin(2\kappa_0 x) \right] \hat{\mathbf{k}} \right\}. \tag{B.51}$$

Functions α, β, γ and Δ are defined in (B.19). Detailed plots of $\mathbf{R}_{\mathrm{cb}}$ (B.51) has been given in Figures 3.1, 3.2 and 3.3.

Expression given by Cieśliński *et al.* [15] can be obtained by the following substitution: $d = \lambda_{0I}/|\lambda_0|^2$, $n_1 = -\alpha/\Delta$, $n_2 = -\gamma/\Delta$, $n_3 = \beta/\Delta$ and a coordinate rotation about y axis through an angle $-\pi/2$, i.e., $\{\hat{\mathbf{i}}, \hat{\mathbf{j}}, \hat{\mathbf{k}}\} \Rightarrow \{-\hat{\mathbf{k}}, \hat{\mathbf{j}}, \hat{\mathbf{i}}\}$.

List of Publications

Refereed Journals

1. RAHUL O. R. and S. MURUGESH,
   Knot soliton solutions for the one-dimensional non-linear Schrödinger equation,
   Journal of Physics Communications **2**: 055033 (2018).
   doi: https://doi.org/10.1088/2399-6528/aac683

2. RAHUL O. R. and S. MURUGESH,
   Rogue breather modes: Topological sectors, and the 'belt-trick', in a one-dimensional
   ferromagnetic spin chain,
   Chaos, Solitons & Fractals **122**: 262 – 269 (2019).
   doi: https://doi.org/10.1016/j.chaos.2019.02.012

Article submitted

1. RAHUL O. R. and S. MURUGESH,
   Exact and non-exact Fermi-Pasta-Ulam-Tsingou recurrences in a Heisenberg ferro-
   magnet.
   Submitted to *Physica Scripta*